

Treatment Planning & Targeting During Shock Wave Therapy

Kya Shoar

Magdalen College

Department of Engineering Science

A thesis submitted for the degree of Doctor of Philosophy.

Trinity Term 2018

A thesis submitted for the degree
Doctor of Philosophy in Engineering Science:

Treatment Planning & Targeting During Shock Wave Therapy

by Kya Shoar, Magdalen College,
supervised by Professor Robin Cleveland.

Abstract

Shock wave lithotripsy is a non-invasive procedure by which kidney stones are fragmented. Currently, many shock waves are delivered to the body that do not impact the stone, but do result in tissue trauma, mainly caused by cavitation. This work presents a monitoring system to reduce the number of shock waves delivered to the body, by tracking the target, and to detect cavitation throughout the procedure.

For the first goal, a circular array, housing twenty-two 0.5 MHz transducers that can be mounted around the aperture of a clinical lithotripter, was used to collect pulse-echo data, from which an acoustic triangulation algorithm was able to locate stones. The accuracy of the system in water was better than 4 mm in the lateral direction and better than 2 mm in the axial direction within ±15 mm of the focus—which is the variation that would be expected clinically. For the second goal, the acoustic pressure field of a shock wave therapy source was measured and its cavitation field was determined. Cavitation was localised using a conventional ultrasound probe and passive acoustic mapping. Bubbles were shown to grow, collapse, and rebound, and the characteristic times were determined. It was found that these parameters increased with the energy level and the pulse repetition frequency and that at the highest energy setting the characteristic time was 288 µs. Finally, the characteristic time of cavitation in an ex vivo pig kidney and for an artificial stone in water due to a clinical shock wave source was determined using passive acoustic mapping. The characteristic times in the pig kidney were shorter than for the stone, e.g. 560 µs in the kidney and 730 µs on the stone at EL 6. No significant correlation between cavitation on a stone that fractured well and a stone that fractured poorly could be determined.

The work in this thesis heralds an advance in current lithotripsy monitoring techniques that are based on B-mode and x-ray. Real-time tracking of the kidney stone and cavitation mapping throughout the treatment would limit the renal injury that routinely occurs during lithotripsy.

Acknowledgements

First and foremost, I would like to thank my supervisor, **Professor Robin Cleveland**, for his advice, guidance, and seemingly everlasting patience. His intellectual curiosity and deep understanding of physical acoustics have been incredibly inspiring.

I would also like to give thanks to **Drs. Ben Turney** and **Karoline Schmitz** for their valuable insight into the medical aspects of my project.

Many thanks to **Dr. Mike Bailey** and his brilliant research team at the University of Washington for hosting me for two months and allowing me to be part of a long-lasting cross-institutional collaboration.

Furthermore, I am grateful to have worked with the brilliant members of the BUBBL Group, who contributed to my work in many ways: **Professor Constantin Coussious**, for always considering the bigger picture and creating the dream team; **Dr. Erasmia Lyka**, for being part of the dream team and her brilliant guidance on using PAM; **Joseph Blackmore**, for his help on creating beautiful figures and clear colourmaps; and **Valerio Pereno** and **Fabio Bianchi**, for excellent career and life advice. Furthermore, I would like to thank **Daphne Cunningham**, and the IBME workshop technicians, **James Fisk** and **David Salisbury**, for creating the most immaculate things from my most imperfect designs.

Many thanks to all of my friends from **Magdalen College** for broadening my horizon beyond my subject in the fantastic interdisciplinary space of the MCR.

A special thanks goes to **Maria Kempnich** for her exceptional advice and profound silliness.

Finally, I would like to acknowledge the **Engineering and Physical Science Research Council** and the **National Institute of Health** for financially supporting my research.

Contents

Abstract i

Acknowledgements ii

Nomenclature vii

1 Introduction 1

1.1 Kidney stone disease . . . 1
1.2 Musculoskeletal disease . . . 3
1.3 Shock wave generation . . . 4
1.4 Lithotripters, treatment, & monitoring . . . 7
1.5 Stone fragmentation . . . 9
1.6 Adverse bioeffects . . . 12
1.6.1 Cavitation as a mechanism for tissue damage . . . 13
1.7 Bubble dynamics during SWL . . . 14
1.8 Passive Acoustic Mapping . . . 17
1.9 Real-time stone tracking . . . 20
1.9.1 Pulse-echo ultrasound transducers . . . 21
1.9.2 B-mode ultrasound . . . 21
1.9.3 Hit/miss detection . . . 22
1.9.4 Time reversal . . . 23
1.10 Aim & thesis outline . . . 24

2 Tracking Stones using trilateration 25

2.1 Introduction . . . 25
2.2 Methods . . . 26
2.2.1 Trilateration algorithm . . . 26
2.2.2 Experimental setup . . . 28
2.2.3 Threshold detection . . . 30

2.2.4 Error minimisation behaviour . . . 32
2.3 Results . . . 34
2.3.1 Localisation accuracy . . . 34
2.3.2 Uncertainty estimation . . . 35
2.3.3 Number of transducers . . . 37
2.3.4 Moving targets . . . 38
2.4 Discussion . . . 39
2.5 Conclusions . . . 42

3 Characterisation of the EMS PiezoClast 43
3.1 Introduction . . . 44
3.2 Methods . . . 45
3.2.1 Acoustic field . . . 45
3.2.2 Cavitation detection . . . 47
3.3 Results . . . 50
3.3.1 Focal Pressure . . . 50
3.3.2 Cavitation detection . . . 54
3.3.3 Cavitation dynamics . . . 57
3.3.4 Cavitation dynamics of nanocups . . . 59
3.4 Discussion . . . 61
3.5 Conclusions . . . 65

4 PAM during SWL 67
4.1 Introduction . . . 67
4.2 Methods . . . 69
4.2.1 Experimental Setup . . . 69
4.2.2 Cavitation detection algorithm . . . 72
4.2.3 B-mode . . . 74
4.3 Effect of the energy level . . . 75
4.3.1 Representative signals . . . 75
4.3.2 Localisation of cavitation . . . 77
4.3.3 Peak detection times . . . 82
4.4 Effect of the SW rate . . . 85
4.5 Evolution of cavitation over time . . . 90
4.6 Cavitation detection during stone fragmentation . . . 93
4.7 Discussion . . . 102
4.8 Conclusions . . . 105

5 Conclusions **106**
5.1 Discussion 106
5.2 Future work 109
5.3 Conclusions 111

Bibliography **113**

Nomenclature

Acronyms

AMCD	Anti-miss-shot control device	
BWL	Burst wave lithotripsy	
CT	Computed tomography	
DORT	Decomposition of the time reversal operator	
DR	Detection rate	
ED	Energy density	$[\mathrm{J\,m^{-2}}]$
EL	Energy level	
FP	False positive	
HIFU	High intensity focused ultrasound	
MRI	Magnetic resonance imaging	
PAM	Passive acoustic mapping	
PCD	Passive cavitation detector	
PDF	Probability density function	
PRF	Pulse repetition frequency	[Hz]
QRR	Quantitative radionuclide renography	
RCB	Robust Capon beamformer	
RMS	Root mean square	
SW	Shock wave	
SWL	Shock wave lithotripsy	
SWT	Shock wave therapy	
TEA	Time exposure acoustics	
TRM	Time reversal mirror	
TR	Time reversal	

Symbols

D	Aperture	[m]
$D(\theta)$	Directivity at angle θ	[dimensionless]

$\bar{E}$	Mean square error	$[\mathrm{m}^2]$
I	Intensity	$[\mathrm{W\,m^{-2}}]$
J_1	Bessel function of order 1	
N	Number of elements	
X	Lateral direction of the lithotripter	[m]
Y	Lateral direction of the lithotripter	[m]
Z	Axial direction of the lithotripter	[m]
Z_0	Acoustic impedance	$[\mathrm{Pa\,s\,m^{-3}}]$
a	Radius	[m]
c	Speed of sound	$[\mathrm{m\,s^{-1}}]$
e	Error	[m]
f	Frequency	[Hz]
$f_\#$	f number	[dimensionless]
k	Wavenumber	$[\mathrm{rad\,m^{-1}}]$
m	Bimodal distribution weighting factor	
p	Pressure	[Pa]
$\tilde{p}$	Measured pressure	[Pa]
p^-	Peak negative pressure	[Pa]
p^+	Peak positive pressure	[Pa]
q	Source strength	$[\mathrm{kg\,s^{-2}}]$
$\tilde{q}$	Measured source strength	$[\mathrm{kg\,s^{-2}}]$
$\mathbf{r}$	Location vector	[m]
t	Time	[s]
t_C	Characteristic time	[s]
t_R	Rebound time	[s]
t_r	Rise times	
w_i	Weight of i^{th} element in beamforming	
$\vec{x}^\mathrm{S}$	Location vector of the stone	[m]
$\vec{x}_k^\mathrm{T}$	Location vector of k^{th} transducer	[m]
z	Axial distance	[m]
Δx	Transverse PAM resolution	[m]
Δz	Axial PAM resolution	[m]
λ	Wavelength	[m]
$\mathcal{N}(\mu, \sigma^2)$	Normal distribution with mean, μ, and standard deviation, σ.	
Π	Acoustic power	[W]
Ψ	Source energy	[J]
ρ	Density	$[\mathrm{kg\,m^{-3}}]$

1 Introduction

What necessitates better treatment monitoring during the therapeutic use of shock waves? In the first chapter, the research question is introduced by reviewing the relevant literature and applications of shock waves in treating kidney stones (SWL) and musculoskeletal disorders (SWT). The literature reveals that a high shock wave dose can result in tissue damage and that cavitation plays a major role in stone fragmentation and renal injury. An improved monitoring strategy for SWL is suggested by using real-time tracking of the stone, to reduce the number of shock waves. Then a method of detecting and mapping cavitation is developed, which can be used for feedback in SWL and SWT.

1.1 Kidney stone disease

Extracorporeal shock wave lithotripsy (SWL) is a non-invasive modality to treat kidney stones (also known as renal calculi) by fragmenting them into pieces small enough to be passed naturally [1]. Stones are formed in the kidney if minerals retained in the urine, come out of solution, and crystallise [2]. Normally, stones smaller than 2 mm can be passed naturally, but larger stones obstruct the ureter and cause severe pain and discomfort, and need to be treated [3]. The incidence of kidney stones in western societies has been increasing rapidly during last four decades [4], for example, the number of kidney stone related hospital episodes in the

UK in 2010 was 83,050, which was a 63 % increase over 2000 [5].

After the first patient was treated with SWL in 1980, SWL quickly became the preferred modality to treat kidney stones [1, 6–8]. By 1989, it was estimated that 87 % of all kidney stone patients in the United States were treated using SWL [9]. By the early 2000s however, a decline to only 50 % of all treatments has been reported [3]. The development of other minimally invasive procedures have contributed to the decline of SWL, for example the number of ureteroscopic stone treatments (including ureteroscopic laser fragmentation and extraction of the stone) increased by 127 % from 2000 to 2010 in the United Kingdom [5]. It has been suggested that with growing confidence in endoscopic procedures, the share of patients treated with SWL will decline even further [10, 11].

SWL is generally considered safe, but concerns about renal injury due to shock waves (SW) have been raised since the late 1980s [12]. Studies have shown that almost all patients suffer from acute effects such as hematuria and 2 % to 20 % of all patients experience subcapsular hematomas [13, 14]. In rare cases, renal failure can also occur [15, 16]. Adverse chronic effects, such as a new onset hypertension and recurring stone disease, have also been suggested by some studies [17, 18]. Studies in animals and patients indicate that adverse bioeffects in the kidney increase with the number of SWs delivered [19–21], the rate of SW delivery [22, 23], and the SW energy level [24]. If the number of SWs could be reduced without affecting outcomes, the level of injury to the kidney should therefore decrease.

Stone motion due to respiration and due to patient motion during the procedure mean that a fraction of the SWs miss the stone when it is outside the lithotripter focus, when the SW is fired. Therefore, more SWs are delivered than needed to fragment the stone sufficiently [25]. A system to facilitate accurate alignment throughout the procedure will reduce the number of shocks delivered, and hence, reduce adverse effects [22, 26].

1.2 Musculoskeletal disease

Other uses of SWs in clinical practice have emerged since the introduction of SWL [27]. In shock wave therapy (SWT) SWs have been shown to be effective to treat musculoskeletal disorders including plantar fasciitis [28–31], calcific tendinitis [32, 33], insertional Achilles tendinopathy [34–36], and chronic pelvic pain syndrome [37–42]. However, some studies have failed to show significant improvements over placebo [43–46] or have shown that conventional treatments might be more effective [47, 48]. A systematic review of 106 clinical studies in SWT found that 84 % report a statistically significant improvement over placebo, suggesting that SWT can be effective [49].

The mechanisms by which SWs result in their therapeutic effects are not well understood. The possible mechanisms are often linked to the acoustic energy of the SW per unit area, commonly referred to as the energy flux, the energy density, the energy flux density, or the pulse intensity integral [50]. In this work, the term energy density (ED) will be used, as it is common in the SWT community. Possible mechanisms include an increase in nitric oxide production that can have an anti-inflammatory effect, which has been linked to energy densities (ED) of $\sim$0.03 mJ mm^{-2} [51]. Neovascularisation, a tissue repair process due to the formation of new capillaries, can be enhanced by applying SWs with higher EDs, on the order of 0.2 mJ mm^{-2} [52–54]. In clinical studies EDs ranging from 0.02 mJ mm^{-2} to 0.7 mJ mm^{-2} have been delivered [49]. However, a specific, effective SW dose or treatment protocol for a given disorder is yet to be determined.

1.3 Shock wave generation

SW sources use electrohydraulic, electromagnetic, or piezoelectric excitation to form a high-amplitude positive-pressure (compressional) shock front followed by a negative-pressure (rarefactional) tail, as shown in figure 1.1A [50]. The positive-pressure phase has a peak of up to 150 MPa and a duration of 1 µs. The negative-pressure tensile tail follows with a peak amplitude of 10 MPa and a duration of 5 µs [55]. In theory, the rise-time of SWs, defined as the time it takes for the pressure to rise from 10 % to 90 % of the peak-positive pressure, predicted by the Taylor shock profile, is less than 1 ns [56]. Rise-times of this order are too short to measure with current hydrophones as they do not have a sufficiently short response time.

Electrohydraulic sources (figure 1.1B) use a spark gap placed in water at the first focus (F1) of a hemi-ellipsoidal reflector. A potential difference of 10 kV to 30 kV is applied to the spark gap, which results in a breakdown of water and an expanding vapour bubble to produce a spherically spreading shock front. The wave is reflected and focused onto the geometric focus of the ellipse at F2. The repeated violent bubble collapses at the spark gap erode the electrodes requiring a replacement every 1000 to 2000 SWs to avoid alterations in the acoustic output [57, 58]. One manufacturer has addressed this issue by encapsulating the electrodes to ensure longer life-times [59]. Electrohydraulic sources have also been employed in SWT using machines produced by Medispec [60, 61], HMT [62, 63], and others.

Electromagnetic lithotripters use an electrical coil placed in close proximity to a metal plate. A short electrical pulse through the coil generates a repulsive force in the metal plate. The motion of the plate results in the generation of an acoustic wave. Different manufacturers use one of two configurations to focus the waves onto the target. Storz lithotripters (figure 1.1C) generate an outward-travelling cylindrical wave that reflects from a parabolic reflector and is reflected and focused

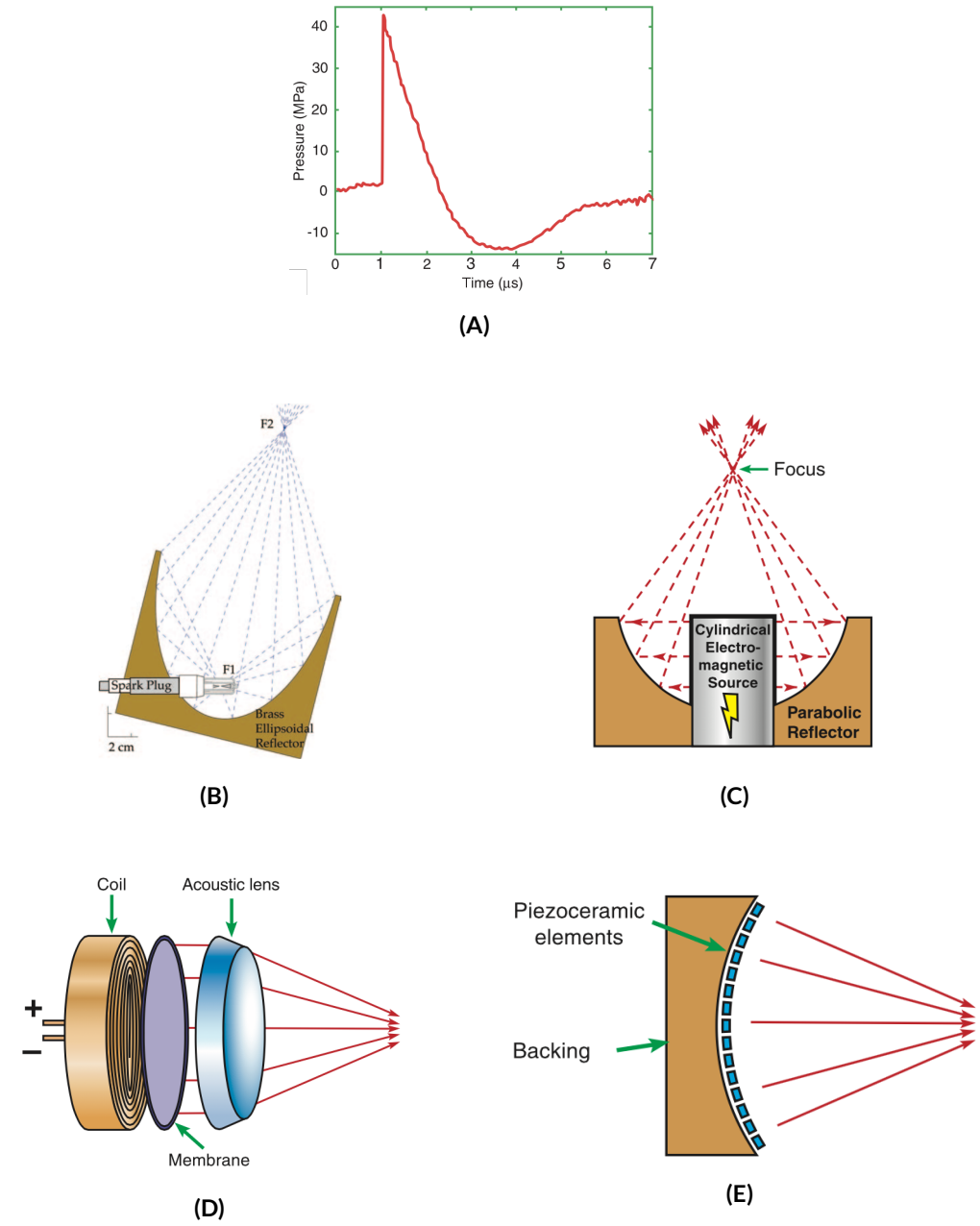


Figure 1.1: (A) Representative acoustic output from a shock wave source; and schematic diagrams of (B) an electrohydraulic source with an interior focus at F1 and an exterior focus at F2; (C) an electromagnetic source focusing through a parabolic reflector; (D) an electromagnetic source focusing through an acoustic lens; and (E) a piezoelectric source with elements arranged on a hemi-spherical bowl of a spherical cap to focus on the geometric focus. Figures reproduced from [11] and [50].

on a point [50]. Dornier and Siemens lithotripters (figure 1.1D) generate a quasi plane wave and use an acoustic lens to focus the acoustic energy [64]. It is noted that in neither electromagnetic configuration, waves form a shock at the source. However, non-linear distortion along the path can create a shock wave at the focus. Due to a life-time in excess of 1 million SWs, electromagnetic lithotripters are the most frequently used machines for lithotripsy [65]. Smaller electromagnetic sources that can be used in an orthopaedic setting are also frequently used in SWT [43,66,67].

Piezoelectric sources (Figure 1.1E) consist of an array of up to 3000 piezoceramic elements arranged on a hemispherical bowl of a spherical cap. The sound emitted simultaneously from all elements focuses the energy at the geometric focus due to constructive interference. Similar to electromagnetic lithotripters, a shock wave is not generated at the source, but non-linear distortion along the path results in a SW at the focus. Although piezoelectric sources use backing to avoid ringing in the piezoceramic elements beyond the initial pulse, a short ring-down period is inevitable [65,68]. Smaller, hand-held piezoelectric sources have also been employed in SWT as focused sources [45,69,70].

Radial, or ballistic sources, have a compressed air chamber to accelerate a projectile towards an applicator that is pressed against the skin to generate a radially spreading pressure wave [35]. These sources are used in SWT. The pressure waves produced by these devices do not resemble a SW similar to those observed in SWL [71]. The positive pressure phase lasts for around 4 µs and reaches a peak positive pressure of 8 MPa with EDs up to 0.18 mJ mm^{-2} [72]. Furthermore, the radially spreading wave does not form a cigar-shaped −6 dB focal region but rather a region of maximum pressure at the applicator [71]. To facilitate the aforementioned therapeutic effects of both, focused sources producing high EDs and radial sources producing low EDs, dual mode operation devices combine an electromagnetic with a radial therapy head [73]. Furthermore, dual mode devices can treat both regions close to the surface of

the skin and bone calcifications that are located deeper in the body.

1.4 Lithotripters, treatment, & monitoring

The Dornier HM3, the first clinical lithotripter, had a electrohydraulic source placed at the bottom of a water bath, and thus, patients were immersed in water to avoid an impedance mismatch between air and tissue. The stone was alinged using fluoroscopic imaging and local sedation or even anaesthesia was necessary to perform the procedure [6, 74, 75].

Changes in the second generation of lithotripters focused on improving stone localisation and monitoring, employed electromagnetic and piezoelectric SW generation [76]. Ultrasound imaging was introduced for real-time monitoring and water baths were eliminated in favour of a coupling cushion. Dry lithotripters have a source placed in a therapy head under a bed or on an arm coupled to the patient through a membrane using coupling gel [77]. Moreover, the aperture of the sources was increased to reduce the pain at the entry point of the wave front on the surface of the body, and thus, the energy is spread over a larger surface area and anesthesia is no longer necessary [78].

Third generation lithotripters built upon these advancements to achieve more practical designs; machines have become modular, combine localisation systems from ultrasonic and fluoroscopic imaging, allow for a wide range of energy settings, and have even larger apertures to reduce pain at the entry point even further [65]. SWL has evolved from a complex in-patient procedure to a routine ambulatory walk-in/walk-out treatment option. Somewhat remarkably however, the acoustic signature of lithotripters has remained almost very similar to that employed on the first lithotripter [11, 50].

The design alterations of second and third generation lithotripters facilitate a more user friendly experience for both clinicians and patients alike, but by considering the physical acoustics, the cost is revealed. Water-bath lithotripters transmit 99 % of the acoustic energy into the body. But trapping air pockets between the membrane of a dry lithotripter and the patient leads to significant energy reflection [79, 80]. It has been suggested that trapping air pockets on 6 % of the membrane surface area decreases stone breakage by 50 % [79]. Furthermore, coupling degrades during one treatment due to motion and repositioning of the patient. Currently, doctors can only rely on visual verification to avoid air pockets.

Increasing the aperture of the source has led to a smaller focal region and higher peak-pressures. The Dornier HM3 has a peak-positive pressure of 45 MPa and a focal spot diameter of 15 mm [55]. The Storz Modulith SLX, however, has a peak-positive pressure of more than 100 MPa and a focal diameter of only 4 mm [81]. From one perspective, the use of smaller focal volumes is justified as it should result in more energy delivered to the kidney stone and in less damage to the soft tissue surrounding the stone. But modern lithotripters do not appear to reduce re-treatment rates or produce better stone fragmentation [82]. However, in clinical practice, the narrower focal volume of a modern lithotripter could miss the stone more frequently due to stone motion in the kidney [25]. Note, the definition of the focal region is the contour where the pressure is 6 dB less than the maximum pressure and it follows that even outside the focal region of a Storz Modulith, higher pressures than the peak-pressure of a Dornier HM3 can be achieved, and thus, evaluating focal dimensions, which are only relative to each design, can be misleading.

Fluoroscopic and ultrasonic imaging are used to align the focus of the lithotripter with the stone. Lithotripters have an X-ray source and detector mounted on a C-arm. The C-arm rotates around the patient to locate the stone in three dimensions. Due to the ionising radiation emitted by fluoroscopy, the stone cannot be monitored

continuously during treatment. Consequently, the stone is initially located within the kidney, the focus of the lithotripter is aligned, and then delivery of a fixed number of SWs (typically 500) occurs before the alignment is confirmed again using fluoroscopy. In-line and out-of-line ultrasound imaging can be used to verify the position of the stone in real-time, in addition to aligning the stone initially. However, robust identification of stones in B-mode imaging is challenging [83]. Furthermore, it has been suggested that ultrasound imaging for SWL requires a long training period [84]. Utilising the twinkling artefact has been suggested to better image stones in the kidney [85, 86]. The artefact appears in colour Doppler, highlighting some stones as coloured spots on B-mode, as will be described in more detail later.

More recently in 2015, Burst Wave Lithotripsy (BWL), a new method of non-invasively fragmenting kidney stones, was introduced by Maxwell et al. [87]. Rather than using SWs, stones are exposed to a broadly focused short burst of ultrasound with an operating frequency of 170 kHz, 285 kHz, or 800 kHz, and a focal peak pressure of up to 6.5 MPa. After treating stones in vitro for up 14.7 min, stones had been fragmented sufficiently to less than 1 mm [87]. To monitor the procedure in vivo, an in-line B-mode ultrasound imaging system and a twinkling artefact in colour Doppler is used [88].

1.5 Stone fragmentation

The mechanisms leading to stone fragmentation during SWL are still a matter of debate and the proposed ideas are shown in figure 1.2. The main mechanisms contributing to stone fracture appear to be cavitation and stress waves.

Patients with stones ranging from 3 mm to 10 mm are commonly treated with SWL. The acoustic properties of kidney stones vary between stone types. For example,

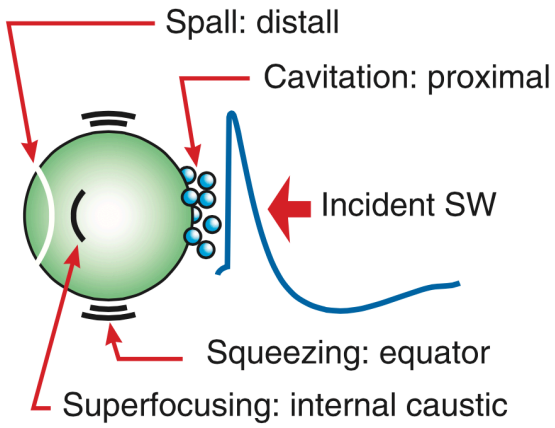


Figure 1.2: Schematic drawing to illustrate the main mechanisms leading to stone fracture and the regions they act on. Figure reproduced from [50].

calcium oxylate monohydrate stones have been reported with densities between $1800\,\mathrm{kg\,m^{-3}}$ and $2000\,\mathrm{kg\,m^{-3}}$ and longitudinal sound speeds from $3000\,\mathrm{m\,s^{-1}}$ to $4500\,\mathrm{m\,s^{-1}}$ [89–92]. These speeds exceed both, the speed of sound in the surrounding fluid and in the soft tissue, that ranges from $1450\,\mathrm{m\,s^{-1}}$ to $1580\,\mathrm{m\,s^{-1}}$.

Squeezing As the speed of sound in kidney stones is faster than in the surrounding liquid [90], the shock is propagating slower outside the stone, and thus, a circumferential force around the stone equator is developed. The circumferential quasistatic compression or "squeezing" results in tensile forces at the proximal and distal ends of the stone [93]. Therefore, it was concluded that wider, low-pressure foci would facilitate stone fragmentation and a suitable lithotripter for that purpose was designed [94].

Cavitation The rarefractional pressure-tail of a SW has an amplitude of 10 MPa and a duration of 5 µs [55]. Gas or vapour cavities are formed in the urine surrounding the stone and, due to the incident SW, grow several times larger than their initial size and collapse after a prolonged expansion phase [95]. For bubbles on the proximal wall of the kidney stone a high-speed microjet is emitted, which will impact the stone at speeds greater than $100\,\mathrm{m\,s^{-1}}$ [96, 97]. Furthermore, a SW

is emitted during the collapse, and bubble clusters are formed at the proximal wall of the stone as shown in figure 1.2. The collapse of the cluster amplifies the contribution of inertial cavitation on stone fragmentation [98]. However, bubble clouds, which form proximal to the stone due to multiple bubbles interacting and merging together, might also shield the target during the treatment. Clouds have primarily been observed at SW rates greater than 1 Hz [11].

Stress Waves Stones are elastic solids that can support both, shear and normal stresses as the SW couples into them [99]. Due to the properties and the geometry of kidney stones, it is shear waves that the SW couples into most efficiently. These can generate shear and tensile stresses that result in fragmentation [100].

Spall Fracture Solids are usually weaker in tension than in compression. The incident SW undergoes an anti-phase reflection at the soft boundary at the distal wall of the stone, and the resulting tensile stress induces spallation [84]. However, it has been suggested that spallation is only a minor contributor to stone fragmentation [101].

Superfocusing In canonical shapes such as spheres all of the internal waves can result in local focusing, which will result in locations of the highest stress, and hence, regions where stones might fail mechanically [102, 103]. The geometry of the stone facilitates such stresses through superfocusing. That is, as the wave reflects from the distal wall of the stone, it is focused by refraction, due to the difference in speed of sound between the surrounding tissue and the stone, and diffraction from the corners of the stone. Although superfocusing can occur in cylindrical stone models, realistic stone geometries do not cause superfocusing [50].

1.6 Adverse bioeffects

Although SWL is generally considered safe, it does induce trauma to tissue, for example 63 % to 85 % of patients show signs of renal trauma if evaluated with computed tomography (CT) or magnetic resonance imaging (MRI) post-treatment [12, 104, 105]. Another study examined acute effects on the kidney due to SWL using excretory urography, quantitative radionuclide renography (QRR) and MRI, and found that in 74 % of the patients one or more tests revealed abnormalities in morphology or kidney function [13]. Previously, Lingeman and Newmark [106], and McAteer and Evan [14] reviewed tissue damage due to SWL in detail. A spectrum of adverse bioeffects, covering acute renal injury and chronic long-term effects, will be discussed here.

The most common consequence of lithotripsy is haematuria (blood in the urine), which occurs in patients after receiving roughly 200 SWs. In the great majority of patients, haematuria resolves within a few days or at most weeks and is reported as an incidental finding [107]. The blood in the urine is due to the incident SWs rupturing blood vessels [108]. Morphological studies on animal models have shown pathological effects on renal tissue and confirmed haemorrhages [19]. Studies on a pig model have shown a reduction in renal function due to haemorrhages by 5 % to 6 % following a typical dose of SWs [23, 26, 109].

Hematomas are localised collections of blood outside of blood vessels and were observed in less than 1 % of all patients, examined with ultrasonography post-treatment, in a study investigating 1012 SWL treatments from 1980 to 1984 [110]. However, examining injury using MRI revealed a hematoma rate of 29 % in a different study [13]. Several other studies have since confirmed hematomas as a consequence of SWL [107]. While most of them resolve naturally within weeks without any long-term effects on renal function, some can persist for months or even

years [111]. Rare case studies have also reported acute renal failure due to subcapsular hematomas or complete renal failure [15, 16].

Potential long-term bioeffects due to SWL include new onset hypertension [112]. Studies have reported the incidence of hypertension in 8 % to 17.5 % of patients following SWL, where higher rates have been associated with older patients [17, 113]. Measuring the renal vascular resistance before and after SWL has shown a significant age-dependent increase due to SWL and has suggested age as a significant risk factor [17, 114]. Recurring stones with a transformed mineral composition is a further long-term complication. Patients, who have a calcium oxalate stone and who have received a greater number of lithotripsy treatments, are more likely to develop recurring calcium phosphate or brushite stones [18, 115]. Brushite is a mineral that responds rather poorly to SWL [107].

1.6.1 Cavitation as a mechanism for tissue damage

Acoustic cavitation was first observed in lithotripsy in 1987 and refers to the creation of vapour and/or gas cavities in the fluid due to the tensile phase of the wave exceeding the threshold in tissue [96]. Cavitation has been established as a dominant source of tissue damage [116, 117]. Experiments have shown that damage is significantly reduced when cavitation is reduced or suppressed [116, 117]. Previously, the contribution of cavitation, collapsing bubbles and resulting microjects to stone fragmentation was discussed. However in tissue, the absence of a rigid surface precludes jetting. Instead, it has been shown that cavitation in a vessel results in focal invagination will deform vessels and potentially rupture them [118]. Other studies have shown that the explosive growth of the bubble has the potential to rupture capillaries [119]. That is, capillaries due to their small size are subjected to greater stresses and fail first [120, 121]. As blood escapes the vessels, more cavitation nuclei

are available and the probability of cavitation is increased significantly [122, 123]. Thus, cavitation detection may be a useful measure to monitor the potential for adverse effects during lithotripsy.

It has also been proposed that inhomogeneities in speed of sound in the millimetre scale in tissue can result in another source of injury. The wave will distort as it is passing through tissue and induce shear [50]. Shear stresses are also created due to the short rise time of SWs leading to non-uniform straining of the tissue. Shear stress of this order could contribute to tissue damage [124, 125].

Animal models have been used to show that number, intensity, and rate of shocks have a significant effect on renal trauma. Delius et al. [126] used a canine model to show that after a threshold of 500 to 1500 delivered shocks, larger and more frequent parenchymal haemorrhages are observed, while no difference between 1500 and 3000 SWs could be seen [126]. Further evidence for renal injury due to a supraclinical dose of 8000 SWs was determined by using a pig model [21]. It has also been shown that the size of the lesion increases with the SW intensity when delivering 2000 SWs to a pig model [24]. The effect of the SW rate has also been shown to affect the renal injury in canine and porcine models. In dogs it was shown that SWs at 100 Hz create more hemorrhages and larger hematomas than SWs at 1 Hz [22]. Similarly, a pig model was used to show that reducing the SW rate from 2 Hz to 0.5 Hz reduces the renal injury [23]. Thus, a real-time monitoring system could suggest a reduction of the rate, if, for example, an excess of cavitation was detected, to limit renal injury.

1.7 Bubble dynamics during SWL

Acoustic cavitation occurs when the SW pulse interacts with pre-existing, macroscopic gas bubbles in the fluid, which will nucleate acoustic cavitation if their surface

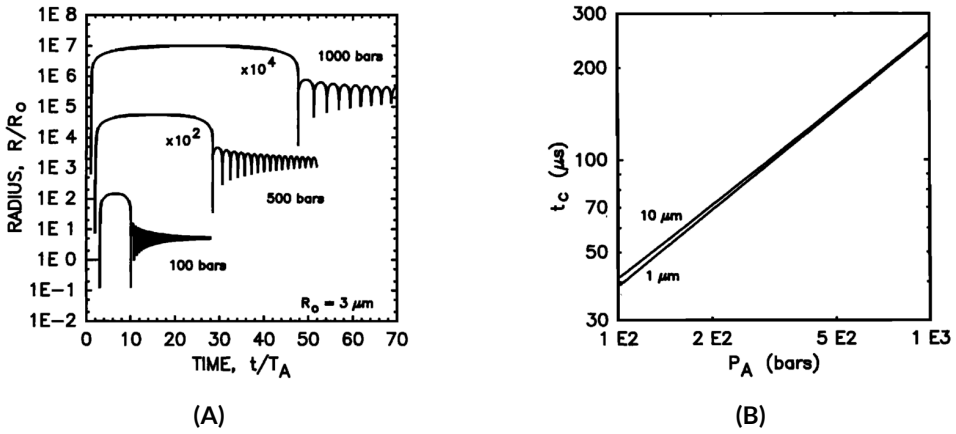


Figure 1.3: Modelling the bubble dynamics due to a single SW pulse: (A) calculated time-radius curves for three different peak positive SW amplitudes, where $T_A = 12\mu$s, R is the instantaneous radius and R_0 is the initial radius of the bubble; and (B) relationship between the peak positive driving pressure, P_A, and the characteristic time, t_C of a bubble for two different initial bubble radii. The ratio of peak positive to peak negative pressure was fixed at 3.1 and 6.25 in panels (A) and (B), respectively. Both figures reproduced from [127].

tension does not hinder growth [127]. The presence of cavitation during SWL was first reported in 1987 [96]. A thin x-ray film was exposed to SWs at the focus of a lithotripter and numerous spots were detected as a result of microjets emitted by violently collapsing bubbles on the hard surface. Subsequently, the Gilmore-Akulichev model was used to determine the bubble dynamics due to an incident SW [127]. Figure 1.3A shows the time-radius curves of a 3 µm bubble as it is impacted by SWs of different amplitudes (where $T_A = 12\mu$s). The SW in all cases has a compressive duration of 1 µs and a tensile tail lasting 6 µs. The compressive pressure of the SW crushes the cavity to $\frac{1}{10}$ of its initial size and a broadband emission is recorded. Afterwards, the bubble expands due to the tensile pressure of the SW and remains enlarged at more than 100 times its initial radius until the inertia of the fluid crushes the bubble and a second broadband pulse is emitted up to 600 µs later. This characteristic time, t_c, i.e. the time from bubble growth to the initial collapse, depends on the amplitude of the source and is not very sensitive to the initial bubble radius as shown in figure 1.3B. A distinguishing characteristic of the cavitation is that the collapse occurs much later than the duration of the SW [127].

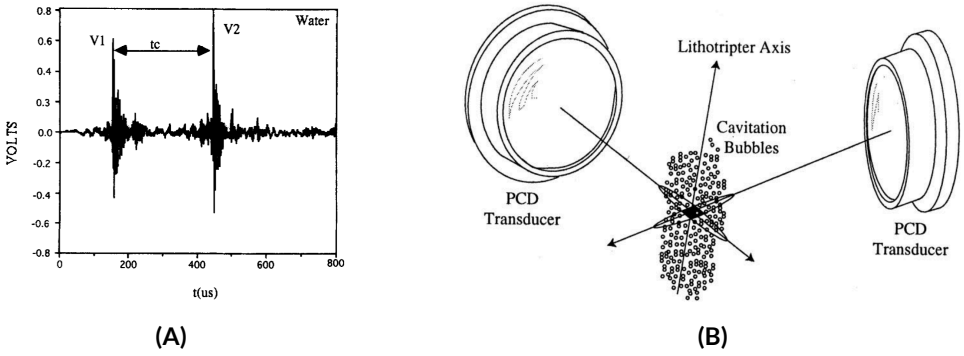


Figure 1.4: Cavitation detecting during SWL: (A) Pressure radiated from a bubble cavitating due to a single SW pulse indicating the characteristic time, t_C; (B) schematic drawing to illustrate dual passive cavitation detectors, which are placed orthogonal to each other and aligned confocally. Figures reproduced from [122] and [128].

Experiments in water tanks have confirmed the acoustic characteristics of bubble growth, collapse and rebound during SWL and detected the acoustic emissions from these events using transducers, commonly referred to as passive cavitation detectors (PCD) [122,128,129]. Figure 1.4 shows a signal corresponding to cavitation recorded on a PCD and a setup with two confocally aligned PCDs to localise cavitation in space. It can be seen that experimentally the characteristic "double-bang" from growth and collapse of the bubble can be detected and a characteristic time in the order of 100 µs is obtained [122]. However, in order to localise the emissions spatially, more than one detector is needed. As shown in figure 1.4B, two orthogonal PCDs can be aligned confocally such that the overlapping focal volume is 5 mm in diameter. By using coincidence detection of the characteristic acoustic emissions of bubble growth and collapse, cavitation can be localised to be within the confocal region [123, 128, 130]. Cavitation has also been detected in pig kidneys in vivo [123, 130] and in patients [122]. It was shown that cavitation occurs during SW treatment in the collecting system and in the renal tissue using a dual PCD system that was confocally aligned with a Dornier HM3 electrohydraulic lithotripter and a pig model [130].

1.8 Passive Acoustic Mapping

The current state of the art in SWL is to use single or dual PCDs to detect cavitation, which gives limited spatial information. If a map of cavitation can be generated then it might be possible to differentiate between useful cavitation around the stone and harmful cavitation in the parenchyma. In the later case parameters such as the amplitude or the rate could be used to reduce tissue damage.

Passive acoustic mapping (PAM) is a technique that has previously been used to monitor cavitation during high intensity focused ultrasound (HIFU) treatment [131]. Its principles are rooted in passive sonar [132] and in mapping sources of seismic acoustic emissions [133]. PAM uses an array of passive detectors, commonly a conventional B-mode ultrasound probe, to passively listen to acoustic emissions [131]. The energy at each voxel within a pre-defined two dimensional grid is determined by beamforming the signals recorded on the array. PAM has been used to monitor ablation [134], to estimate the temperature rise in tissue [135], and in drug delivery applications [136, 137].

Five steps are necessary to generate a PAM frame: (i) grid definition, (ii) recording acoustic emissions, (iii) filtering recorded signals, (iv) beamforming, and (v) source energy estimation:

(i) The area of interest is defined through a two-dimensional grid that lies in the plane of the diagnostic array used to monitor acoustic emissions. The source strength will be determined for every pixel of the grid. The location and size of the focus of the therapeutic source should be considered to define the grid size. In this work, the theoretical resolution was used to guide for the spacing in the grid but other factors, such as the computational time that increases with a smaller grid spacing, should also considered.

The theoretical spatial resolution of PAM depends on the point spread function of the imaging array. Using the $-3\,\mathrm{dB}$ width that corresponds to the minimum separation to resolve two distinct points, the transverse, $\Delta x_{-3\mathrm{dB}}$, and axial resolutions, $\Delta z_{-3\mathrm{dB}}$, for a linear array with an aperture D and a centre frequency corresponding to the wavelength λ are [138]

$$\Delta x_{-3\mathrm{dB}} \approx 0.89 f_{\#} \lambda \tag{1.1}$$

$$\Delta z_{-3\mathrm{dB}} \approx 6.95 f_{\#}^2 \lambda, \tag{1.2}$$

where for a distance z between the source and the linear array

$$f_{\#} = \frac{z}{D}. \tag{1.3}$$

In theory, these expressions require a narrowband acoustic signal with a wavelength λ and suggest a dynamic grid that varies along z, however for simplicity, the centre frequency of the array and a constant spacing throughout the grid was used in this work.

(ii) The acoustic emissions from the region of interest are recorded on all elements of the array. These signals potentially include the emissions of interest, for instance due to cavitation, scattered signal from the source, and interference.

(iii) By applying a frequency filter to each of the signals that have been recorded, the broadband emissions from cavitation can be isolated from the narrowband source frequency and its harmonics in HIFU. However, in SWL and SWT both, source and cavitation signals are broadband. We found it to be necessary to add additional steps to isolate the cavitation signal due to SWs.

(iv) A beamformer is a spatial filter to utilise the aperture of an array of receivers to separate sound sources in space [139]. For a compact sound source the

received pressure field, p, at location $\mathbf{r}'$ and time t is

$$p(\mathbf{r}',t) = \frac{q\left(\mathbf{r}, t - \frac{|\mathbf{r}'-\mathbf{r}|}{c}\right)}{4\pi|\mathbf{r}'-\mathbf{r}|}, \tag{1.4}$$

where the source is at location $\mathbf{r}$ with strength q propagating through a medium with speed of sound c and assuming linear propagation, and neglating higher order terms and viscous effects [140].

Given measurements of the pressure field, $\tilde{p}$, due to multiple simple sound sources, the signal can be back-propagated and summed to reject noise and interference to estimate the source strength

$$\tilde{q}(\mathbf{r},t) = \frac{1}{N}\sum_{\mathrm{i}=1}^{N} w_{\mathrm{i}} 4\pi|\mathbf{r}_{\mathrm{i}}-\mathbf{r}|\tilde{p}\left(\mathbf{r}_{\mathrm{i}}, t + \frac{|\mathbf{r}_{\mathrm{i}}-\mathbf{r}|}{c}\right) \tag{1.5}$$

for an array with N receivers, where the i^{th} receiver is located at $\mathbf{r}_i$ [138]. Given the location of all receivers in the array, the differences in the time of arrival from each receiver to each voxel in the grid is used to delay-and-sum [131].

Furthermore, beamformers can apply a weight, w_{i} to the signal that is received on individual elements of the array. In non-adaptive beamformers, such as Time Exposure Acoustics (TEA), the value of the weights are constant and not adapted to the data [133], which results in large artefacts in PAM [141]. These artefacts are due to inaccuracies in the locations of the receivers, varying array element sensitivities, and interference between multiple sound sources.

To achieve a better spacial resolution in PAM, the weights can also be optimised for each receiver array by using data-adaptive beamformers [141]. The Capon Beamformer [142] and the Robust Capon Beamformer (RCB) [143,144] have been applied to PAM for this purpose and used experimentally in vitro and in vivo [141]. However, the improvements in spatial accuracy carry a

computational cost. Throughout this work, RCB has been used for PAM.

(v) The source power and energy can be determined from the strength that was defined in Eq. (1.4) by assuming a plane wave, i.e. that the receivers are in the far-field, and by using the definitions of acoustic intensity, I, and acoustic power, Π, [138, 145]

$$I(\mathbf{r},t) = \frac{\tilde{p}^2(\mathbf{r},t)}{\rho_0 c} = \frac{\tilde{q}^2\left(\mathbf{r}', t - \frac{|\mathbf{r}-\mathbf{r}'|}{c}\right)}{\left(4\pi|\mathbf{r}-\mathbf{r}'|\right)^2 \rho_0 c} \tag{1.6}$$

$$\Pi(\mathbf{r}',t) = 4\pi|\mathbf{r}-\mathbf{r}'|^2 \frac{\tilde{p}^2(\mathbf{r},t)}{\rho_0 c} = \frac{\tilde{q}^2\left(\mathbf{r}', t - \frac{|\mathbf{r}-\mathbf{r}'|}{c}\right)}{4\pi\rho_0 c}. \tag{1.7}$$

Finally, by integrating the source power over time, the source energy, Ψ, is obtained

$$\Psi(\mathbf{r}) = \int_{t_0}^{t_0+T} \frac{\tilde{q}^2\left(\mathbf{r}', t - \frac{|\mathbf{r}-\mathbf{r}'|}{c}\right)}{4\pi\rho_0 c}\, dt. \tag{1.8}$$

1.9 Real-time stone tracking

During SWL, kidney stones move due to respiration and patient movement. Due to misalignment, it has been esitmated that 40 % of all SWs miss their target [83]. Given the benefits of reducing the treatment dose, several attempts at a clinically viable system to track stones in real-time have been made [85, 86, 146–155]. Acoustic concepts lend themselves to be used during the treatment because in contrast to fluoroscopy, no harmful ionising radiation is emitted during ultrasound. Furthermore, penetration depths large enough to monitor the kidney can be achieved using ultrasound in the megahertz frequency range.

1.9.1 Pulse-echo ultrasound transducers

As early as 1984, Chaussy et al. considered employing a single ultrasound transducer in the semi-elliptic reflector of a spark lithotripter to locate kidney stones acoustically [156]. Unsuccessful attempts however, led them to revert to the radiological monitoring system using two X-ray sources aligned such that their axes intersect at the second focus of the lithotripter. Towards the end of the 1980s, the disadvantages of using an X-ray imaging system were addressed and utilising two ultrasound transducers driven in pulse-echo mode to monitor the procedure was suggested [146].

In an effort to reduce missed shots, an *anti-miss-shot control device* (AMCD) was deployed on a piezoelectric lithotripter [147]. AMCD operates the piezoceramic elements of the lithotripter in either a low-voltage (imaging) regime or a high-voltage (treatment) regime, where the low-voltage signal generator is also connected to an echo receiver. By emitting a probing ultrasonic pulse and listening to the echo from the stone, the location for the maximum echo levels can be determined and the SW triggered. As a result, reduced bleeding and improved stone fragmentation were observed in a canine model [147]. AMCD can be extended beyond piezoelectric lithotripters if an imaging probe is added.

1.9.2 B-mode ultrasound

In-line B-mode ultrasound imaging is clinically used to verify the stone location in real-time. Several image processing algorithms have been suggested to track kidney stones on B-mode images and to align the SW focus and target. Four image processing algorithms were compared and clinical tests to access their efficiencies were presented [148]. For common cases, the algorithm tracked the motion of the gallstone throughout the treatment but, in more difficult cases however, the efficiency of the

treatment could not be improved through tracking. Furthermore, by using a block matching algorithm to determine the location of kidney stones in real-time, 40 % fewer shocks were necessary to fragment kidney stones through tracking [149, 150]. Similarly, an algorithm was designed to compute stone trajectories in patients [151]. The trajectories were used in ex vivo and in vitro models to move stones using a computerised positioning stage and, by tracking the stone during lithotripsy, the number of SWs was reduced by half [152]. Furthermore, all of the tracked objects were pulverised to less than 1 mm compared to 55.3 % for untracked stones. The algorithm was improved further by making it more robust later [154].

"Twinkling" artefacts on Doppler ultrasound have also been employed for tracking purposes [85, 86]. "Twinkling" occurs in hyper-echoic regions on colour Doppler, and thus, kidney stones appear as bright-coloured spots [157]. It has been suggested that the twinkling artefact might be due to bubbles trapped in cracks and crevices on kidney stones [158, 159]. The strong contrast between stones and tissue on colour Doppler can be facilitated to develop further tracking algorithms.

Such image processing algorithms demonstrate the utility of tracking, but they rely on B-mode ultrasound imaging, which is not a robust method of finding stones, for example, sensitivity values range from 19 % to 93 % and specificity values from 84 % to 100 % for detecting stones using B-mode ultrasound [86]. It appears that reliance on B-mode has been a barrier to clinical translation.

1.9.3 Hit/miss detection

To determine the efficiency of SWL, real-time detection systems that determine whether a SW hit the stone or missed the target have been investigated. Such systems are not useful to track the stone as they only provide information *after* a SW has been triggered. Yet, valuable information can be gained through hit/miss

detection to estimate the appropriate SW dose.

A Doppler shift due to stone fragments and micro-cracks was observed, and thus, spectral Doppler ultrasound was utilised to differentiate hits and misses [153]. Furthermore, a characteristic resonant acoustic scatter is emitted when stones are hit during SWL. Thus, a broadband receiver was employed close to the lithotripter to detect successful shots as passive system to monitor SWL in real-time [155]. It was concluded that such a system could be facilitated to determine whether stones have been fragmented sufficiently to be passed naturally. A similar concept was presented by Leighton et al. to evaluate the efficiency of SWL by classifying shocks as "effective" or "ineffective" [119]. The system presented had a sensitivity of 91.7 % and a specificity of 100 %.

1.9.4 Time reversal

Time reversal (TR) has been developed as a method to localise targets rather than imaging the body. That is, lower frequency sound can be used for TR such that the response from the stone behaves similarly to that of a point scatterer. Initially, it was used to auto-focus through an inhomogeneous medium such as tissue as waves distort in aberrating media [160, 161]. TR uses the individual elements in an array as the time reversal mirror (TRM). The elements transmit a pulse and receive a scattered signal. The echo is recorded on all channels and stored in the digital memory. The signals are emitted in reverse and will autofocus on the target. In multi-target media, repeated use of a TRM will iterate and converge on the most reflective target [160, 161]. Experimental results to support this claim were presented in a study where the TRM was used to focus on a kidney stone through an inhomogeneous medium [162]. By applying time reversal to a piezoelectric lithopripter, the focus of the SW can be moved such that a stone is targeted. Later experiments revealed

the possibility of focusing on a moving gall bladder or kidney stone embedded in a surrounding inhomogeneous medium [163].

By using the decomposition of the time reversal operator (D.O.R.T.), the technique was extended to detect targets and to focus selectively on two or more scatterers [164]. In the D.O.R.T. method, an eigenvector of the time reversal operator is identified for each scatterer. To focus, the corresponding eigenvector is transmitted through the medium [164].

1.10 Aim & thesis outline

Although monitoring during SWL has continuously improved, almost four decades after its introduction into clinical practice, adverse effects are still observed routinely in SWL. Thus, the aim of this work is to present two further monitoring modalities that would reduce tissue damage.

First, a system to track kidney stones in real-time using a trilateration algorithm is shown in chapter 2. To achieve the most accurate localisation, the elements are placed on the edge of the lithotripter aperture. Thus, the angular resolution of the system is maximised. Furthermore, elements with a centre frequency of 0.5 MHz are used to reduce attenuation of the signal.

Second, PAM is modified to detect cavitation during SWT and SWL. In chapter 3 the characterisation of the acoustic and cavitation field of a hand-held piezoelectric SW source is shown. PAM is used to determine the cavitation field by isolating the emissions from cavitation using the temporal distinction from the scattered source signal. In chapter 4, this concept is applied to SWL and cavitation is detected for ex vivo pig kidneys and model stones.

2 Tracking Stones using trilateration

The following chapter has been largely based on a published article [165]. It is motivated by the fact that during SWL many shock waves are delivered to the body that do not impact the stone, but do result in tissue trauma. Thus, a monitoring system is developed to locate kidney stones, with the goal of gating shock waves not aligned with the stone, and hence, reducing renal trauma during lithotripsy. The system consists of a circular array housing twenty-two 0.5 MHz transducers that can be mounted on a clinical lithotripter. It was deployed in a water tank and tested with two stone models made from gypsum cement and a stone model fragment. An algorithm consisting of: threshold detection, automatic rejection of weak signals, and triangulation was developed to determine the location of stones. The results show that within ±15 mm of the focus of the lithotripter, the accuracy was better than 4 mm in the lateral directions and 2 mm in the axial direction. Using off-the-shelf hardware, the algorithm can calculate stone positions every 1 s allowing for real-time tracking during lithotripsy.

2.1 Introduction

Stone motion, due to respiration and/or patient motion during the procedure, means that as few 40 % of the SWs delivered to the body hit their target due to misalignment of the SW focus and the kidney stone [25]. The mistargeted SWs will therefore

induce tissue damage without providing a therapeutic effect. Hence, it follows that if the stone can be tracked in real-time, the delivery of SWs can be gated to ensure that SWs are only fired when the stone is in the focus, which would result in fewer SWs being delivered to the patient.

Rather than using B-mode ultrasound, with typical frequencies in the range of 3 MHz to 7 MHz, a circular array of twenty-two 0.5 MHz transducers that can be mounted as a collar on a clinical lithotripter was employed. Using a lower frequency results in less attenuation of the signal as it propagates through several layers of tissue. The aim of this work is to localise kidney stones in real-time, in order to provide a trigger signal for a lithotripter when the stone is in the focal region. Each transducer, in turn, transmits a short, low-pressure pulse, and all the transducers record the backscatter from the stone. The arrival time of the echo on each recording is determined using threshold detection, and then a trilateration algorithm is used to determine the stone location. The elements are placed on the edge of the lithotripter aperture, to yield a larger aperture compared to B-mode. In this chapter, the accuracy of our system to locate targets is assessed and real-time performance of the algorithm is demonstrated.

2.2 Methods

2.2.1 Trilateration algorithm

Figure 2.1 shows the configuration of the system: an array of N transducers placed at locations $\vec{x}_k^{\mathrm{T}}$, where $\vec{x}$ refers to a three dimensional vector in space and k is an integer from 1 to N. Pulses are transmitted by transducer k, scatter off the stone located at $\vec{x}^{\mathrm{S}}$, and received by transducer m. The total distance travelled by sound

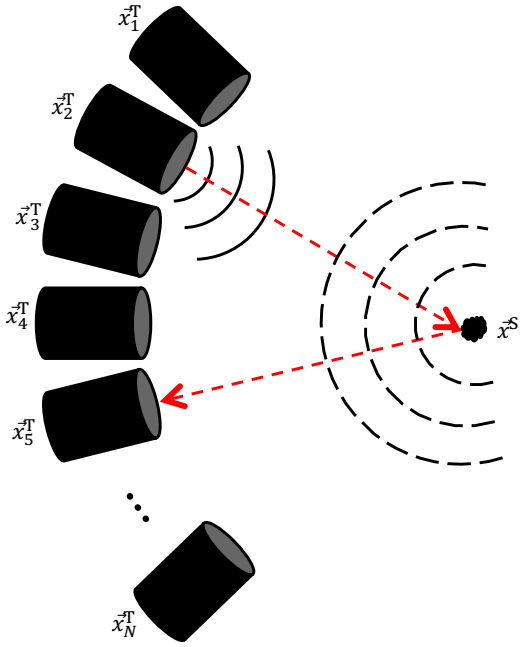


Figure 2.1: Schematic drawing of an array with N transducers and a scatterer illustrating the sound path between any two transducers.

for any combination of transducers is given by

$$x_{km} = \left|\vec{x}^{\mathrm{S}} - \vec{x}_k^{\mathrm{T}}\right| + \left|\vec{x}_m^{\mathrm{T}} - \vec{x}^{\mathrm{S}}\right|. \tag{2.1}$$

It follows that the echo time, t_{km}, in a medium of uniform sound speed, c_0, between transmitting by transducer k and reception by transducer m is

$$t_{km} = \frac{x_{km}}{c_0}. \tag{2.2}$$

By using multiple transducers, the location of the stone, $\vec{x}^{\mathrm{S}}$, can be determined algebraically using Eq. 2.2). In principle, three measured echo times are sufficient if the speed of sound in the medium and the locations of the transducers are known. In practice however, the echo time for each transmitter-receiver combination may differ from the ideal case due to a number of factors, including the irregular shape of the stone, a non-uniform speed of sound, noise in the signal, uncertainty in the

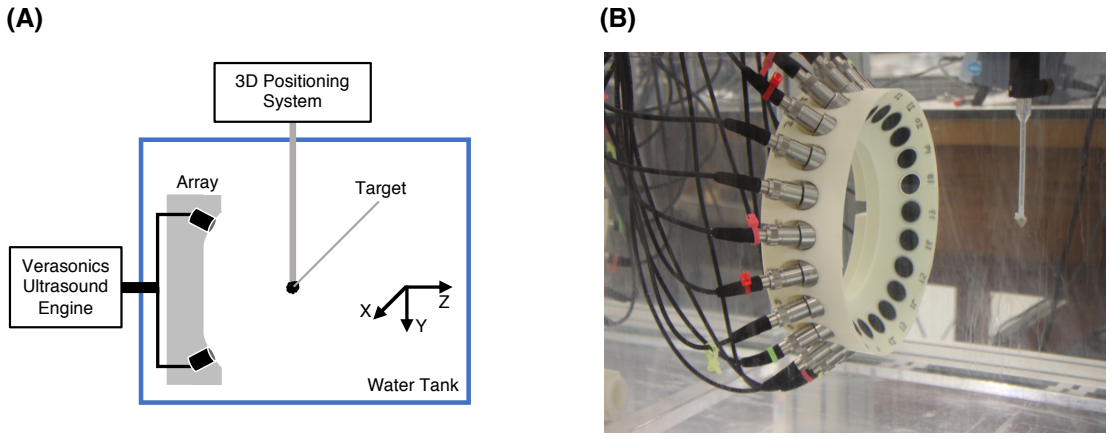


Figure 2.2: (A) Schematic drawing of the experimental setup. (B) Photograph of the system deployed in a water tank.

exact location of each element in the array, and the finite size of the transducers and the scatterer. Therefore, the approach here is to take many more measurements from which the following error function, e_{km}, is defined

$$e_{km} = |c_0 t_{km} - \hat{x}_{km}|, \tag{2.3}$$

where $\hat{x}_{km}$ is the estimated distance travelled by sound, and estimate the stone location by minimising the mean square error, $\bar{E}$, by varying $\vec{x}^{\mathrm{S}}$:

$$\bar{E} = \frac{1}{N^2} \sum_{m=1}^{N} \sum_{k=1}^{N} {e_{km}}^2. \tag{2.4}$$

2.2.2 Experimental setup

Figure 2.2 shows the experimental setup consisting of a circular array of transducers and a scatterer. Twenty-two transducers (0.5 MHz, 19.05 mm diameter, V318-SU Panametrics-NDT, Waltham, MA) were placed in a 3D printed collar on a circle of diameter 206 mm. The axis of each transducer was aligned to a point 128 mm away

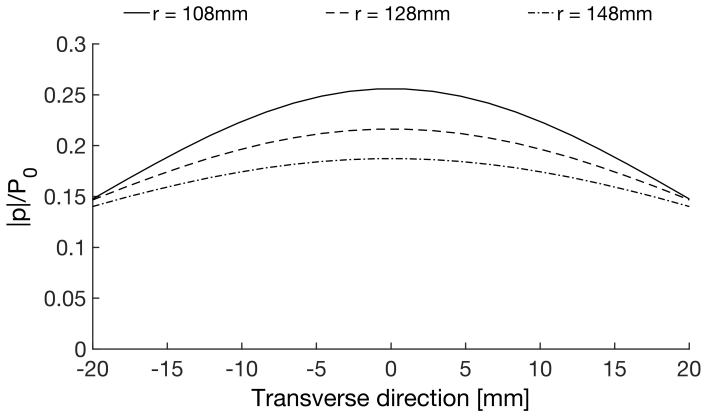


Figure 2.3: Lateral pressure field, p, normalised to the source pressure, P_0, of a 0.5 MHz transducer with an element diameter of 19.05 mm at three axial distances. The pressure field is uniform to ±30 % within ±20 mm of the focus.

in the z-direction; this corresponds to the focal length of a clinical lithotripter; the Dornier HM3 [166]. The Rayleigh distance for each transducer at 0.5 MHz is 95 mm, and therefore, the lithotripter focus, where the stone should be, is in the spherical spreading region of the transducers.

In figure 2.3, the normalised pressure field of the transducers for three axial depths ranging ±20 mm from the focus has been plotted. The beam directivity of the field that can be seen in the pressure profiles is a function of the directional factor, $D(\theta)$. It is defined as the pressure at an angle θ relative to the pressure on-axis, where $\theta = 0$, at the same radial distance from the transducer. For a vibrating piston the directional factor is

$$D(\theta) = \frac{2J_1(ka\sin\theta)}{ka\sin\theta}, \tag{2.5}$$

where the wavenumber $k = \omega/c_0$, a is the radius of the piston, and J_1 is the Bessel function of order 1 [145]. Figure 2.3 shows the radial pressure profile at the focus and at ±20 mm from the focus. It can be seen that the pressure field, normalised to the source pressure, is uniform to ±30 %, and thus, the amplitude of the scattered signal from a point scatterer within ±20 mm of the focus will be within 30 %. The beam directivity of the transducers limits the range for reliable localisations as will

be shown later.

A Verasonics Vantage ultrasound engine (Verasonics Inc, Kirkland, WA) was used to control the transmit-receive sequence, acquire the echo data, and compute the location of stones in real time. Each element was excited with a pulse of amplitude of 50 V and a frequency of 0.5 MHz for two cycles. The echo signal was received on all channels at a sampling rate of 2 MHz, four times the transmit frequency, and processed without filtering or time gain compensation.

The gypsum stones have properties similar to those of natural stones [167] and were cast in moulds of natural kidney stones created from micro CT data. Three scatterers were used: two stone models measuring approximately 10 mm by 5 mm by 5 mm cast from UltraCal 30 gypsum cement (United States Gypsum Co., Chicago, IL) and a stone model fragment. The scatterers were glued to the end of a plastic pipette, which was mounted onto a three dimensional positioning stage, so that the stone could be translated under computer control with an accuracy better than 0.1 mm. Subsequently, one of the two stones was fragmented using a lithotripter into a piece measuring 5 mm by 5 mm by 3 mm and the tracking experiment was then repeated.

2.2.3 Threshold detection

The measured echo time t_{km} was determined by doing threshold detection on the received signals. Cross-correlation and a combination of detecting the maximum amplitude within a specific time window were tried as an alternative method but were found to be less robust than threshold detection. Four representative raw receive voltage signals for a stone target are shown in figure 2.4. The theoretical arrival time for the cases shown in (A), (B) and (D) is 198 µs and for the case in (C) is 221 µs. It can be seen that the amplitude of the echo varies from 452 mV

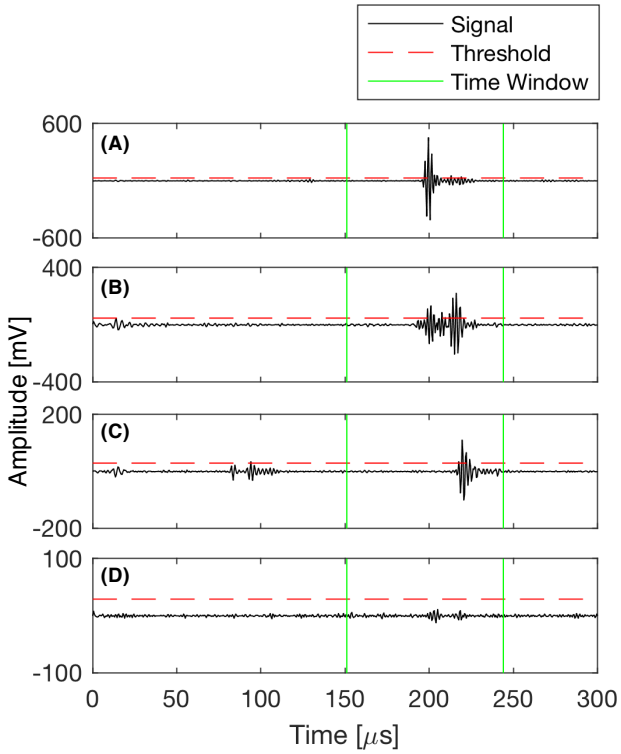


Figure 2.4: Representative receive signal traces highlighting the threshold detection for a stone target. The theoretical arrival time in (A), (B), and (D) is 198 µs and in (C) is 221 µs.

to 11 mV, and thus, an absolute threshold would not be appropriate. A study was conducted where the threshold was varied from 3 times to 30 times the standard deviation and it was found that a value of 15 gave the most robust detection. Based on this criteria, the threshold was approximately 30 mV in (A), (C) and (D), and 47 mV in (B).

In figure 2.4(A), an echo signal is detected at 197 µs, which compares well with the expected arrival of 198 µs, with reverberations within the stone resulting in about 20 µs of secondary signals. In figure 2.4(B), the echo is composed of multiple echoes of varying amplitude. As a result, the threshold employed here results in an arrival time of 193 µs; about 6 µs after the initial increase in the amplitude beyond noise, a little earlier than expected. Figure 2.4(C) shows an example, where the directly incident transmitted pulse is recorded on the receiver after 94 µs, while the echo from the stone is received at 217 µs. To avoid detecting the incident signal as an

echo, it was assumed that the target will not move beyond ±20 mm from the focus in any direction in which case the echo from the stone would only be received from 151 µs to 244 µs. Within ±20 mm of the focus, the directivity of the pressure field is uniform to ±30 %, and thus, the amplitude of the scattered signal should also be relatively uniform in that region. Figure 2.4(D) illustrates a situation where no scatterer could be identified by the threshold algorithm as the noise characterisation resulted in a threshold of 29 mV, which exceeded the 11 mV. amplitude of the echo. Decreasing the threshold to five times the standard deviation would have meant this particular signal was detected but would have lead to false detection elsewhere.

By using 22 transducers in the array, up to $22^2 = 484$ signals for each localisation are recorded. Therefore, even if individual stone echo signals do not produce a detectable signal, there should be sufficient redundancy to have a robust estimate of the stone location. An assessment of how many transducers are necessary for an accurate localisation will be presented later.

2.2.4 Error minimisation behaviour

The error function given in Eq. (2.4) was minimised with the MATLAB function *fminsearch*, which uses the simplex search method. [168] Figures 2.5(A) and 2.5(B) show the error as a function of iteration number and the estimated stone location for a stone placed at the focus. It can be seen that the mean square error steadily decreases and converges to a function output of 4.3×10^{-5} within 47 iterations (using an initial guess, $\vec{x}_0$, as the geometric focus). In space, the z coordinate and the radial distance monotonically approach asymptotic values and the final estimate for the position is within 1.3 mm of the true position.

Figures 2.5(C) and 2.5(D) show equivalent results for a stone 21.2 mm away from the initial guess. The search algorithm appears to settle around a local minimum

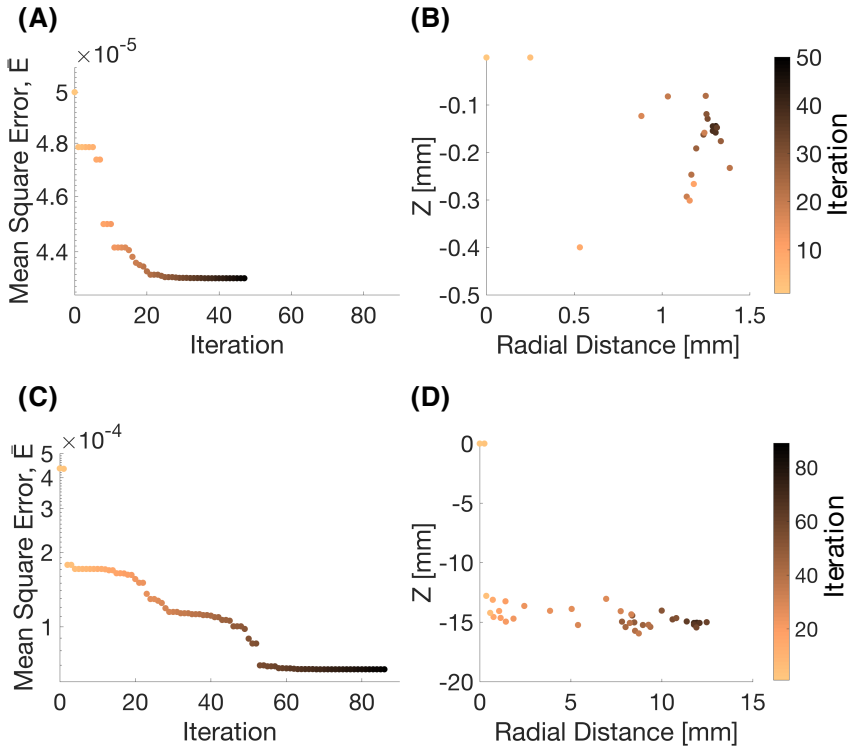


Figure 2.5: Minimisation algorithm: (A) and (B) stone placed at the focus $(0,0,0)$, where (A) shows the error function at each iteration and (B) shows the computed target location at each iteration with the final computed location $(-0.1,1.3,0.1)$. (C) and (D) stone placed 21 mm away from the focus $(0,15,-15)$, the final computed location $(0.4,11.9,-15.1)$.

for 20 iterations revealed by the flat portion of the error function. In the first few iterations, the z coordinate settles close to the true location $-15\,\text{mm}$, as shown in panel (D). Then the algorithm adjusts the radial distance with the final location reached after 86 iterations yielding an error value of 6.7×10^{-5}. This location is $0.4\,\text{mm}$, $3.1\,\text{mm}$, and $0.1\,\text{mm}$ away from the true location in x, y, and z, respectively.

The iterative minimisation algorithm was terminated, when the last steps of all coordinates of the estimated location were smaller than $0.1\,\text{mm}$ and the change in the mean square error was smaller than 10^{-10}. These values were chosen such that the algorithm does not get stuck in local minima and resulted in a computational time of $25\,\text{ms}$ on average for an $\vec{x}_0^{\,\text{S}}$ within $\pm10\,\text{mm}$ of the actual location.

It was found that varying $\vec{x}_0^{\,\text{S}}$ $\pm25\,\text{mm}$ away from the focus in any direction had a minor effect on the final estimate (less than $0.1\,\text{mm}$) but the computational time

was reduced when the initial guess was close to the actual location. Therefore, in the motion experiments, the initial guess was set to the previous location obtained.

Once the optimisation had been run, it was observed that some echo times, $t_{k,m}$, were significantly different from what would be expected from the initial result. Hence, prior to running the minimisation algorithm, the mean echo time and the standard deviation within the dataset were determined. Any echo times that were different by more than 1 standard deviation were excluded to avoid including echoes from structures other than the stone in the minimisation. The proportion of Excluded Echoes defined as

$$\text{Excluded Echoes } \% = \frac{\text{No. of echo times within 1 STD}}{\text{Total No. of signals}} \times 100\% \tag{2.6}$$

turned out to be a predictor of the accuracy of the localisation.

2.3 Results

2.3.1 Localisation accuracy

The accuracy of localising targets was determined by moving a stone in the focal region and comparing the true location to that estimated by the tracking algorithm. Figure 2.6 shows the RMS deviation in location in both lateral directions and along the axis of the lithotripter for two intact gypsum stones and one gypsum stone fragment for locations in a range up to 15 mm from the focus. The RMS deviation was used to measure the difference between estimated coordinates, $\hat{x}$, $\hat{y}$, and $\hat{z}$, and the true values x_t, y_t, and z_t:

$$\text{RMS dev.} = \sqrt{\frac{(x_t - \hat{x})^2 + (y_t - \hat{y})^2 + (z_t - \hat{z})^2}{3}}. \tag{2.7}$$

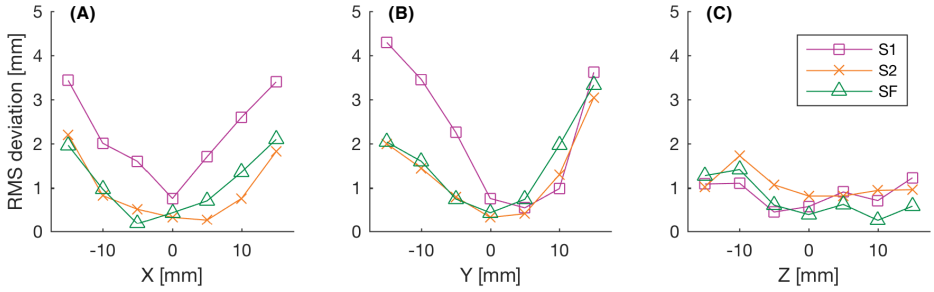


Figure 2.6: RMS deviation of the localisations for two stone models (S1,S2) and a stone fragment (SF) along the transverse directions (A and B) and the axial direction (C). In each of the cases the other variables are kept at the focal plane, i.e. for panel (A): $y = z = 0$.

Figures 2.6(A) and 2.6(B) show for lateral motion the deviation less than 2 mm for ranges up to 10 mm from the focus and in the axial direction the deviation was less than 2 mm for all ranges tested.

Figure 2.7 shows the accuracy in orthogonal two-dimensional planes for all three targets. In the lateral plane (upper images), it can be seen that the error within the square spanning ± 5 mm from the focus yields errors less than 3 mm. In the axial plane (lower images), the error is less than 2.5 mm for ranges of ± 15 mm in the axial direction and ± 5 mm in the lateral direction.

2.3.2 Uncertainty estimation

The data in Figures 2.6 and 2.7 show that as the target moves away from the focus the localisation accuracy reduces. Two metrics were studied to see if the localised accuracy could be determined from the echo data. One metric was the mean square error, $\bar{E}$, given in Eq. (2.4), which was hypothesised to be small when the accuracy was highest; the second was the number of echo signals within one standard deviation of the mean of the echo times in the dataset, defined as the Excluded Echoes in Eq. (2.6).

Figure 2.8(A) shows the mean square error, $\bar{E}$, as a function of the deviation for

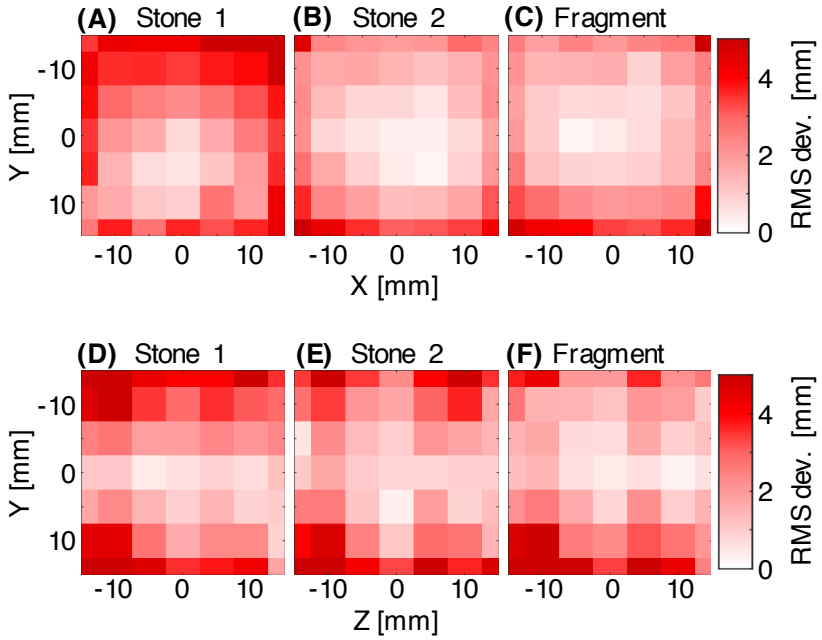


Figure 2.7: RMS deviation of the localisations for the three different targets (A)-(C) in the lateral and (D)-(F) axial planes.

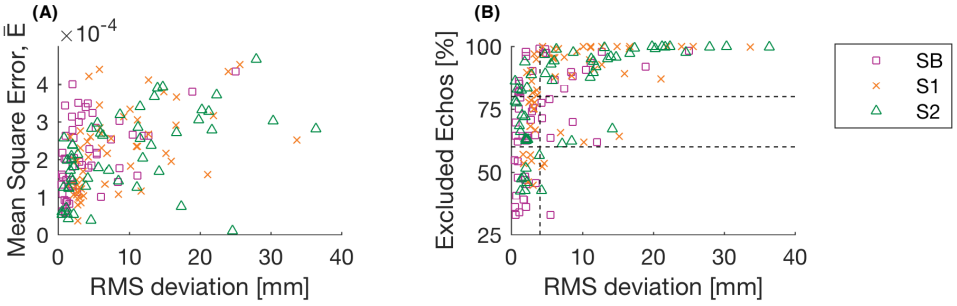


Figure 2.8: Comparing the mean square error (A) and the percentage of Excluded Echoes (B) to the true deviation to determine a metric for an uncertainty estimate.

targets placed ±30 mm from the focus and figure 2.8(B) shows the percentage of Excluded Echoes as a function of the RMS deviation. In figure 2.8(A), it can be seen that there is a poor correlation between the mean square error and the deviation. In figure 2.8(B) however, it can be seen that the Excluded Echoes resemble a receiver operator curve. With the exception of one point, localisations that were made with fewer than 60 % Excluded Echoes yield a deviation of less than 5 mm. With the exception of nine further points, any localisation that was computed with fewer than 80 % Excluded Echoes also results in less than 5 mm deviation. These nine points all stem from targets placed 20 mm to 30 mm away from the focus in the lateral direction, which is beyond the region of a uniform pressure field of the transducers. As the target is moved to a location where the beam directivity drops (>20 mm), the signal to noise ratio drops as well limiting the algorithm's ability to detect robust echoes. With fewer transducers detecting a reliable echo time, the accuracy of the localisation drops, thus creating the possibility to use the percentage of Excluded Echoes as a metric for the accuracy in the localisation.

Using the data in figure 2.8(B) a threshold can be defined to determine if a SW should be fired to break up stones detected to be in the focal zone or not. A threshold of 60 % Excluded Echoes yielded a 4.9 % false-positive rate (that is, deviation was >4 mm but not rejected) and a 34.9 % detect rate (that is, localisations of better than 4 mm was identified). By applying an Excluded Echoes percentage threshold of 80 % these rates will change to 19.5 % and 72.3 %, respectively.

2.3.3 Number of transducers

The collar was fabricated for 22 transducers, however it may be possible to achieve sufficient results with fewer transducers, which would reduce acquisition and processing times. The impact of using fewer transducers was accomplished by post-

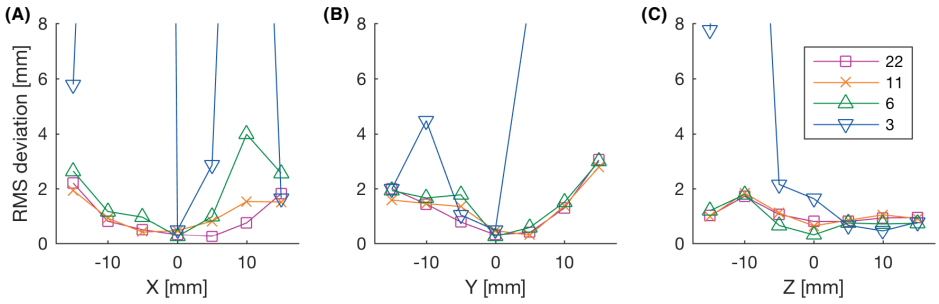


Figure 2.9: RMS deviation of the localisations for a stone model, using 3, 6, 11, or 22 transducers from the collar, in the transverse directions (A and B) and the axial direction (C).

processing full data sets and only using a subset of transducers. The transducers were chosen such that the aperture was not changed and such that active elements were always equally spaced. Figure 2.9 shows the error along all three directions for 3, 6, 11 and 22 transducers. It can be seen that 11 and 22 transducers result in an almost identical error profile. Using six transducers results in a similar profile for all but two off-axis locations. Finally, using three transducers the stone cannot be located reliably in the lateral directions nor on-axis. The accuracy is worse than 5 mm in two locations.

The processing time was 25 ms for 22 elements, 10 ms for 11 elements, 5.8 ms for 6 elements, and 4.3 ms for 3 elements.

2.3.4 Moving targets

Figure 2.10 shows the results of localising a stone that was in continuous motion (range ±10 mm) across the focus in the lateral direction using 22 elements. The colour coding of each localisation identifies the uncertainty (percentage of Excluded Echoes) in the localisation. The location is estimated accurately when the stone is within ±7.5 mm of the focus and the uncertainty is low. When the stone moves to ±10 mm, the localisation has an error of <7.5 mm, however, the uncertainty is also high, which means the information can still be used for gating. Note however, the

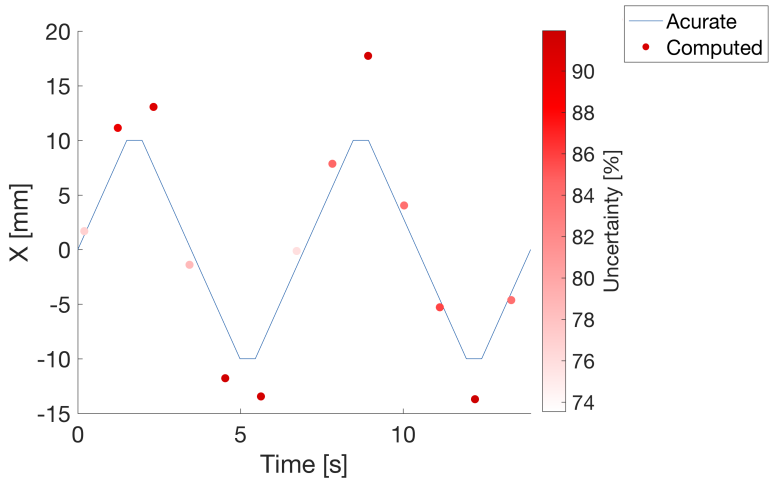


Figure 2.10: Localising a moving stone that is displaced ±10 mm from the focus and showing its true location as a line and the estimates as red points. The colourbar identifies the percentage of Excluded Echoes to predict the accuracy of each localisation.

previously identified Excluded Echoes threshold for stones (60 % to 80 %) is different in these data where even up to a value of 86 % Excluded Echoes the localisations are accurate.

2.4 Discussion

It has been shown that a trilateration approach, combined with a minimisation algorithm, can be used to localise kidney stones in vitro. The results reported here show (for three tested scatterers) that the accuracy is better than 3 mm for stones within ±10 mm of the focus in the lateral direction (with one exception). Localisations became significantly less accurate at lateral distances greater than ±10 mm from the focus, which was expected, given the beam width of the transducers. We note that the focal width of current lithotripters ranges from 2.8 mm to 7.7 mm [50], and therefore, correctly identifying whether the stone is in the focal volume within ±10 mm is sufficient to gate SWs for the application at hand.

A correlation between the accuracy of the localisation and the number of transducers

Table 2.1: Detection rates (DR, better than acceptable deviation and correctly identified) and false positive rates (FP, above acceptable deviation but not rejected) for 60 % and 80 % Excluded Echoes for different acceptable RMS deviations.

Excl. Echoes thresh.	**60 %**		**80%**	
Accepted RMS dev.	**DR**	**FP**	**DR**	**FP**
<2 mm	44%	13%	79%	36%
<4 mm	35%	4.9%	72%	20%
<8 mm	29%	0%	62%	12%

that pick up an echo time within 1 standard deviation of the mean echo time in that dataset, the percentage of Excluded Echoes as defined in Eq. (2.6), was determined. This metric was more robust as a predictor of uncertainty than the mean square error, $\bar{E}$. Analysing the current datasets suggests a threshold between 60 % and 80 % of Excluded Echoes can be used to determine if the stone localisation is accurate. For more complex media such as tissue, we anticipate that the variation in this threshold could be even greater. It may be that the threshold detection for an accurate localisation must be determined for each patient, a process that could be achieved by taking an initial measurement when the stone is in a known location. Fluoroscopy is typically used for alignment at the start of lithotripsy and an initial ultrasound measurement when the stone is in the focus could be used to estimate an appropriate threshold of Excluded Echoes for robust localisations.

Furthermore, lithotripters that differ in focal width might require different thresholds from 60 % or 80 % that were optimised for an acceptable deviation of <4 mm. Table 2.1 shows how the detection rates (DR) and the false positive rates (FP) change for acceptable RMS deviations (defined in Eq. (2.7)) of <2 mm, <4 mm, and <8 mm, and for 60 % and 80 % Excluded Echoes. Here, the compromise lies in not increasing treatment times while minimising the risk of missing the target. For lithotripters with larger focal widths (and thus a higher acceptable deviation), it might be appropriate to set a higher threshold to reduce treatment times. It can be seen that an acceptable deviation of <8 mm yields a FP of 12 % for 80 % Excluded

Echoes. This value is similar to the FP of 13 % for a deviation of <2 mm and 60 % Excluded Echoes. The higher DR at a higher Excluded Echoes threshold of 80 % would result in a faster treatment time and might thus be desirable. Lithotripters with narrower foci, however, require a lower threshold in order to decrease FP rates.

It was shown that decreasing the number of transducers reduces the acquisition time but also results in poorer performance. For three elements it was not possible to robustly locate the stone. It should be noted that in tissue, signals will be subject to a greater degree of non-ideal behaviour, and so, although it was sufficient in vitro, it would not be a surprise if all 22 (maybe even more) transducers would be needed in tissue. In vivo, the signals would be subject to attenuation, resulting in a poorer signal to noise ratio that might impact the algorithm's ability to detect an echo. Furthermore, multiple reflections from interfaces are expected to be registered. Given that the stone is initially located reliably using fluoroscopy, that a priori location information could be used to initially identify the echo from the stone reliably. That information may then be used to create robust echo detection parameters for each patient in the presence of multiple tissue layers.

Using a MATLAB code, it was possible to acquire and process data in approximately 1 s using 22 elements. Given lithotripter fire rates are on the order of 1 Hz to 2 Hz, this is not quite sufficient for real-time tracking. Implementing the algorithm in a complied code should reduce the time dramatically, it is noted that the acquisition time for recording 300 µs on 22 transducers is 6.6 ms, and so, if processing times can be reduced to less than 0.1 s, real-time stone tracking can be carried out. Furthermore, assuming that breathing causes the stone to move at a maximum speed of $5\,\mathrm{mm\,s^{-1}}$, it would take ∼0.5 s for the target to move across the width of a narrow lithotripter focus. In that case, the computational frequency requirement for a localisation would be at least 2 Hz.

The scope of the experiments reported here have two main limitations. First, all

experiments have been conducted in water, a homogeneous medium with low attenuation and known sound speed. In tissue, the signals would be subject to scattering and reflections from different tissue interfaces (e.g. fat and muscle), and the signals would be weaker due to higher absorption. In these complex structures, weighting different echo times based on the robustness of the echo, the amplitude of the signal, or the noise level might be advantageous. In the homogeneous environment, however, applying weights did not result in an improved accuracy. Second, for the current experiments only one scatterer has been placed in the acoustic field. During SWL however, stones will break into multiple fragments and multiple stone fragments will be present in the field. It would be necessary to show the system remains robust in the presence of multiple fragments.

2.5 Conclusions

In summary, it has been shown that for a low-element count array in a configuration appropriate for a lithotripter it is possible to track a model kidney stone with an accuracy better than 4 mm near the focus. This system could be used to gate SW delivery in order to reduce SWs that are not targeted on the stone. Furthermore, it would indicate if motion had moved the stone permanently out of the focus. The proposed system would not interfere with other imaging modalities such as X-ray fluroscopy or B-mode ultrasound. The approach measured echo times between multiple transducers using a threshold detection to determine the echo time. A minimisation approach was employed to determine the most likely position of the stone. An uncertainty parameter has been identified that can be used to exclude inaccurate results. Finally, the method can be used to track moving targets in real time. Accessing the robustness of the method in more realistic complex tissue structures is now necessary.

3 Characterisation of the EMS PiezoClast

The acoustic field and the cavitation dynamics of the clinical shock wave therapy source, the EMS PiezoClast, were characterised using a PVDF needle hydrophone. The focal waveform was measured with a peak acoustic pressure of 25.9 MPa and a focal region of 1.8 mm by 8.0 mm at the highest energy setting and the peak pressure of 5.9 MPa and a focal region of 2.6 mm by 11.2 mm at the lowest setting. Passive acoustic mapping was used to study the cavitation dynamics, showing bubble growth, collapse, and rebound due to the shock waves. The characteristic and rebound times depended on the energy level and the pulse repetition frequency of the shock wave. From energy level 1 to 20 the characteristic time grew from 43 µs to 218 µs and the rebound time grew from 40 µs to 106 µs for shocks fired at 1 Hz. At higher levels the characteristic and rebound times increased with the pulse repetition frequency and reached 288 µs and 211 µs, respectively at energy level 20 and 8 Hz. The results suggest that passive acoustic mapping can be a viable monitoring technique or research tool implemented during shock wave therapy.

3.1 Introduction

In this chapter, the pressure and cavitation fields from a hand-held piezoelectric shock wave source, the EMS PiezoClast, are characterised. The source uses 1000 piezoelectric crystals that are arranged in a spherical cap. A gel pad that varies in size, such that the focus can be between 5 mm and 40 mm in the body, is used to couple the source to the patient. The manufacturer reports a pressure range from 11.5 MPa to 82.2 MPa and a positive ED of up to 0.42 $\mathrm{mJ\,mm^{-2}}$ at the focus of this device. Although the acoustic fields for some SWT devices have been reported [71,73,169–171], many clinical SWT studies do not report acoustical parameters. As a result analysing the efficacy of SWT and defining an effective SWT dose becomes challenging.

Passive acoustic mapping (PAM) was used to characterise the cavitation field. PAM uses an array of passive detectors, commonly a conventional B-mode ultrasound probe, to listen to acoustic emissions as a result of the interaction of another ultrasound source, e.g. therapeutic ultrasound, with the medium [131]. The passively recorded signals are beamformed to create a map of the source energy associated with the emissions. PAM is a technique that has previously been used to monitor cavitation during high intensity focused ultrasound (HIFU) treatment in real-time [131]. The technique was originally demonstrated in both, a gel phantom and an ex vivo bovine liver [172]. It has also been used to monitor ablation [134], to estimate the temperature rise in tissue [135], and in drug delivery applications [136, 137].

The acoustic signature from cavitation produced by HIFU differs from that produced by SWs [119]. In HIFU, the emissions consist of a narrowband harmonic component, associated with the driving frequency of the therapeutic source, and a broadband component, uniquely associated with inertial cavitation [173]. In SWL or SWT bubbles grow to ∼1 mm with a timescale on the order of 100 µs before collapsing

violently [127]. The cavitation produces distinct emissions that typically occur at initial growth, violent collapse, and rebound [122, 129, 174]. The time between the initial growth and the violent collapse is referred to as the characteristic time, t_C, and the time between the violent collapse and the rebound is referred to as the rebound time, t_R [128]. A confocally aligned dual passive acoustic detection system has previously been used to localise bubbles during lithotripsy in vitro [128] and in vivo [123].

The cavitation dynamics have been defined for water and for nanocups, a polymeric nanoparticle with a single cavity [137]. It has been suggested that such particles stabilise a bubble in their cavity and that the bubble will cavitate inertially in a HIFU field, when the negative pressure threshold is overcome. For a cavity size of less than ∼600 nm, the cavitation threshold of the nanocup will depend on the driving frequency and the size of the initial bubble, and thus, on the particle size [175].

Nanocups have previously been used as cavitation nuclei that can be propelled through the leaky vasculature of tumours [137]. These particles have previously been used for transdermal drug delivery [176] and the delivery of oncolytic vaccinia viruses [177]. The goal of this chapter is to characterise the EMS PiezoClast by determining its acoustic field using a hydrophone and its cavitation dynamics in space using PAM.

3.2 Methods

3.2.1 Acoustic field

The acoustic field of a SW device, the EMS PiezoClast (Electro Medical Systems S.A., Nyon, Switzerland), was determined first. Although the source has been used

for SWT, detailed measurements of the acoustic field are not available, hindering the development of standardised and optimised therapy concepts.

The source employs a piezoelectric source (aperture diameter of 100 mm) mounted in a hand piece, connected to a control unit, which can be operated by setting an energy level (EL) between 1 and 20 and a pulse repetition frequency (PRF) of 1 Hz to 8 Hz. The source has a fixed focus of 63 mm and can be coupled to gel pads to provide a standoff of 5 mm to 40 mm.

The source was coupled to a 10 mm gel pad, using ultrasound gel, and mounted above a tank filled with de-gassed, de-ionised water, with the face of the pad immersed in the water, as shown in figure 3.1. An acoustic absorber was placed at a 30° angle at a distance of 27.5 cm from the source. A bare wire was attached to the back of the hand piece in order to detect the electromagnetic pulse that occurs when the source is fired. The cable was connected to an oscilloscope and used as a trigger signal for the experiments.

A polyvinylidene fluoride (PVDF) needle hydrophone (Müller-Plate Needle Probe, Müller Instruments, Oberursel, Germany) with a sensitive diameter of <0.5 mm was placed in the water tank underneath the source to measure the acoustic field. The hydrophone can measure pressures ranging from −10 MPa to 150 MPa and is capable of detecting a rise time of 50 ns according to manufacturer. It was connected to a computerised 3D positioning stage and connected to an oscilloscope (Waverunner 44Xi, Teledyne LeCroy, Chestnut Ridge, NY). The voltage was converted to the acoustic pressure using the manufacturer calibration of 12.5 mV MPa^{-1} that varies by ±3 dB from 0.3 MHz to 11 MHz. It was moved until the largest signal was measured and this was defined as the position of the focus. Pressure-time waveforms were recorded at the focus for all ELs. 2D scans in the X-Y and X-Z planes were performed for ELs 1, 10, and 20, where the signal was recorded within ±4 mm from the focus in the transverse plane and from a distance of 55 mm to 75 mm away from

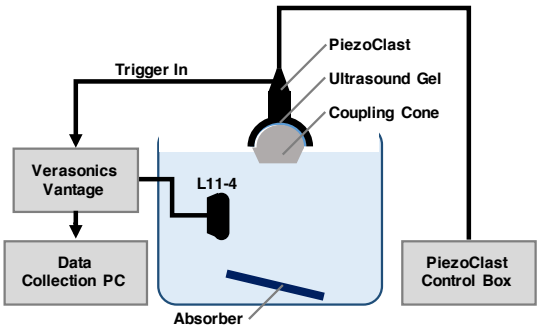


Figure 3.1: Experimental setup showing an ultrasound array, the L11-4, used to detect cavitation from a SWT source, the EMS PiezoClast.

the source in the axial direction.

3.2.2 Cavitation detection

Cavitation is one of the mechanisms by which SWT devices may produce a therapeutic effect. Yet, no measurements of the cavitation field of SWT sources, or specifically the EMS PiezoClast, are available. Developing PAM to detect cavitation during SWT could be utilised later for monitoring or research purposes. The following experiments outline how PAM has to be modified to detect cavitation that is not distinct in frequency (as would be the case in HIFU) but distinct in time (as is the case in SWT and SWL). The algorithms are subsequently tested in a water tank.

PAM data was acquired using a 128 element linear array, the L11-4 (Verasonics Inc., Kirkland, WA), which was oriented perpendicular to the acoustic beam of the SW as shown in figure 3.1. The probe has a $-6\,\mathrm{dB}$ bandwidth from $4\,\mathrm{MHz}$ to $11\,\mathrm{MHz}$ and was connected to a Verasonics Vantage ultrasound engine, which was interfaced with a PC. The Verasonics was triggered from the SW source at each SW and the PC was programmed through Matlab to collect the received RF line of each element in the L11-4 array for $1\,\mathrm{ms}$.

In order to align the L11-4 with the SW source, the hydrophone was placed in the tank and moved to the focus using the motorised positioning stage. The L11-4 was then moved using a manual positioning stage until the tip of the hydrophone appeared in the centre of the B-mode image. The hydrophone was then removed from the tank.

The acoustic emissions were recorded from 100 consecutive SWs for each setting of the source. The system was then left to rest for 1 min for all bubbles to disperse before the next experiment was conducted. The data sets were then post-processed in order to generate the energy maps.

Although the focus of this work was the characterisation in pure water, a final experiment using nanocups as cavitation nuclei was also performed. Given that these particles have previously been used in drug delivery applications using HIFU, their activation with a SW source could create an opportunity for future applications using nanocups and SW sources.

The cavitation dynamics due to nanocups were determined by flowing nanocups through a thin-walled, flexible, rubber tube (internal diameter 0.33 mm), which was placed at the focus of the SW source, as shown in figure 3.2. The tube was fixed onto a holder and mounted on a positioning stage. Initially, it was filled with air such that the reflection could be seen on the B-mode image created by the L11-4 and the tube could be aligned with the focus of the source. The nanocups were fabricated according to the formulation in [137] with a mean diameter of 487.3 nm and the polydispersity index of <0.1 determined with dynamic light scattering. The particles were diluted to a concentration of $1\,\mathrm{mg\,mL^{-1}}$ in degassed water. A syringe pump was used to flow the solution at a flow rate of $0.2\,\mathrm{mL\,min^{-1}}$ or a flow velocity of $9.7\,\mathrm{mm\,s^{-1}}$. Similar to the previous experiments, the effect of the EL and the PRF was tested by varying the EL from 1 to 20 and the PRF from 1 Hz to 8 Hz. As a control experiment, degassed, deionised water was flowed through the tube and

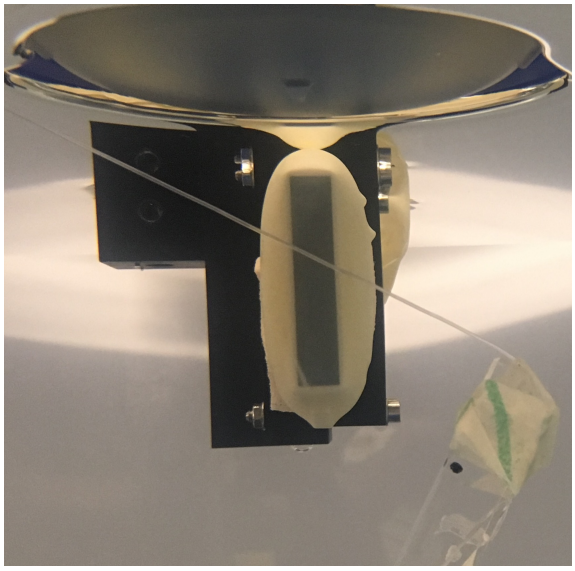


Figure 3.2: Photograph of the experimental setup to monitor the cavitation dynamics of nanocups. The EMS PiezoClast can be seen at the top of the picture with the tube running diagonally from the top left to the top right and the L11-4 placed perpendicular to the source.

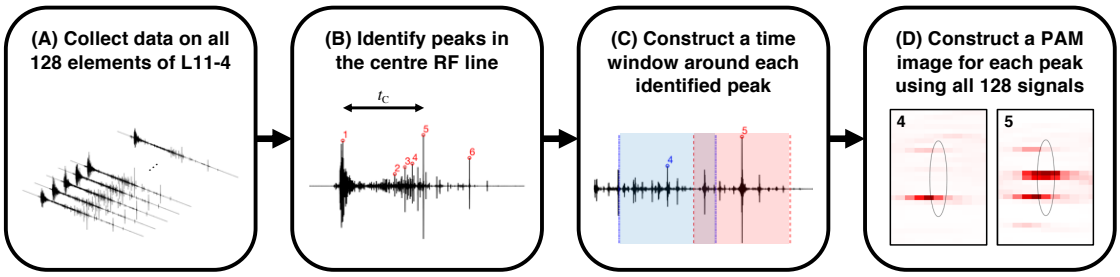


Figure 3.3: Schematic of the signal processing steps to characterise cavitation spatio-temporally due to a SW. The characteristic time, t_C shown in (B) refers to an event detected at peak 5. The shaded areas in (C) represent the time windows created around peaks 4 and 5.

the experiments were repeated.

Figure 3.3 shows a schematic representation of the post-processing steps. For each SW, the received emissions on all 128 elements of the L11-4 were collected and filtered using a finite impulse response equiripple bandpass filter from 4 MHz to 11 MHz. The central RF line (that is, the 64th element) was then used to identify peaks using the Matlab function *findpeaks*, as potential cavitation events. Peaks were defined as local maxima with an amplitude of at least $\frac{1}{5}$ of the maximum within the signal, $V_{\max}$, and at least 20 µs apart from each other. These values were determined empirically by testing $\frac{1}{10}V_{\max}$, $\frac{1}{5}V_{\max}$, and $\frac{1}{2}V_{\max}$ and 10 µs, 20 µs, 50 µs, and 100 µs,

respectively, to detect a reasonable number of peaks in each signal and limit the processing time. After detecting peaks, a time window of ±20 µs was constructed around each peak. Then all 128 signals were time windowed accordingly and the time segments were used to generate one map per peak using PAM. Using a larger time window resulted in too many events captured in one map. In this work, the Robust Capon Beamformer (RCB) was used to generate the maps [141], however, the same methods could also be applied to other beamformers. By processing the datasets as shown in figure 3.3, each cavitation event is defined by its t_C and in space.

The processing time for each SW depends on the number of peaks detected in each signal. The major contributing factors were the time it takes to filter the received signals on all 128 elements and the time to construct a map, which were approximately 2 s and 450 ms, respectively. Hence, in the example shown in figure 3.3 with six peaks and thus six maps, the total processing time was approximately 5 s.

3.3 Results

3.3.1 Focal Pressure

Figure 3.4 shows representative pressure waves recorded at the focus for three EL settings. The peak positive pressure, p^+, was 5.9 MPa at EL 1 and 25.9 MPa at EL 20. The rise time, defined as the time for the pressure to rise from 10 % to 90 % of p^+, was 272 ns at EL 1 and decreased to 185 ns at EL 20, which is consistent with non-linear steeping. The compressive part of the pressure (that is, the time from the initial SW rise to the first zero-crossing) lasts for about 1 µs for all ELs. After the leading positive peak there is a dip and then a shoulder (between 43.5 µs and

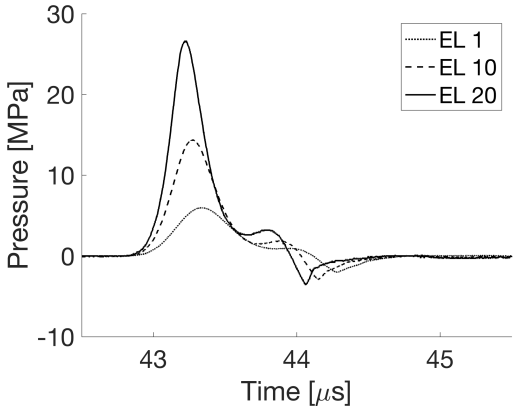


Figure 3.4: Pressure waveforms of the SW source at the focus for the nominal EL settings 1, 10, and 20.

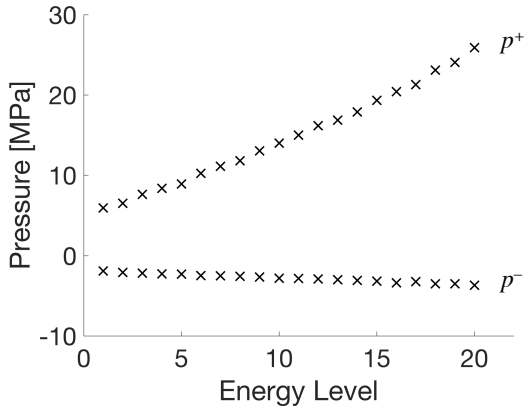


Figure 3.5: Peak positive, p^+, and peak negative, p^-, pressures of the SW source at the focus in water for all ELs. (Error bars not shown as $<1\,\%$.)

44 µs), which varies with the EL. In the case of EL 20, it results in a small second peak. The shoulder is followed by a short negative tail, which is EL dependent. The measurement of p^- might be limited by a bubble growing on the tip of the needle hydrophone and truncating the recorded pressure waveform. At EL 20 it has a sharp peak at 44.1 µs and then relaxes to the baseline. For lower settings the peak occurs later in time and is lower in amplitude. Figure 3.5 shows the peak focal pressures as a function of EL. From EL 1 to 20, p^+ increases from 5.9 MPa to 25.9 MPa and the peak negative pressure, p^-, from -1.9 MPa to -3.7 MPa, respectively. The relative increase in p^- is less than p^+ since at EL 1 p^- is 32 % of the p^+, while at EL 20 it is 14 %.

Table 3.1: The peak positive pressures (p^+), the peak negative pressures (p^-), the rise times of pressure wave (t_r), the positive energy densities (ED_+), and the length (F_L) and width (F_W) of the contour, where the pressure is −6 dB of p^+, for five nominal energy levels (EL) of the PiezoClast at the focus.

EL	p^+ [MPa]	p^- [MPa]	t_r [ns]	ED_+ [mJ mm^{-2}]	F_W [mm] × F_L [mm]
1	5.9	−1.9	272	0.01	2.6 × 11.2
5	8.9	−2.3	251	0.02	2.2 × 10.4
10	14.0	−2.8	236	0.04	2.2 × 9.4
15	19.3	−3.2	211	0.06	1.8 × 8.8
20	25.9	−3.7	185	0.10	1.8 × 8.0

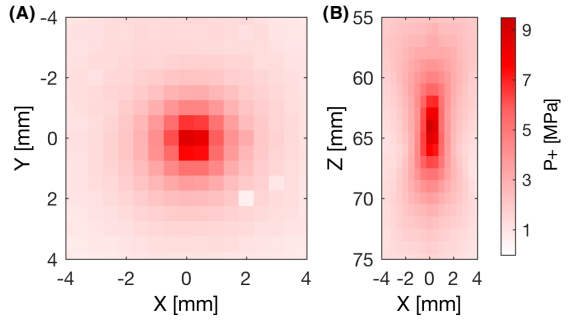


Figure 3.6: The peak positive pressure in the (A) transverse and (B) axial plane of the EMS PiezoClast at EL 5.

A commonly used metric in SWT is the energy density, ED. ED is defined by the IEC standard [178] as the pulse intensity integral, i.e. the time integral of the instantaneous intensity

$$\mathrm{ED} = \int \frac{p_\mathrm{a}^2}{Z_0}\, dt, \tag{3.1}$$

where p_a is the acoustic pressure and Z_0 is the acoustic impedance of the medium, water in this case. Because the hydrophone does not accurately capture the negative pressure, only the ED over the compressive phase, ED_+, was calculated by carrying out the integration in Eq. 3.1 up to the first zero-crossing. As shown in table 3.1, the ED_+ increases from 0.01 mJ mm^{-2} to 0.1 mJ mm^{-2} from EL 1 to 20. The increase is predominately due to higher peak positive pressures as the duration of the compressive part of the wave does not change significantly with the EL.

Figure 3.6 shows 2D scans of p^+ of the SW source in the transverse and axial planes at EL 5. The focal volume of the source can be determined from the −6 dB (−50 %)

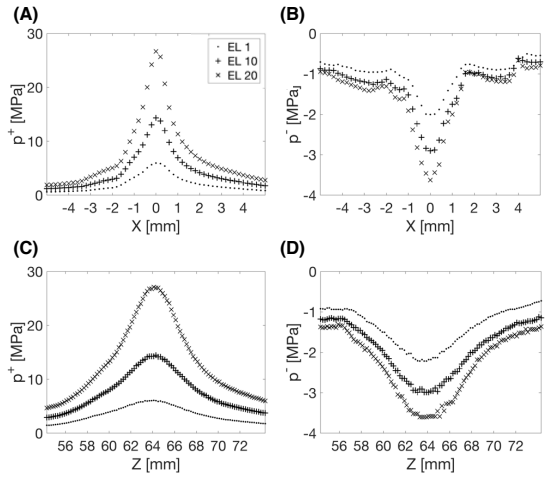


Figure 3.7: Linear scans at three different ELs showing the (A/C) peak positive and (B/D) peak negative pressures in the (A/B) axial and (C/D) transverse direction.

contours. The peak pressure of 9.1 MPa occurs at an axial distance of 64 mm at EL 5, and the focal region is 10.4 mm in length by 2.2 mm in diameter. The −6 dB region is symmetrical in the transverse direction and cigar shaped in the axial plane. Table 3.1 shows the size of the focal region for a range of ELs. It can be seen that the dimensions of the focal region shrank by ∼30 % as the EL increases from 1 to 20.

One dimensional scans in the X- and Z-direction are shown in figure 3.7 for EL 1, 10, and 20. The scans show that the distributions do not change dramatically with EL. There is a slight asymmetry in the X-axis, particularly for p^-. Figure 3.7(B) shows p^- in the transverse transverse direction, where p^- exhibits a local maximum at ±2 mm. In contrast p^+ decreases monotonically with distance from the focus.

Figure 3.8 shows the pressure waveform at EL 20 at ±1 mm and ±2 mm away from the focus in the transverse direction. These waveforms demonstrate that both, the amplitude of the wave drops (25.9 MPa at the focus, 11.9 MPa at 1 mm, and 6.7 MPa at 2 mm) and the shape of the wave changes: the duration of the compressive parts increase from 1 µs at the focus to 1.5 µs and 2 µs for 1 mm and 2 mm, respectively, and at 2 mm the negative pressure is almost completely vanished.

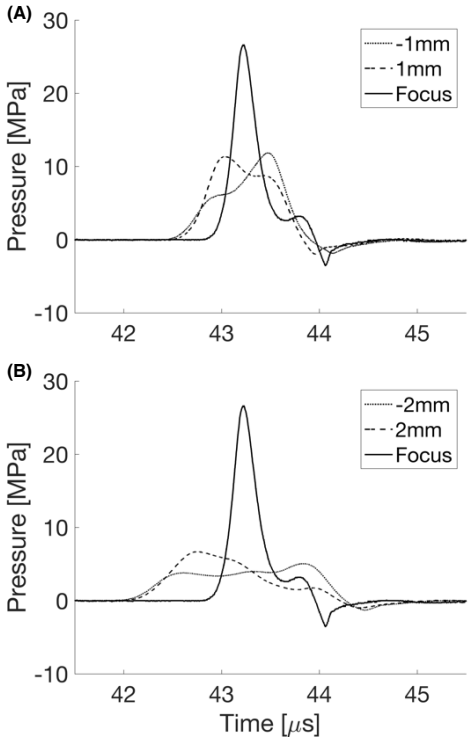


Figure 3.8: Pressure waveforms at a distance of (A) 1 mm and (B) 2 mm from the focus in the positive and negative transverse directions for EL 20.

In figure 3.8(A), an asymmetry can be seen in the waveforms, when at 1 mm, a positive peak is followed by a shoulder but at −1 mm the shoulder is followed by the peak. The same trend can be seen at a distance of ±2 mm in figure 3.8(B). This behaviour suggests an asymmetry of the source and that one side of the source might produce a pressure wave that is higher in amplitude than the other side.

3.3.2 Cavitation detection

Figure 3.9 shows representative receive signals from the centre element of the diagnostic array, peaks identified in these signals, and the PAM images associated with each peak to localise cavitation and to determine the cavitation dynamics at three different ELs. The Z-axis is along the SW wave propagation with the source at $z = 0$. The theoretical resolution of PAM is ∼0.4 mm in the Z-axis (transverse to

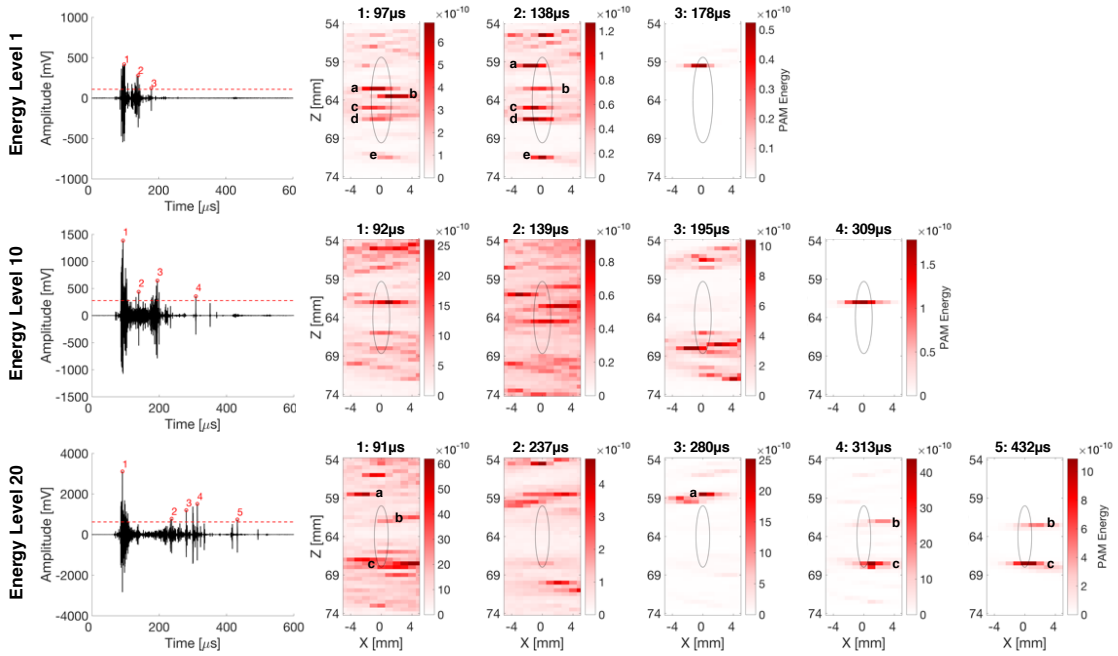


Figure 3.9: Cavitation detection during SWT at three ELs for an experiment in pure water. The three rows show representative results for a single SW at EL 1, 10, and 20. The left column shows the centre RF line received on the L11-4 array and the peaks detected in that signal. The following columns show the PAM images corresponding to each of those peaks. The oval represents the −6 dB contour of the pressure field with the SW coming from the top.

array), which is better than ∼4.8 mm in the X-axis.

At EL 1, the incident signal occurs at 97 µs, which corresponds to the travel time from the SW source to its focus and to the diagnostic array. This initial arrival can be attributed to scattered signals from the focal volume and emissions from the initial growth of bubbles, and has a duration of 30 µs. The signal at peak 2 at 138 µs constitutes the main collapse of the bubbles yielding a t_C of 41 µs. Peaks 1 and 2 constitute the double-bang that has been previously observed in lithotripsy. The PAM, constructed around peaks 1 and 2, each show four distinct locations of activity in the focal region. Locations 1c and 1d map to 2c and 2d suggesting growth and collapses of bubbles in these locations. 1a and 1b map to 2b suggesting that they translate towards each other and perhaps coalesced. The collapse at 2a should be related to a small signal in 1 outside the focal region. Similarly, 2e has a precursor at 1e. Finally, at peak 3, one location of collapse is identified, which appears to

correspond to a rebound of the signal at 2a with a rebound time, $t_R = 40\,\mu s$.

At EL 10, the number of total peaks detected, in the representative case shown in figure 3.9, increases to four. The structure of the receive signal is similar to before, with the incident emission at 1, the main collapses at 3 and 4, and a potential rebound at 340 µs that falls under the detection threshold. In this case there is an additional peak at 2, which occurs in the 'noise" between the incident signal and the first collapse. The amplitude of the RF trace for peak 1 is larger than at EL 1, and the maximum source energy is 25×10^{-10}, about four times larger. There are three peak locations in the focal region of the map and also more pre-focal signals, which are diffusive. Peak 2 occurs within a period of elevated noise between the detection of the incident sound and what appears to be the time that the majority of bubbles collapse. Peak 3, at 195 µs, constitute a characteristic time that is later than at EL 1. Finally, the last peak is detected at 309 µs and results in a PAM with one major collapse in the focal region with a t_C of 217 µs. The location of the collapse coincides with the region of activity detected in peak 1 indicating the initial growth of the bubble, however no rebound was detected in this case.

At EL 20, five peaks are detected, the first (at 91 µs) corresponds to the incident wave. Peak 2 occurs in the noise signal and results in a map that has little correlation with the other ones. Peaks 3 and 4 are somewhat clustered from 237 µs to 313 µs suggesting the main collapse is not synchronous as at lower ELs. The features at 1a and 3a could correspond to the growth and collapse of a bubble proximal to the focus with a characteristic time, $t_C = 189\,\mu s$. The features b and c in the 1^{st}, 4^{th} and 5^{th} map show the main cavitation activity with a t_C of 222 µs and a t_R of 119 µs, where b occurs off axis and c distal to the focus.

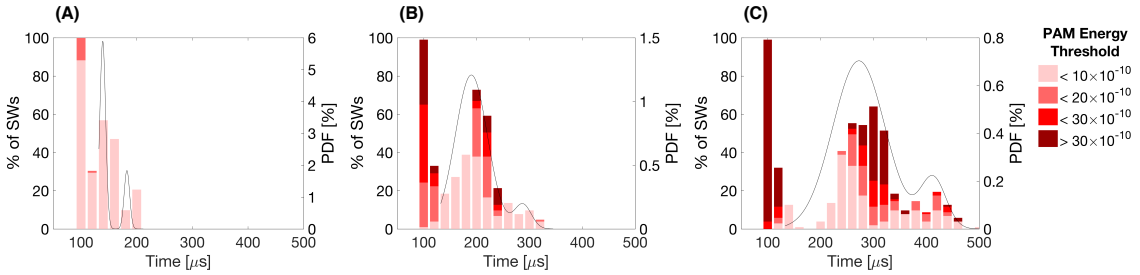


Figure 3.10: Histogram of time distribution of peaks detected at (A) EL 1, (B) EL 10, and (B) EL 20 after delivering 100 SWs at each EL. The maximum energy in the PAM resulting from each peak is shown in the colourbar. A bimodal Gaussian probability density function (PDF) is fit to each curve, for t >125 µs, and shown in the right y-axis.

3.3.3 Cavitation dynamics

To reduce the data that was collected over 100 SWs at each EL, histograms of the temporal peak distribution were generated, where the height of the bars shows the number of events recorded and the colour intensity indicates the PAM energy, figure 3.10. It can be seen that at all ELs the arrival of the SW at 95 µs is detected >98 % of the time. The signals from the main collapse and the rebound can be seen as a double-humped distribution in the histograms, and the timings of the two distinct peaks, relative to the detection of the incident SW, increases. However, the number of peaks detected as rebounds is smaller than those detected as the main collapses, that is, the second peak is smaller than the first. The colour of the bar is related to the acoustic energy emitted from the collapses. It can be seen that the energy increases with the EL, as at EL 1, none of the peaks resulted in a PAM with a maximum energy $> 10 \times 10^{-10}$ while at EL 20 most of the emissions resulted in a PAM energy exceeding 30×10^{-10}. The longer characteristic times and higher emission energies are consistent with bubbles growing larger and collapsing more violently at higher ELs.

To capture the collapse-rebound times, a bimodal Gaussian probability density function (PDF) was fit to the data after the first peak, i.e. for the data after 125 µs, where

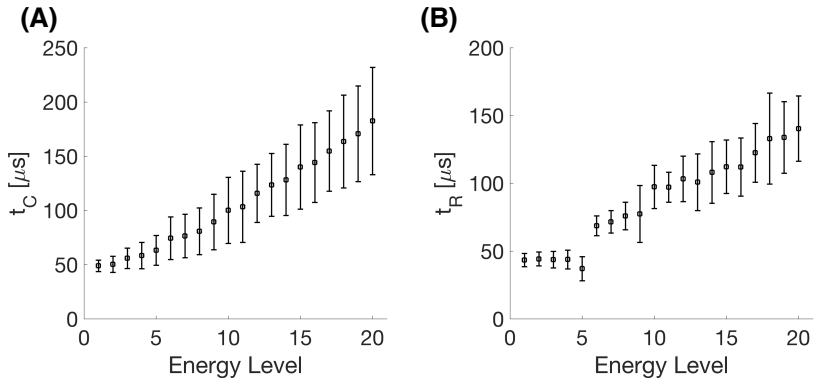


Figure 3.11: Mean characteristics of the main collapse at the characteristic time, t_c, and the rebound time, $t_r = \mu_2 - \mu_1$, when delivering 100 SWs at each EL in pure water.

bimodal PDF is

$$\text{PDF} = m \times \mathcal{N}(\mu_1, \sigma_1^2) + (1-m) \times \mathcal{N}(\mu_2, \sigma_2^2) \tag{3.2}$$

where μ_1, μ_2, σ_1, and σ_2 are the means and standard deviations of the first and second mode of the PDF, and m is the weighting factor between the modes. The parameters were used to fit the model to the datasets using MATLAB's *maximum likelihood estimates* function. The PDFs for EL 1, 10, and 20 are shown in figure 3.10. From μ_1 and μ_2 the mean t_C and t_R were determined and figure 3.11 shows how the means and the standard deviations vary with the EL. Figure 3.11(A) shows t_C increases with the EL and the standard deviation also increases, both in an absolute sense and a relative sense, which suggests that the characteristic time at higher ELs spreads across a large time span and that more peaks are detected. Figure 3.11(B) shows that t_R also increases above a threshold level of EL 5. This suggests either the absence of a rebound or that it was not detected, for ELs 1 through 5.

Figure 3.12 shows how t_C and t_R are affected by the PRF at four different ELs. It can be seen that at EL 5, t_C changes from 63 µs to 53 µs and t_R from 37 µs to 48 µs, when the PRF changes from 1 Hz to 8 Hz. At EL 10, t_C remains constant until 6 Hz, when it increases from ∼90 µs to 149 µs. The rebound time, t_R decreases from 1 Hz to 4 Hz, is absent at 6 Hz, and increases to 139 µs at 8 Hz. At EL 15 and EL 20, t_C

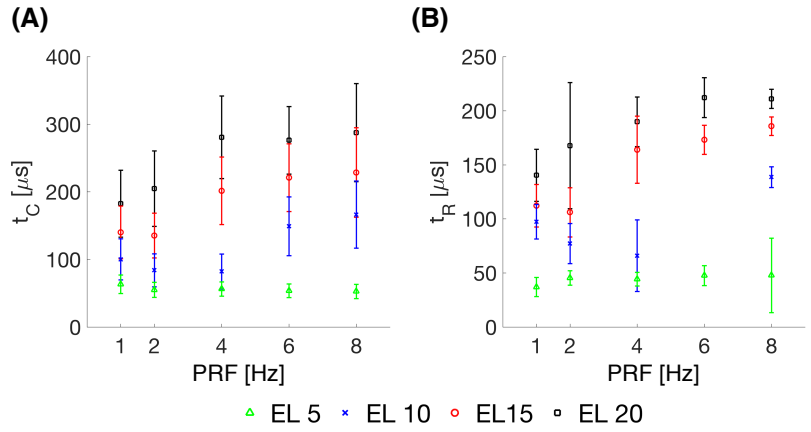


Figure 3.12: The effect of the pulse repetition frequency (PRF) on the characteristic and the rebound time for ELs 5, 10, 15, and 20. The means and standard deviations were determined by delivering 100 SWs in pure water.

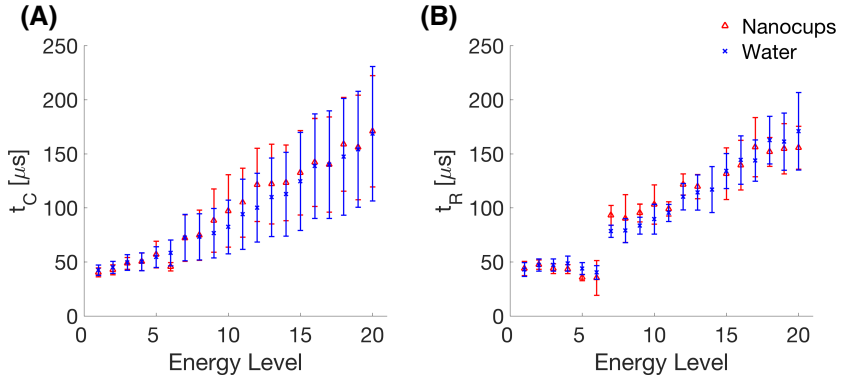


Figure 3.13: Cavitation dynamics of nanocups and water flowing through a tube. The mean and standard deviation of the characteristic time, t_C, and rebound time, t_R, of the cavitation is shown as a function of the energy level of the source.

is constant at 1 Hz (∼140 µs) and 2 Hz (∼200 µs) before increasing at 4 Hz to 201 µs for EL 15 and 281 µs for EL 20, and remaining at a similar level for 6 Hz and 8 Hz. Similarly, t_R increase with the PRF and at 8 Hz reach a value of 164 µs at EL 15 and 211 µs at EL 20.

3.3.4 Cavitation dynamics of nanocups

Figure 3.13 shows t_C and t_R of nanocups and water that was flowed through a tube at the focus of the SW source at all ELs of the PiezoClast. From EL 1 to 8, the t_C of the cups appears to match the control (figure 3.13A). The data looks similar to the

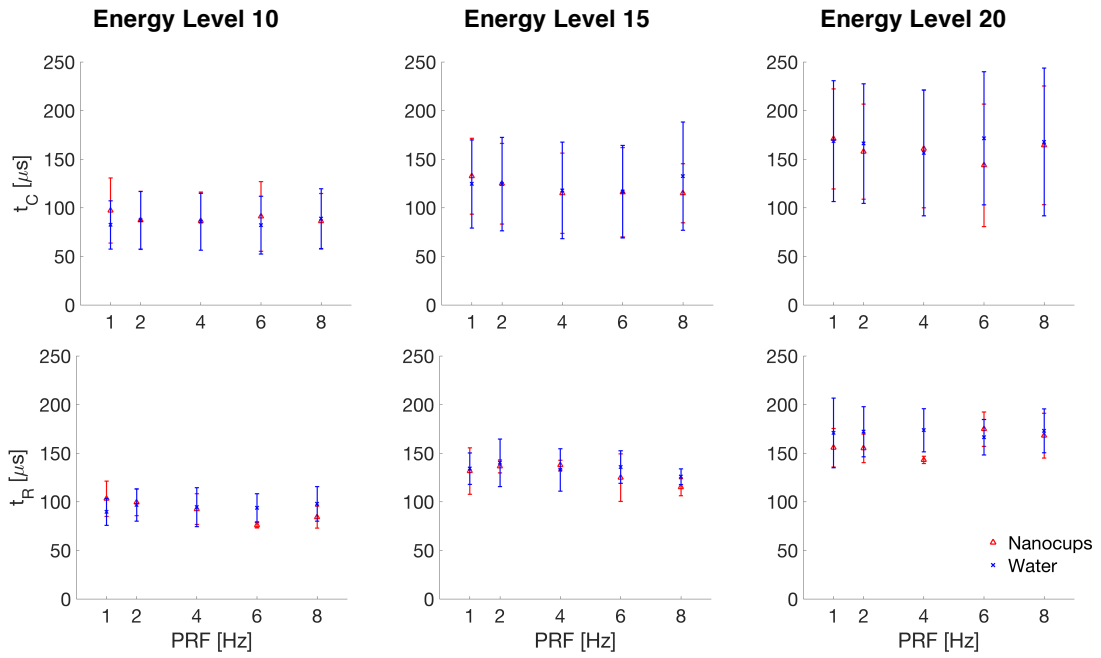


Figure 3.14: Cavitation dynamics of nanocups and water flowing through a tube at different rates of SW delivery. Each column shows the dynamics for a energy level. The top row shows the characteristic time, t_C, and the bottom row shows the rebound time, t_R.

previous case with a knee appearing at EL 6 rather than EL 5, which means that the presence of the tube and the flow has shifted the cavitation threshold. However, the cavitation does not change with the nanocups compared to the control case.

The rebound detection times from EL 1 to 6 appear to be at approximately 50 µs (figure 3.13B). The flat response implies a noise level of 50 µs and that no rebound collapses were occurring until EL 6. From EL 6 to 20, t_R increases but significant differences between the nanocups and the control cannot be seen.

In figure 3.14 the cavitation dynamics at different rates of SW delivery are shown for three ELs. Both times increase with the EL, however, at all ELs the PRF does not appear to affect the cavitation dynamics. Furthermore, no significant difference between the nanocups and the control can be seen.

3.4 Discussion

The therapeutic bioeffects of SWT are linked to the mechanical stresses, of which the dominant processes are likely the high peak positive pressure and the short rise time of the SW and cavitation caused by the tensile force of the rarefractional tail of the pressure wave [27]. The goal of this work was to assess the acoustic and cavitation field of an EMS PiezoClast to provide a better insight into the physical mechanisms that could contribute to its action in SWT.

The peak pressures reported here are lower than those indicated by the manufacturer (11.5 MPa to 82.2 MPa). The measurements of the acoustic field show that the EMS PiezoClast produces an acoustic pressure wave with positive pressures of 5.9 MPa at the lowest and 25.9 MPa at the highest EL. Over the same change in energy setting the peak negative pressure changes from −1.9 MPa to −3.7 MPa. Given the relatively large diameter of the hydrophone (<0.5 mm) compared to the width of the focal region, averaging over the sensitive area of the hydrophone might have affected the reported pressures. The acquisition of the negative pressure wave might have also been affected by cavitation on the needle hydrophone tip. Thus, the tensile tail of the waveforms appear to be truncated and the duration of the tensile tail is shorter than expected. While the amplitude of the peak negative pressure doubles from EL 1 to 20, the peak positive pressure increases by a factor of four. The smaller relative increase in p^- might also suggest non-linear effects that would cause a sharper increase in peak positive pressures. Previously, SWs with EDs from 0.06 mJ mm^{-2} to 0.28 mJ mm^{-2} have been administered in clinical SWT studies. At the focus of the EMS PiezoClast, ED_+ of up to 0.1 mJ mm^{-2}, which is lower than reported by the manufacturer by a factor of four, were measured. The negative EDs were not determined in this work due to limitations in measuring the negative pressures with a needle hydrophone. The maximum value for the ED_- would be for

a symmetric waveform, as in that case ED_- should equal ED_+.

The decreasing rise time of the EMS PiezoClast (from 272 ns at EL 1 to 185 ns at EL 20) further suggests that the waveforms are more distorted and non-linear at higher ELs. However, a pressure rise by a factor of four has led to a drop in the rise time. In lithotripsy, SWs can reach peak pressures exceeding 100 MPa that can have a rise time too short to be measured by current hydrophones (<5 ns). The rise time depends on the pressure of the waveform and the type of excitation and published literature values indicate that electro hydraulic sources have the shortest rise times and piezo electric sources the longest rise times [55]. For example in SWL, the Dornier HM3 at a focal pressure of 40 MPa has a rise time of <10 ns whereas the Piezolith 2200 has a rise time of 130 ns at 56 MPa [55]. The pressure waves observed for the EMS PiezoClast have a similar signature but are lower in amplitude and have a larger rise time. Further to a larger source pressure, lithotripters typically also have a larger aperture that will increase the focal pressure.

The −6 dB focal region of the EMS PiezoClast was measured to have a cigar-shaped volume that is 11.2 mm by 2.6 mm at the lowest energy setting and decreases to 8.0 mm by 1.8 mm at the highest energy setting. In figure 3.7, it was shown that the peak positive pressure rises sharply for higher ELs as closer to the focus the non-linear effects result in a larger peak positive pressure. Thus, the pressure threshold for the −6 dB contour increases and the focal volume shrinks at higher ELs. However, for a more effective assessment of the source, the volume exposed to a pressure threshold should be considered rather than the −6 dB focal region. For example using a fixed threshold of 10 MPa, at EL 20 the focal spot is 10 mm by 2.5 mm whereas for EL 5 it is zero. However, at present it is not clear what the absolute pressure for a therapeutic effect is.

Further to the drop in the peak pressures, it was shown that for 1 mm of lateral motion the shape of the acoustic wave changes with an increase in the duration of the

waveform, suggesting that even within the −6 dB volume the treatment site experiences a varied physical stimulus. Further, the pressure waveforms reported here were measured in a water tank. When used clinically, the acoustic field will be aberrated and attenuated by the soft-tissue and strongly reflected by bone. For mechanisms to be considered, specific geometries should be considered. Furthermore, it is challenging to deliver the pressure wave to a desired treatment site during a clinical treatment, given that the source is not designed to be operated with a diagnostic probe.

The key contribution of this work is to detect and map cavitation due to SWs. The PAM waveforms exhibited the double-bang signatures that have been reported in SWL with t_C on the order of 100 µs, which increases with the EL. The data suggests that the main collapses occurred in isolated locations. Simulations [127] and in vitro work [128, 174] have shown that t_C also increases with the pressure of the incident wave during lithotripsy. For comparable incident pressures the results reported here seem to be in agreement with in vitro work done previously. Rebound collapses were also detected and the rebound time was shorter than the characteristic time. The amplitude of the cavitation signals increased with EL and was higher in the main collapse than the rebound collapses.

It was shown that in the water tank t_C and t_R are affected by the PRF at ELs 10 to 20. However at EL 5, the cavitation dynamics were barely affected by the PRF and from EL 1 to 5 the rebound times were flat, which might suggest that collapses were either less violent or did not cause a rebound. Given that cavitation is likely a contributing factor in the bioeffects of SWT, the clinical effect of altering the PRF should thus be considered. Currently, the focus of many clinical studies lies in finding an effective number of SW or total ED delivered.

The cavitation dynamics of nanoparticle cavitation nuclei has also been determined in this work by flowing nanocups through a tube placed at the focus of the SW

source. In a HIFU field similarly sized particles have an inertial cavitation threshold of <1 MPa [175]. This peak negative pressure is exceeded at every EL of the SW source used in this chapter (p^- at EL 1 was −1.9 MPa), and thus, it was anticipated that nanocups would cavitate at all ELs of the SW source. The results in this chapter suggest that cavitation was detected for all ELs with a characteristic time of >50 µs.

The characteristic and rebound times increased with the EL similar to the cavitation in water. In all three cases (nanocups or water flowing through a tube and water without a tube), the dynamics appear to change after EL 5 or 6, where the rebound time experiences a step change from ∼50 µs to >75 µs. It is possible that the collapses become more violent as the negative pressure exceeds −2.3 MPa and that rebounds only start to occur at EL 6.

The similarity of the cavitation dynamics for water and nanocups might suggest that the initial size of the bubble does not affect the characteristic and rebound times. Simulations have previously shown that increasing the initial bubble size from 1 µm to 10 µm has no effect on the characteristic time of cavitation when the bubble is hit with a SW of 10 MPa to 100 MPa [127]. It can be assumed that the cavitation in a water tank with no tube was also nucleated from small impurities which might be similar in size to the nanocups. Note however, that the focus of the source is larger than the tube that was filled with nanocups suggesting that cavitation could have also occurred outside of the tube. Furthermore, the resolution of the PAM algorithm used here exceeds the diameter of the tube, and thus, cannot differentiate between cavitation on the surface of or within the tube.

It was shown that the cavitation dynamics of nanocups or pure water in a tube is not affected by the rate of the SWs. The difference to water with no tube suggests that the presence of the tube eliminates the effect of PRF regardless of the nanocups. Two hypotheses for this behaviour are proposed. First, the data from the water

tank suggests that the bubbles at higher PRFs grow larger and the walls of the tube prevent the bubble diameter exceeding 0.33 mm, and thus, limiting the characteristic time to <250 µs. However, it might be more plausible that higher PRFs create bubble clusters in the tank that collapse with large characteristic times when no tube is present but that the presence of the tube inhibits the creation of such clusters.

The total calculation time for PAM depended on the number of peaks that were detected in a signal and measured between 3 s and 5 s, which precludes mapping every SW for rates faster than 0.2 Hz. However, creating maps at 3 SW intervals (for a rate of 2 Hz) can still be considered. The calculation time could be reduced by analysing fewer peaks or by employing a compiled code.

3.5 Conclusions

In summary, the acoustic and cavitation fields of a hand-held piezoelectric SW source, the EMS PiezoClast, which is used to treat musculoskeletal disorders and chronic pain, have been characterised. Acoustic parameters, such as the focal pressure, the acoustic field, and the size of the focal volume were measured using a PVDF needle hydrophone by 1-D and 2-D scans in water. Passive acoustic mapping was used to detect and localise cavitation due to SWs by measuring emissions with a diagnostic ultrasound array. The novelty of this work, lies in using PAM by isolating acoustic emissions from cavitation, which are not distinct in frequency from the incident SW, demonstrating that PAM could be a powerful monitoring tool in SWT and by extensions SWL, as will be shown in chapter 4. Cavitation events were localised in space and their characteristic time was determined. PAM will provide feedback on cavitation which may be beneficial if occurring at the treatment site but may result in unwanted side-effects if occurring elsewhere. Finally, nanocups, which have previously been used as cavitation nuclei in drug delivery applications,

were exposed to SWs in a flow experiment. However, no significant difference to the cavitation dynamics of flowing water could be detected.

4 Passive Acoustic Mapping During SWL

This chapter expands on the work in the previous chapter and applies cavitation detection using PAM to experiments with a clinical lithotripter. Ex vivo kidneys and model stones were used as targets and the experiments were monitored with two probes, an in-line P4-2 and an out-of-line L11-4. During a ramp experiment, it was found that the characteristic time in kidneys increased from energy setting 6 to 9 from 560 µs to 700 µs. At EL 6 no effect on the characteristic time was determined by changing the rate of SW delivery from 1 Hz to 2 Hz. During a longer exposure to 3000 SWs, it could be seen that throughout the experiment several cavitation clusters were detected. Finally, targeting cylindrical model stones showed that the characteristic time is longer for stones compared to tissue and that cavitation occurs on the proximal wall of stones.

4.1 Introduction

Cavitation during SWL is a contributing factor to tissue damage [22, 118, 121, 126] and stone fragmentation [97, 98]. It has been shown that bubbles collapsing on the rough surface of a kidney stone might aid the fragmentation of the target due to high speed jets that are emitted from violently collapsing bubbles [97]. Furthermore, bubble clusters form proximal to the stone and either shield the target from the incident SW or collapse inertially to further fracture it [98]. However, if cavi-

tation occurs near a vessel wall, it may rupture capillaries to release blood into the interstitium [118, 121]. The pool of blood produces an envoironment for sustained cavitation, which can lead to widespread injury.

Although PCD systems have been used to detect cavitation in vivo [123, 130] and in patients [122], most of these systems do not provide a spatial map of the cavitation and are thus of limited value clinically. If a cavitation monitoring system could be developed using an ultrasound array then this would simplify the transition into clinical practice since modern lithotripters are already routinely monitored using a diagnostic ultrasound array.

Conventional PAM applied to HIFU differentiates between emissions from reflections and cavitation by using a frequency filter to extract the broadband component (due to inertial cavitation) from the harmonic component (due to the driving frequency of the therapeutic transducer). In SWL, where the SW is broadband, frequency domain filtering is not an option, however, it is expected that the emissions will be distinct in time [127]. Thus, the methodology, presented in the previous chapter, is developed further and applied to a clinical electromagnetic lithotripter source. The goal of this chapter is to detect cavitation during SWL using a conventional ultrasound probe and to use the location or the characteristic time to differentiate between cavitation occurring in the soft tissue and around the stone. The major challenge lies in differentiating between reflections and cavitation emissions that might both be registered within the same time window.

In this chapter, several experiments were performed using ex vivo pig kidneys and model stones under different exposure conditions. In each case, the acoustic emissions were measured using passive ultrasound arrays and PAM was used to localise the source of the acoustic emissions. In addition to the maps, collapses during SWL yield a characteristic time, the time between growth and collapse of bubbles. The goal is to differentiate beneficial cavitation on the stone from harmful cavitation

in tissue. The location of the cavitation on PAM and the characteristic time are assessed as parameters to accomplish that differentiation.

4.2 Methods

4.2.1 Experimental Setup

The experiments in this chapter were carried out using the clinical lithotripter in the Churchill Hospital Oxford, the Modulith SLX-F2 (Storz Medical, Tägerwilen, CH). The output from the clinical lithotripter is set in terms of an energy level (EL), which can be varied from 0.1 to 9 that reportedly results in a peak-positive pressure of 6.7 MPa to 107 MPa and a peak-negative pressure of 2.5 MPa to 16 MPa at a maximal treatment depth of 180 mm [179]. The lithotripter is fitted with an in-line ultrasound array and an x-ray source that is mounted on a C-arm, which are used for stone targeting and monitoring. To conduct experiments, the patient table was dismantled and a tank was coupled through a window (fitted with a mylar sheet) to the flexible coupling cushion of the source. The tank was filled with degassed water and phosphate buffered saline (PBS; Sigma-Aldrich Co., St Louis, MO) at 9.8 g per 1 liter of water. PBS was added to limit the deterioration of the tissue during the course of the experiment.

A Verasonics P4-2 probe was inserted in-line and interfaced with a Vantage ultrasound engine (both Verasonics Inc, Kirkland, WA) that was connected to a PC to create PAM images. The P4-2 has an aperture of 18.9 mm and a center frequency of 2.5 MHz corresponding to a wavelength of 0.59 mm in water. The distance from the array to the focus of the lithotripter, when the probe was fully inserted, measured approximatly 100 mm. Thus, from Eqs. (1.1) and (1.2), the transverse resolution, $\Delta x_{\text{P4-2}}$, and the axial resolution, $\Delta z_{\text{P4-2}}$, of the P4-2 in this setup can be approxi-

mated to

$$\Delta x_{\text{P4-2}} \approx 2.8 \text{ mm} \tag{4.1}$$

$$\Delta z_{\text{P4-2}} \approx 115 \text{ mm}. \tag{4.2}$$

The focal region of the Storz SLX measures 2.8 mm by 37 mm [50], and thus, although the in-line probe might still be useful to determine the characteristic time of cavitation events, it will not provide well resolved spatial information axially to determine whether cavitation occurred proximal or distal to the focus.

Thus, a second probe, a Verasonics L11-4 (centre frequency of 6.25 MHz, aperture of 38.1 mm) was added out-of-line in order to collect data simultaneously with the in-line probe. The L11-4 is attached to a manual positioning stage that is connected to the tank and placed 36 mm to 56 mm from the lithotripter focus as shown in figure 4.1. Although this configuration is not feasible in clinical practice, the out-of-line array provides a higher resolution PAM with which to compare P4-2. The theoretical resolution of the probe determined from Eqs. (1.1) and (1.2) is:

$$\Delta x_{\text{L11-4}} \approx 0.3 \text{ mm} \tag{4.3}$$

$$\Delta z_{\text{L11-4}} \approx 2.3 \text{ mm}. \tag{4.4}$$

Note that these values will change depending on the exact distance from the L11-4 to the focus. However, the resolution will remain in the same order of magnitude for all experiments in this chapter.

The Verasonics engine needed to be triggered when a SW was delivered. This was accomplished by placing a bare wire near the source to pick up the electromagnetic interference that occurs when the SW was fired. When triggered, the Verasonics engine collected data from both probes simultaneously.

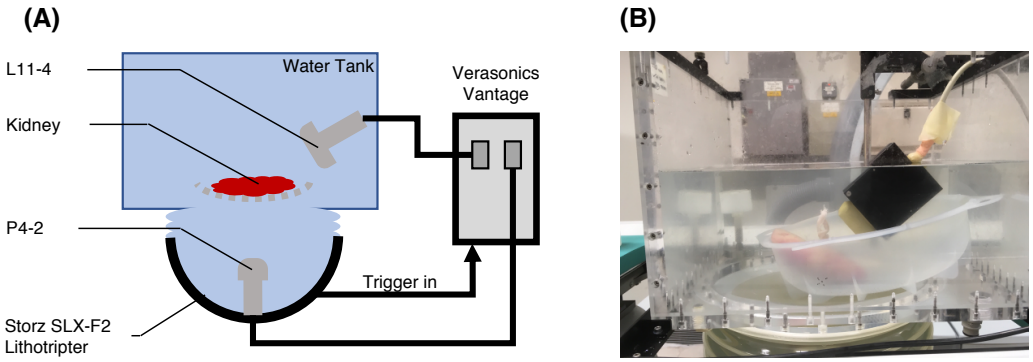


Figure 4.1: The experimental setup to detect cavitation, on two independent probes using PAM, in an ex vivo pig kidney during SWL in (A) a schematic drawing and (B) a photograph.

A steel ball, which was connected to the tank and controlled using a manual positioning stage, was moved to the focus prior to each experiment by using the x-ray monitoring system of the lithotripter. Then, the L11-4 was used to generate a B-mode image and the probe was moved until the ball was captured. The position of the ball, and thus, the position of the focus, was recorded with respect the L11-4 array. Similarly, the P4-2 probe was used to generate a B-mode image to record the position of the focus. Afterwards, the steel ball was removed from the tank and replaced by the target, which was aligned using the L11-4.

The experimental setup for detecting cavitation in an ex vivo pig kidney, which was held in place using a silicone sieve, is shown in figure 4.1. All kidneys were degassed for four hours before the experiments by placing them in an airtight chamber and using a vacuum pump at ∼40 kPa. Three different experiments were conducted using pig kidneys: First, the pressure was ramped by incrementing the operating EL of lithotripter from 2 to 9 and delivering 200 SWs at each EL at a pulse repetition frequency (PRF) of 2 Hz to the same kidney without any intermission. Second, cavitation detection during an exposure to different PRFs was examined by delivering 2000 SWs to three kidneys at EL 6 and 1 Hz, 1.5 Hz, and 2 Hz. Finally, the effects of a longer exposure were examined by exposing three kidneys to 3000 SWs each at a rate of 1 Hz, 1.5 Hz, and 2 Hz. During all three experiments, the exposure to SWs

is expected to generate cavitation in the tissue. Thus, both ultrasound probes, the L11-4 and the P4-2, were used to passively record acoustic emissions to detect and localise cavitation using PAM as will be described later.

The experimental setup for cavitation detection during stone fragmentation was carried out by placing stones in a tip of a glove (made from latex) and placed in the water tank at the focus of the lithotripter. Stone models were cast from UltraCal30 gypsum cement (United States Gypsum Co., Chicago, IL) according to [167]. The stones were cylindrical and measured 10 mm in length and 5 mm in diameter. After casting the stones, they were left in the mould for 24 h and dried for another 24 h before weighing them. Prior to the experiment, the stones were soaked for at least 24 h to eliminate any air that might be trapped in them.

Afterwards, they were aligned using the x-ray system and their location was noted with respect to the L11-4. 300 SWs were delivered to each stone at EL 6 and a rate of 1 Hz. The fragments were recovered from the latex holder and dried for at least 24 h. The fragments were then placed on a sieve to retain any fragments larger than 2 mm by 2 mm, which were weighed to obtain the remaining weight after the experiment as a measure of fragmentation success.

4.2.2 Cavitation detection algorithm

In chapter 3, it was shown that peak detection and PAM can be used in combination to determine the characteristic time of cavitation events and localise them spatially when delivering SWs using a SWT source in a water tank without a target. The characteristic time of a bubble in SWL is defined as the time between growth and collapse and can reach several 100 µs [127]. Thus, to detect cavitation during SWL, the following steps were employed for both monitoring arrays:

(i) Collect data on all elements of the monitoring arrays and filter them using a bandpass filter to reject noise, where the high-pass and low-pass frequencies were adjusted to the bandwidth of the receiving array, that is, 2 MHz to 4 MHz for the in-line P4-2 and 4 MHz to 11 MHz for the out-of-line L11-4. These filters have proven most effective, as the broadband emissions from cavitation result in a signal corresponding to the impulse response of the receiver.

(ii) Identify peaks in the signal received on the central element of each array (that is, the 64^{th} element on the L11-4 and the 32^{nd} element on the P4-2) using a minimum amplitude threshold relative to the maximum amplitude in the signal, $V_{\max}$, and a minimum separation time between peaks. The amplitude threshold was initially set to $\frac{1}{5}V_{\max}$ for the P4-2 and $\frac{1}{15}V_{\max}$ for the L11-4. A different threshold was needed, because the out-of-line probe was exposed directly to the incident SW, which resulted in a higher peak signal. The time separation was set to 40 µs from the peak on both probes.

(iii) Construct a time window of ±20 µs around each peak to construct a PAM image for each peak by beamforming the segmented signals received on all elements of each array using the RCB beamformer [141]. It was determined that a PAM image with a maximum source energy of less than 5×10^{-14} falls below the noise threshold.

The targets used in the experiments in this chapter result in complex acoustic fields. For example, the incident SW might reverberate in the target and/or reflect back into the tank from the water-air interface. These reverberating or reflecting signals might be registered on the monitoring arrays and detected as peaks as they cannot be differentiated from the acoustic cavitation emissions by applying a frequency filter as both are broadband. However, reflections from stationary objects will result in an almost identical peak detection time throughout the experiment and at all ELs, while cavitation is stochastic in nature and with increasing EL should result in longer

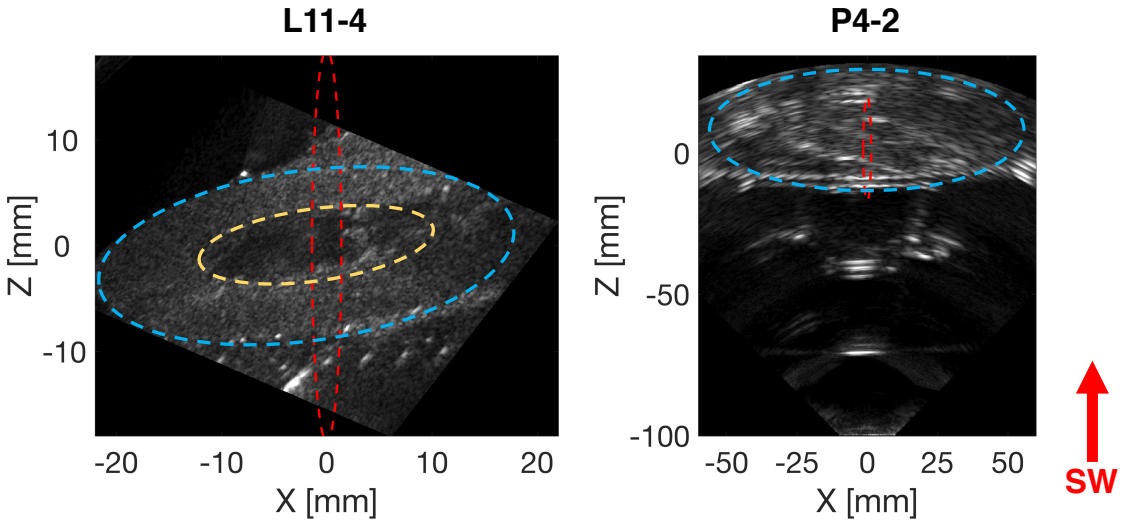


Figure 4.2: Sample B-mode images of a kidney in the water tank acquired on the L11-4 and the P4-2 before exposure to SWs. The red dashed line shows the contour of the −6 dB focal region of the SW source, the blue dashed line represents the outline of the kidney, and the yellow dashed line encompasses the collecting system. The SW is coming from the bottom and is aligned at the origin of the coordinate system.

duration and more intense cavitation. The consistency in identical peak detection times will be used to distinguish reverberations from cavitation.

4.2.3 B-mode

The L11-4 and the P4-2 probes can also be used to create B-mode images of the targets in the tank. Consequently, the maps created with PAM can be overlayed on the B-mode image to identify the location of the activity with respect to the target. Figure 4.2 shows B-mode images of a kidney in the tank created with both probes. The image created with the L11-4 has to be rotated as the probe was placed at an angle as shown in figure 4.1.

The blue dashed line identifies the contour of the kidney that has a granular appearance on B-mode. The speckles are due to the scattering off the inhomogeneous tissue of the kidney. The collecting system (shown in yellow) is filled with fluid and thus appears hypo-echoic. Similarly, the water surrounding the kidney appears in

hypo-echoic. Isolated hyper-echoic reflections can also be identified on the L11-4 that are most likely due to larger bubbles in the water. The focus of the source has been aligned with the collecting system of the kidney.

It can be seen that the resolution of the L11-4 is better due to the higher frequency and aperture of the probe. The poor resolution of the P4-2 makes it challenging to identify the collecting system. An echo at $Z = -40$ mm shows the reflection from the interface between the tank and coupling cushion of the lithotripter.

4.3 Effect of the energy level

4.3.1 Representative signals

In the first experiment of this chapter the same kidney was subject to 200 SWs at each energy setting from 2 to 9. Figure 4.3 shows sample traces that were received on the central element of the probes at three ELs. Considering the distances between stationary objects in the tank, and the corresponding times of flight, peaks that are due to reflections can be singled out. The diameter of the reflector of the lithotripter measures 300 mm and the focal distance is 165 mm. It follows that it takes the SW approximately 212 µs to arrive at the focus. The L11-4 was placed 36 mm from the focus. The P4-2 was placed 100 mm from the focus, that is, a signal from the focus will arrive on the P4-2 43 µs after the L11-4. The vertical distance from the focus of the lithotripter to the water surface was 120 mm.

On the L11-4, the incident SW was registered at 240 µs in all three cases. The detection time corresponds to the time of flight from the source to the probe via the focus and the signal will include the scattered SW and emissions from the initial bubble growth. At 355 µs a consistent signal is detected at all three ELs most likely

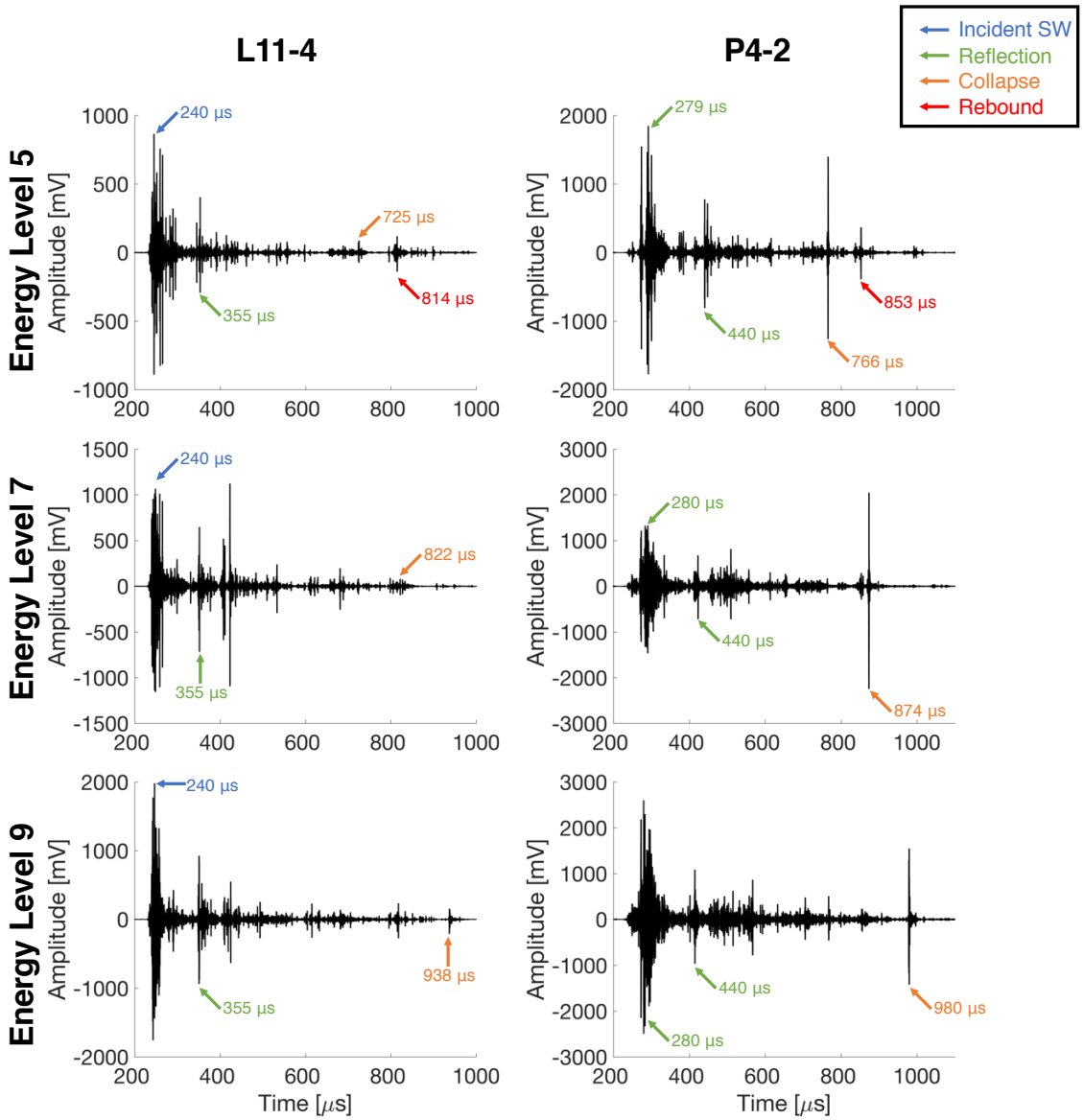


Figure 4.3: Sample traces received on the centre element of the L11-4 (left) and the P4-2 (right) at ELs 5, 7, and 9. The rows show representative signals corresponding to the same SW. The arrows indicate the detection times of the incident SW, reflections from the kidney and the water surface, collapses, and rebounds. Although the signals from the L11-4 have a poor signal to noise ratio, time of flight information can be used to identify the main collapse. It is possible that a rebound at EL 7 and 9 occurred outside of the frame.

due to the reflection of the SW from the water surface. At ELs 7 and 9 a consistent signal is also detected at 420 µs. The lack of a similar event at EL 5 suggests that this signal is not due to a reflection. Afterwards, several emissions that are smaller in amplitude are detected at all ELs. Due to the low signal to noise ratio, the emissions recorded on the L11-4 may be unreliable.

The signals on the P4-2 show that a reflection of the SW from the proximal surface of the kidney is detected on the P4-2 at 280 µs. The reflection from the water surface can be seen at 440 µs. The reflection is followed by an emission from a collapse at 766 µs and a rebound at 814 µs. For EL 7 and EL 9, the features of reflection, first bang, reflection, and collapse can be seen. The characteristic times occured at 874 µs at EL 7 and 980 µs at EL 9, which is consistent with cavitation being driven harder. A new feature at was a local peak at ∼500 µs. At ELs 7 and 9 no rebound collapse was detected, which could be due to the emissions arriving later than the size of our frame.

Comparing both traces received at EL 5, it can be seen that the main cavitation event detected on the P4-2 maps to a signal received on the L11-4 at 725 µs and that the subsequent rebound maps to a signal at 814 µs. Given the difference in travel time from the focus to the probes, the events on both probes likely correspond to each other and originate from near the focus. The main cavitation event at EL 7, however, is detected at 822 µs, that is, 10 µs earlier than expected if it originated from the focus. Finally, at EL 9 the cavitation event detected on the P4-2 also maps to an event on the L11-4 at 938 µs.

4.3.2 Localisation of cavitation

In figure 4.4, four selected maps created on the in-line P4-2 for a SW at EL 5 are shown. The maps show an elongated region of activity along the axis of the

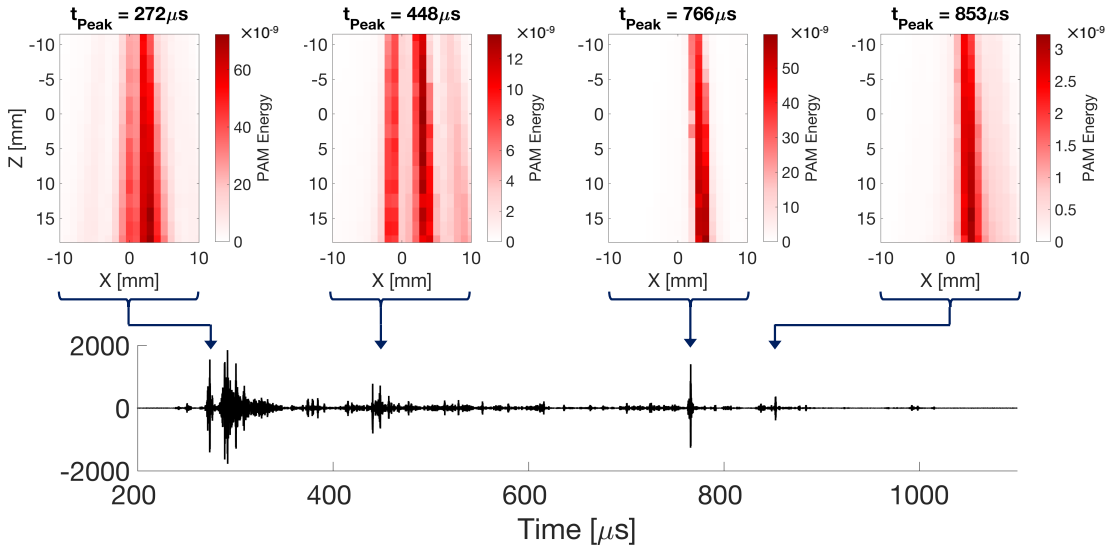


Figure 4.4: PAM images created with the P4-2 for a SW at EL 5. The axial resolution (in Z) exceeds the size of the frame, resulting in vertical lines that span the entire frame. Each panel in the top row corresponds to a peak that is identified in the row below. The focus of the lithotripter was at the origin of the PAM frames.

diagnostic probe and along the SW propagation, cutting across the entire frame, as the axial resolution exceeds the size of the frame. The first frame shows the detection of the reflected SW at 272 µs. The second one corresponds to a reflection of the SW from the water surface. It can be seen that two distinct bands are formed across the frame. The trace in figure 4.4 shows that the signal that was used to create the second frame has two distinct peaks within it resulting in two different locations of activity, and thus, two bands across the PAM image. The third image corresponds to the major collapse at 766 µs with a characteristic time of 486 µs. The activity was more narrow than the reflections detected in frames one and two and had a PAM energy similar to the first frame.

More peaks were identified in the signal than have been shown in figure 4.4. Given the limitations of the axial information, lateral slices of the PAM frames have been extracted and combined to reduce the data and show the evolution of the maps across the signal for three ELs (figure 4.5). The peaks occurring before 350 µs are likely to be caused by reflections from the kidney and its internal structures. The initial growth of any bubbles would also be captured in this time segment. It can be

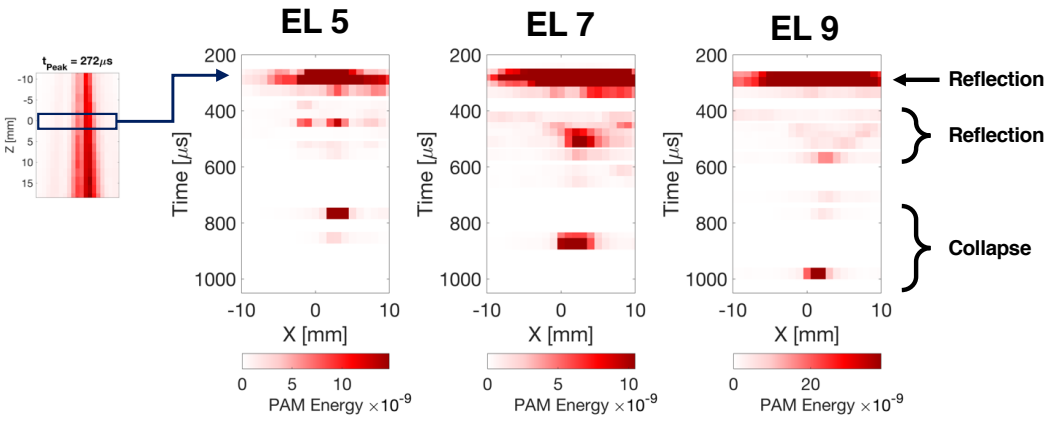


Figure 4.5: Combination of lateral slices of the PAM images created at different peak times for a SW at EL 5, EL 7, and EL 9. The colourmaps were saturated for a better illustration of the activity.

seen that the energy is spread laterally over the entire map. Similarly, the reflection at 448 µs results in a more diffused map. As previously outlined, the major collapse occurred later at 766 µs and is narrower than the reflections.

The lateral slices of the PAM created on the P4-2 for EL 7 and EL 9 are also shown in figure 4.5. A similar structure of reflections from the kidney, reflection from the air, and emissions due to cavitation can be been. The initial maps (<350 µs) due to reflections are broad, while the main collapses results in narrower map. The main collapse moves from 766 µs at EL 5 to 874 µs at EL 7 to 980 µs at EL 9, which is the result of a larger driving pressure.

PAM images were created for the same SWs on the L11-4 as well. Figure 4.6 shows three PAM frames that have been created at three time points at EL 5. The PAM images are overlayed on B-mode to indicate the location of cavitation within the target. It can be seen that the focus of the lithotripter (dashed line) was aligned with the collecting system of the kidney. The first peak corresponds to the reception of the scattered incident wave. The activity results in a PAM energy $> 600 \times 10^{-12}$ and occurs laterally shifted to the focus. The second peak corresponds to cavitation in the collecting system of the kidney with a characteristic time of 480 µs. The cavitation results in a PAM energy that is lower by two orders of magnitude than

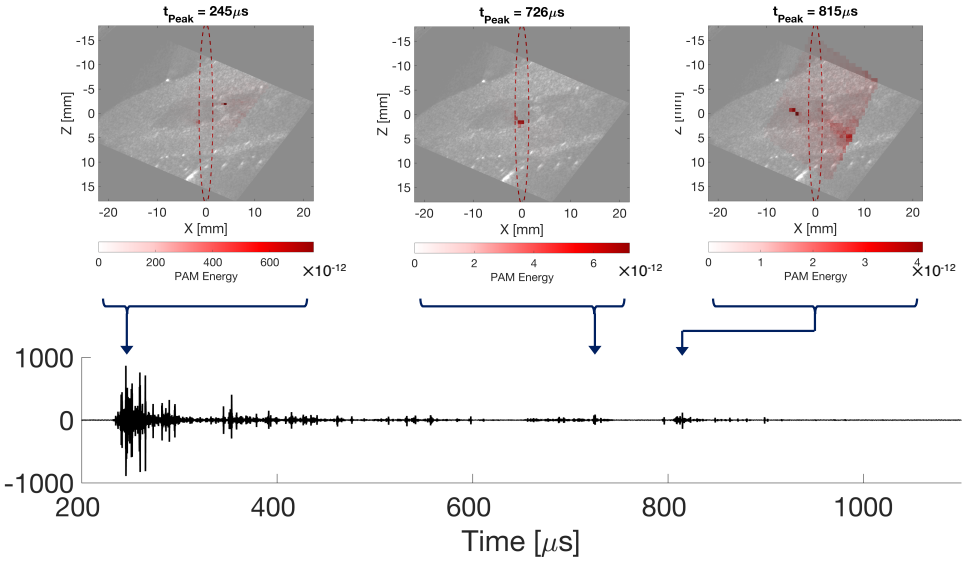


Figure 4.6: PAM overlayed on B-mode (both created with the L11-4) for a SW at EL 5 where each panel in the top row corresponds to one peak. The time of the peak is identified on the signal received on the central element of the array. The poor signal to noise ratio in the signal results in unreliable peak detection, although the beamforming algorithm in PAM can nonetheless localise the source of the emissions. The focus of the lithotripter was aligned with the collecting system of the kidney. The dotted line shows the contour of the −6 dB focal region of the lithotripter. The PAM Energy colour scale is changing by two orders of magnitude.

the incident wave. The third peak results in cavitation off-axis.

The collapses were previously identified on the P4-2 and, using the L11-4 shows that they originated from the collecting system of the kidney. The last event at 853 µs corresponds to the last event seen on the L11-4 as well and is likely caused by a rebound in the collecting system. Although the maps created on the L11-4 (figure 4.6) suggested that the location of the activity changed between the final two collapses, no shift in the lateral direction can be seen on the P4-2 between frames three and four, although the theoretical resolution of PAM should be sufficient to distinguish between the source locations.

Figure 4.7 shows PAM images created for a SW at EL 7 on the L11-4. The first frame (352 µs) shown for the L11-4 shows a peak that corresponds to the reflection of the SW from the water surface. The activity is spread over a section to the far end of the map. The second (724 µs) frame shows activity at a location near the focus in the collecting system of the kidney. The peak that the map was created from is low

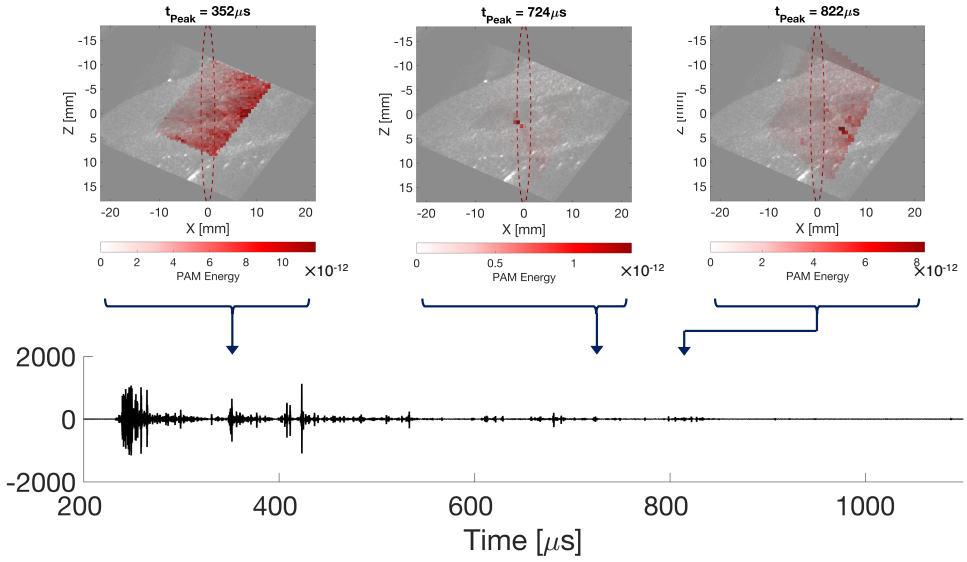


Figure 4.7: PAM overlayed on B-mode for a SW at EL 7 where each panel in the top row corresponds to one peak identified on the signal in the bottom row.

in amplitude. No corresponding peak at ∼767 µs was detected in figure 4.5, which might be due to the low source energy of the activity and that the peak fell below the detection threshold on the P4-2. Finally, the third map (822 µs) results in an event laterally shifted from the focus at $X = 6$ mm. The event was also detected on the P4-2 as the main collapse at 874 mm. Both on the L11-4 and the P4-2 map the event is shifted laterally in the X^+ direction, however, the L11-4 places the event further from the focus than the P4-2.

Figure 4.8 shows the PAM images created for a SW at EL 9. In the first frame on the L11-4, the detection of the incident wave on the probe is shown. The map shows scattering from the focus of the lithotripter and activity at a lower source energy at the far end of the map. The second and third frame show activity at 818 µs and 937 µs. Both are away from the focus laterally (although in opposite directions) and occur pre-focally in the kidney tissue. A longer characteristic time compared to the events detected at EL 5 and 7 is consistent with the larger incident pressure.

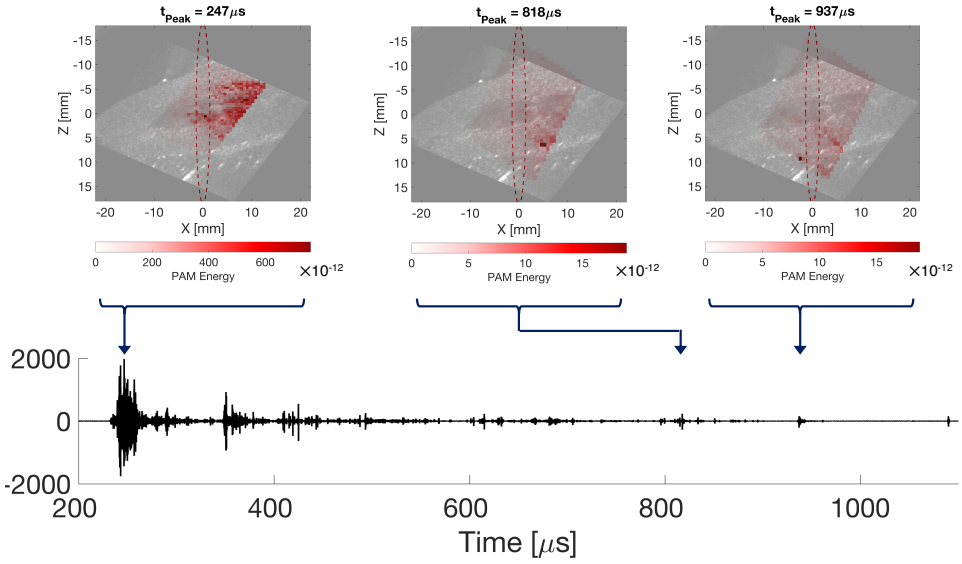


Figure 4.8: PAM overlayed on B-mode for a SW at EL 9 where each panel in the top row corresponds to one peak in signal received on the central element of the L11-4 shown below. Note that the colourmap changes by one order of magnitude between the frames.

4.3.3 Peak detection times

After showing the data for individual SWs at selected ELs, the data collected over the course of 1600 SWs and from EL 2 to 9 was reduced for a more compact representation. Figure 4.9 shows the histogram of the peaks detected throughout the ramp experiment at all ELs for both probes. The colourbar shows the PAM energy that was determined due to the peaks.

Consider the histograms from the out-of-line probe first, shown in figure 4.9. First, at all ELs the scattered incident wave is detected at 245 µs followed by more events that could be the result of reverberating sound in the kidney. The detection time of these events corresponds to the time of flight from the SW source, to the probe via the focus and the detected signal will include the scattered SW and emissions from the initial bubble growth. At 350 µs, a signal is detected on a majority of SWs delivered at ELs 5 to 9. The consistent time corresponds to the travel time from the source to the water surface and to the L11-4. At ELs 2 to 4, the peak was detected less frequently, probably because the amplitude of the peak was below the threshold

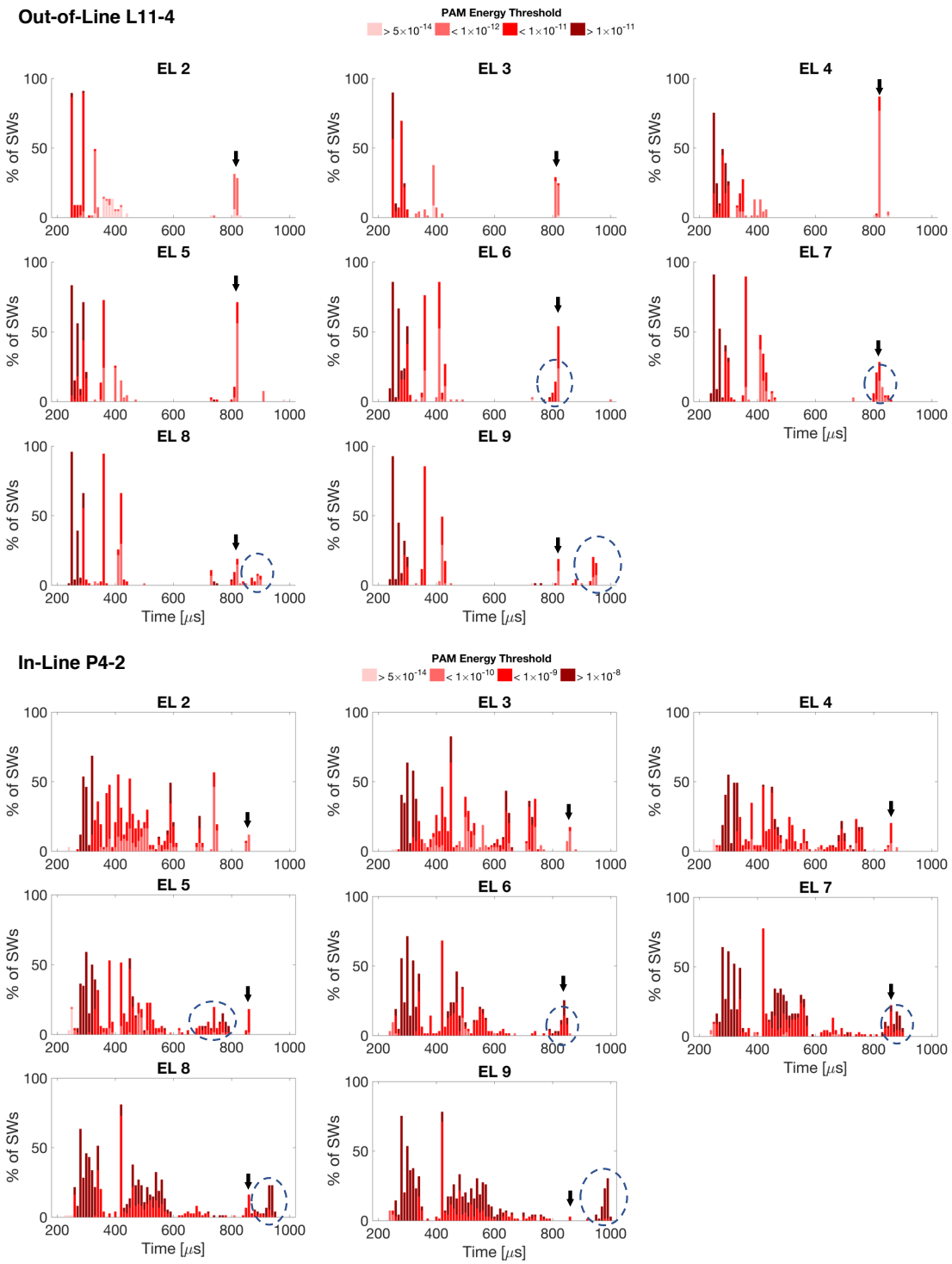


Figure 4.9: Histogram of the peak times detected during an experiment where a pig kidney was subject to 200 SWs each at ELs 2 to 9. The three top rows show the histograms on the out-of-line monitoring array (L11-4) and the three bottom rows show the histograms of the in-line probe (P4-2). The arrows indicate fixed peak times that are consistent and the dashed ovals show clusters that correspond to cavitation. The clusters due to cavitation shift with time as the EL is increased.

in most cases. From 400 µs to 500 µs, a cluster of events can be seen at all ELs. The number of events in this cluster increases between EL 5 and 6, however, the detection time of the cluster does not increase with the EL as would be expected for cavitation events. Finally, events at 800 µs are detected consistently at all ELs at the same detection times (indicated by arrows) suggesting a reflection. From EL 6 to 9 however, a cluster emerges at a similar time that moves shifts with the EL to 1000 µs at EL 9 (indicated by the dashed ovals). Thus, the characteristic time would increase from 561 µs to 711 µs from EL 6 to 9.

Now, consider the histograms for peaks detected on the P4-2 probe in figure 4.9. The reflected SW is detected at ∼280 µs. The detection time has a greater variability than the detection of the incident wave on the L11-4 because the reflection off the curved surface of the angled kidney is less consistent than the path between the lithotripter and the L11-4. From 280 µs to 350 µs several peaks are detected mostly corresponding to a source energy of $> 1 \times 10^{-9}$ and it is difficult to distinguish reflections from the internal structures of the kidney from emissions due to bubble growth. At 420 µs a reflection from the water-air interface can be seen as a consistent peak in 60 % of the SWs. It is followed by an activity cluster from 420 µs to 600 µs. Given that this structure is consistent at all ELs, it most likely is due to reverberations or scattering. At 840 µs a peak appears at a fixed time at all ELs (indicated by arrows). It is detected in less than 20 % of the SWs suggesting that the amplitude of the fixed signal is close to the amplitude threshold of the peak detection. At a similar time, a cluster appears at EL 5 that shifts in time with the EL. The structure is consistent with the L11-4 and constitutes cavitation that would originate from near the focus. The events are detected approximately 40 µs later on the P4-2 compared to the L11-4 corresponding to the time of flight difference from the focus to the probes. It is unlikely that these emissions are due to reflections, as an object would have to move ∼10 cm during the course of an experiment to cause such a time shift.

4.4 Effect of the SW rate

An experiment was conducted to examine the effect of the SW rate on the cavitation within a kidney by separately delivering 2000 SWs each at EL 6 to three kidneys at 1 Hz, 1.5 Hz, and 2 Hz. The SWs were focused to the collecting system of a fresh pig kidney in each of the three experiments. In figure 4.10 the peak detection histograms for each of those experiments is shown for the P4-2 and the L11-4. The right y-axis further shows the mean and standard deviation of the area of the event in PAM.

Figures 4.10(A)–(C) show the detection of peaks and the size of the event on the P4-2. Six segments are highlighted on the figure: First, from 240 µs to 330 µs the reflection from the kidney and its internal structures can be seen. The distribution is sharper at 1 Hz and broader at higher rates, which might be due to different levels of gas that have remained in the kidneys. Furthermore, the broader distribution is due to the curved surface of the kidney, which might tilt slightly back and forth during the experiment and change the travel time to the probe. Segment 1 also encompasses reflections from the internal structures of the kidney.

In segment 2, at 420 µs, a reflection from the water-air interface is detected. consistently. The reflection was not detected in all SWs because the some cases the amplitude of the reflection fell below the detection threshold. Segments 3 and 4 show a double-humped cluster of events from 430 µs to 600 µs, where the first hump (segment 3) is consistently larger than the second (segment 4). These segments either correspond to cavitation or are the result of scattering and reverberating sound. Given that cavitation outside of the focus of the lithotripter would be driven by a lower pressure, it should result in shorter characteristic times. In that case segment 3 would correspond to the main collapse of those bubbles and segment 4 to a potential rebound.

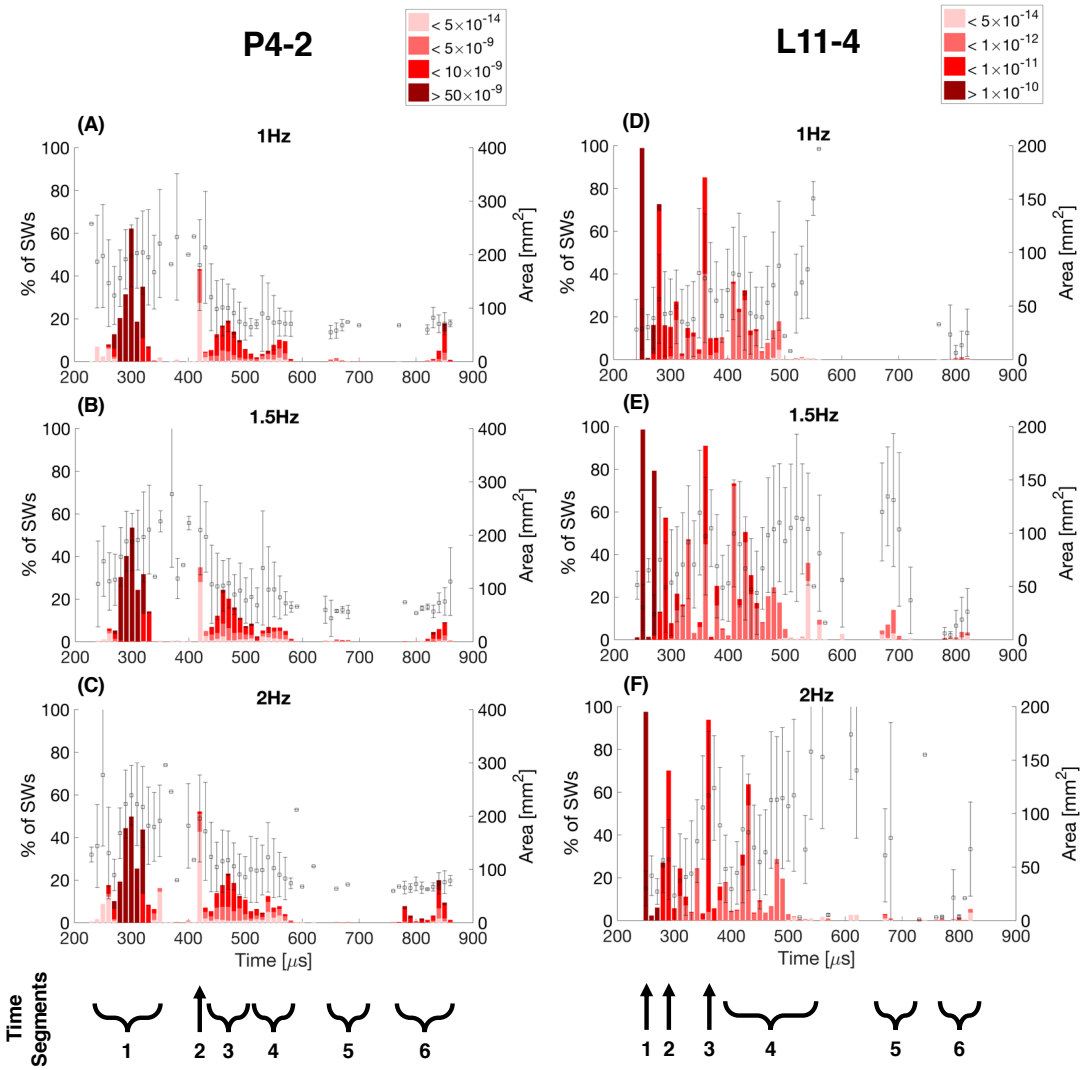


Figure 4.10: Histograms of the peak times detected on the P4-2 (left) and the L11-4 (right). For an exposure to 2000 SWs at EL 6 and at a rate of 1 Hz, 1.5 Hz, and 2 Hz. The colourbar represents the PAM energy that was detected due to that peak. The mean and the standard deviation of the area of the event in PAM that was created due the peaks is indicated on the right y-axis for each time bin. The time segments highlight detection times that were consistent throughout all experiments (arrows) and segments where peak clusters were identified (brackets).

In segment 5 hints of a cluster of events can be seen at rates 1 Hz and 1.5 Hz. Considering the previous ramp experiment, a similar structure emerged at EL 5 and EL 6 that was linked to cavitation.

Finally, a smaller cluster of is detected from 800 µs to 900 µs in segment 6. The late detection likely corresponds to violent collapses with a characteristic time of ∼550 µs. The characteristic time does not appear to depend on the SW rate.

The area of the event on PAM has been defined as the −6 dB region, that is the contour where the determined source energy is 50 % less than the maximum source energy. It is shown on the right y-axis on figure 4.10. In figures 4.10(A)–(C) the area on PAM for the majority of peaks in the third and fourth clusters is less than 100 mm^2. However, the peaks in the first cluster and the peaks corresponding to a reflection from the water-air interface at 420 µs result in larger −6 dB areas on PAM. The theoretical transverse resolution of the P4-2 is approximately 3 mm, and thus, for an axial length of 30 mm it would be reasonable for cavitation events originating from a point to occupy less than 100 mm^2. As hypothesised in the previous experiment, the area of the event on PAM created with the P4-2 might be used to distinguish between reflections and cavitation.

Now consider the peaks that have been detected on the L11-4, figure 4.10(D)–(F). Six time segments have been identified to show the features of the histograms. The structure of incident wave (segment 1), reflection from the kidney (segment 2), and reflection from the water surface (segment 3) is consistent with the structure seen in the ramp experiment.

The events after 400 µs are more stochastic and, given the long detection time, likely caused by cavitation. In segment 4, a cluster of events is detected at all SWs from 400 µs to 550 µs. There appears to be a separation of the distribution at 475 µs suggesting collapsing bubbles before and rebounds after that time. At 1 Hz both

of these parts are broad with more peaks occurring between 400 µs to 475 µs. At 1.5 Hz the peaks are detected more frequently than at the other rates. At 2 Hz the two parts become more distinct at 420 µs and 490 µs. Similar to the P4-2, hints of a double-humped signature can be seen in the peaks detected on the L11-4 as well, particularly at 1 Hz and 1.5 Hz from 400 µs to 500 µs, figures 4.10(D) and (E), in time segment 4. Between the clusters registered on the P4-2 and the L11-4, a time delay can be seen that corresponds to the travel time difference from the focus to the probes, suggesting that the activity originated from the focus.

The following segments 5 and 6 are detected less frequently at all rates. Their likelihood is largest at 1.5 Hz, particularly in time segment 5. These late peaks are most likely caused by late violent collapses.

For the data on the L11-4, it can be seen that no correlation between the size of the event on PAM and the nature of the event (i.e. whether it was due to a reflection or cavitation) can be determined, figures 4.10(D)–(F).

Overall, no clear trend that correlates cavitation with the PRF can be seen. However, at 1.5 Hz more consistent peaks and more clusters had occurred, which might be due to the particular kidney, rather than the SW rate.

Figure 4.11 shows the peak detection histograms on a P4-2 for all PAM where the −6 dB event area was smaller than 100 mm^2 for two kidneys at each SW rate. It can be seen that all consistent peaks (that is, peak times that occurred in more than 50 % of SWs) have been eliminated by applying an area threshold.

At 1 Hz, the similarities between the kidney in figures 4.11(A) and 4.11(D) include the the double-humped characteristic (from 400 µs to 600 µs). It has previously been shown to be independent of EL, which is not consistent with cavitation. In one of the two kidneys, a cluster of events emerges from 650 µs to 750 µs. Since the cluster does not appear in any other case, it is most likely a kidney specific feature. Finally,

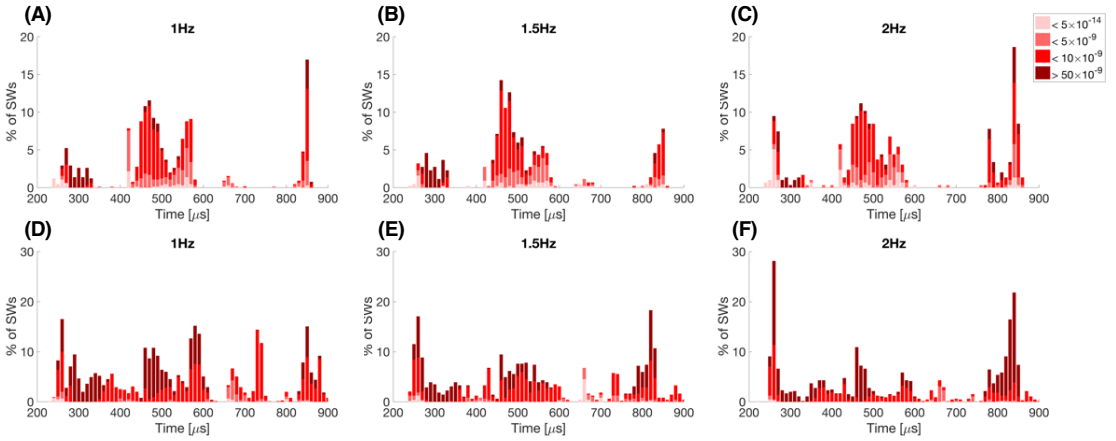


Figure 4.11: Histograms of the peak times detected on the the P4-2 during an exposure to 2000 SWs at EL 6 and at a rate of 1 Hz, 1.5 Hz, and 2 Hz, where two kidneys were exposed to each rate. The variability between kidneys exposed to the same acoustic conditions can be seen by comparing the top and bottom rows. Peaks that resulted in a PAM image where the −6 dB region was larger than 100 mm were excluded and the colourbar represents the PAM energy that was detected due to that peak.

a number of peaks have been detected after 800 µs, which might be the result of late violent collapses. In the kidney shown in figure 4.11(D), the peaks are more broadly distributed. Neither the timing of the double-humped distribution, nor the characteristic time of the late collapses are affected by the PRF.

At 1.5 Hz a similar pattern can be seen although in one of two kidneys the double-humped structure less pronounced. Instead, a broader cluster was observed in this kidney from 450 µs to 600 µs (figure 4.11E). Furthermore, a larger number of events is detected after 700 µs in the second kidney.

At 2 Hz the double-humped distribution is separated further to form two distinct clusters after 450 µs and 550 µs in one kidney (figure 4.11F). Furthermore, the number of late collapses has increased and a correlation between the rate and the number of events occurring at >750 µs can be seen, where more cavitation is detected at higher rates.

The variability between the kidneys shown in figure figure 4.11 shows that results are dependent on the specific environments in which the experiments have been conducted. However, similarities can be seen in all cases in detecting: (1) the

reflection of the incident wave, (2) a cluster between 450 µs to 600 µs, and (3) late collapses after 750 µs.

4.5 Evolution of cavitation over time

An exposure to 3000 SWs was used at rates of 1 Hz, 1.5 Hz, and 2 Hz to determine if cavitation changes over the course of a long, uninterrupted exposure to SWs. Furthermore, in this experiment the L11-4 was placed further from the focus (56 mm) because the directivity of the elements of the array might have precluded them for detecting cavitation events during the previous experiments as a result of an even minor misalignment. The target of the SWs was the collecting system of the kidney.

In figure 4.12, the peaks detected at each SW are shown as a function of their detection time for different rates for the L11-4 and the P4-2. It can be seen that vertical bands are formed at distinct times that are detected across all SWs.

Consider the L11-4 first, figure 4.12(A)–(C). The incident wave is detected at 261 µs (segment 1) throughout all experiments and this corresponds to the travel time from the SW source to the array.

Then there is a gap in emissions and a double band, identified as segment 2, is seen in all experiments from 300 µs to 400 µs. At 1 Hz the source energy in these bands is highest and more peaks appear to be detected, particularly between the bands. Furthermore, after approximately 1500 SWs at 2 Hz at 400 µs a narrowly distributed peak is detected at a consistent time. From the previous experiments and from the narrow breadth of the peak times, it can be determined that these peaks correspond to reflections, reverberations or scattering.

In time segment 3, a broadly distributed band begins at 450 µs and lasts until

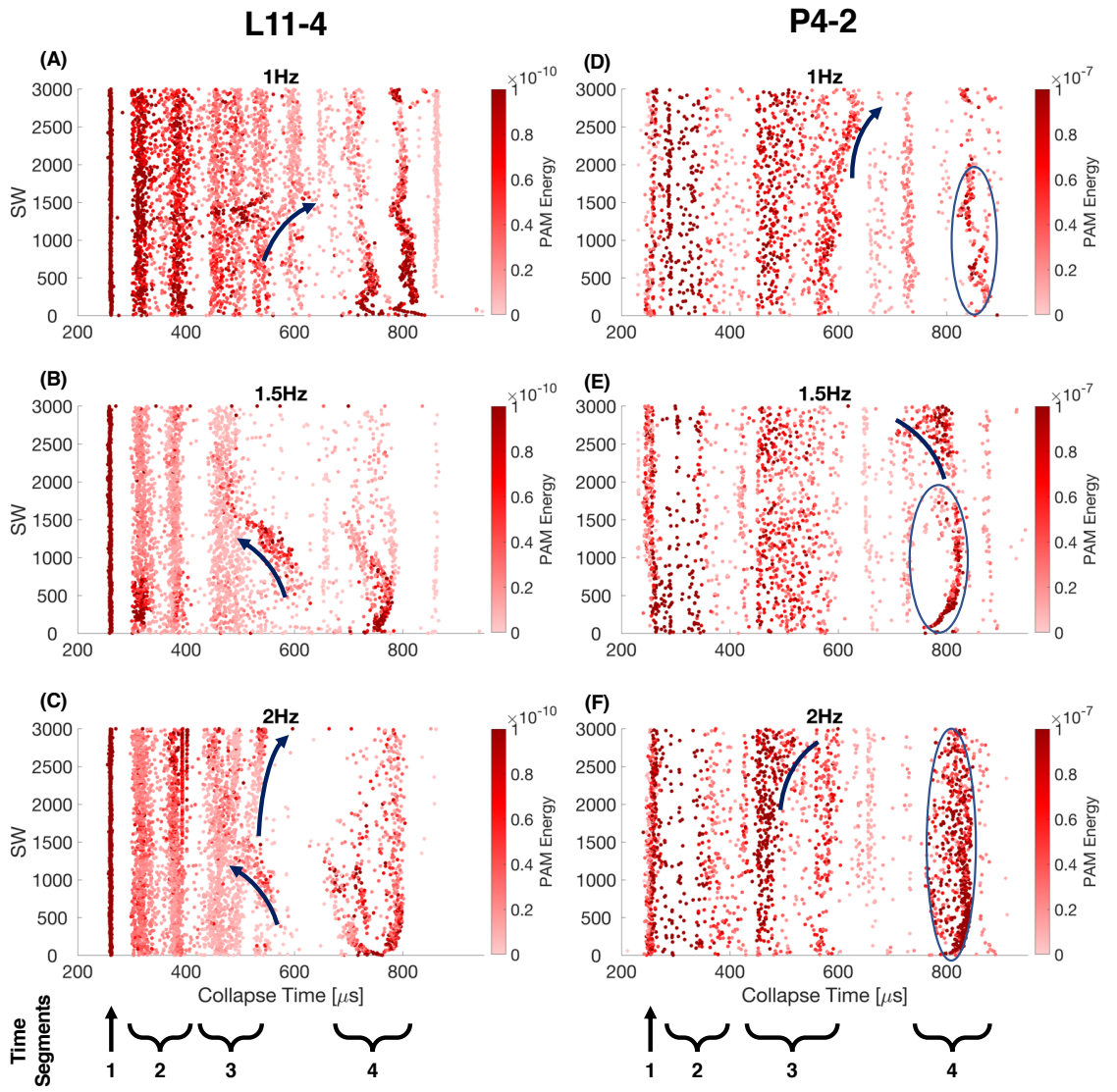


Figure 4.12: Exposure of an ex vivo pig kidney to 3000 SWs: each point represents a peak as a function of the SW number and the time it was detected at. The columns correspond to the data collected on the different probes and the rows correspond to the SW rates 1 Hz, 1.5 Hz, and 2 Hz. The colourbar resents the source energy in the PAM. Peaks that resulted in a map where the source energy as less than 5×10^{-14} were excluded. The blue arrows indicate transition times within the data.

600 µs. Several transitions occur in this segment and have been highlighted in figure 4.12(A)–(C). At 1 Hz peaks are detected throughout this time region. However, it appears that the frequency of peaks at 600 µs increases after approximately 1500 SWs. At 1.5 Hz the band is more narrowly distributed and mostly limited from 400 µs to 500 µs apart from one cluster that ranges from SW 750 to 1500. At 2 Hz after delivering 2000 SWs another cluster of peaks appears. Similar transitions have been seen in other kidney as well. However, the time of the emergence of clusters and the nature of the transitions appear to be random.

Finally in time segment 4, from 750 µs to 850 µs, the source energy drops over the course of all three experiments. It is possible that the kidneys were initially not fully degassed and that some of the larger bubbles initially collapsed violently to form these late peaks. After those bubbles have been destroyed during the first 1000 shocks, less violent collapses occur until the end of each experiment. At 1 Hz the number of peaks remains somewhat consistent in segment 4, while at 1.5 Hz it decreases. At 2 Hz the variance of the peaks grows.

The corresponding data for the P4-2 is shown in figure 4.12(D)–(F). To exclude peaks that were due to a reflections, peaks that resulted in PAM frames where the source energy was below the noise threshold and the −6 dB area was larger than 100 mm^2 were neglected. Similar to the results shown for the L11-4, the peaks arrange in vertical bands. Time segment 1 and 2, from 250 µs to 400 µs, contains peaks from the remaining reflections and might also bear the emissions from the initial bubble growth.

Segment 3, from 450 µs to 600 µs, a large number of peaks are detected. At 1 Hz and 2 Hz the band is divided in two parts: first a region of high source energy and, approximately 75 µs later, a region of lower energy. This signature is consistent with a bubble collapse and rebound cycle as previously identified in the double-humped histograms in figures 4.10 and 4.11. At 1 Hz after 2000 shocks, the distribution of

this band becomes wider. Similarly, at 2 Hz, the peak times increase by the end of the experiment. At 1.5 Hz changes are not apparent through the course of the experiment in this time band.

After 750 µs a final cluster is detected in segment 3, where the number of peaks detected increases with the PRF. At 1.5 Hz and 2 Hz, the first 1000 SWs result in emissions with a high source energy and a characteristic time that shifts later by 50 µs. These collapses might be the result of bubble clusters that collapse violently. Some of these features are not consistent with the L11-4, for example at 1.5 Hz the curvature of the peak times is different between the two probes.

4.6 Cavitation detection during stone fragmentation

Eight model stones were used as targets to investigate cavitation during stone fragmentation. The stones were cylinders measuring 10 mm by 5 mm and had an initial mass of ∼310 µg. The stones were fragmented using 300 SWs at a rate of 1 Hz. After the study, the stone pieces were sieved with a 2 mm mesh and the mass of the retained fragments are shown in figure 4.13. It can be seen that most of the stones had a remaining mass of 200 µg to 300 µg, while stone 6 fragmented particularly well and was pulverised with only 40 µg remaining. For the other stones, little fragmentation occurred but visual inspection of the surface provided evidence of erosion. Some stones were fragmented into two or three larger parts. Stones one, four, seven, and eight had a remaining weight of >280 µg, and thus, fractured poorly.

During the fragmentation of the stones, in-line and out-of-line arrays were used to determine the cavitation around the targets. The experimental setup during the fragmentation experiments is shown in figure 4.14. It can be seen that the L11-4 was aligned at a 90° angle to the SW propagation direction and to the P4-2 in these

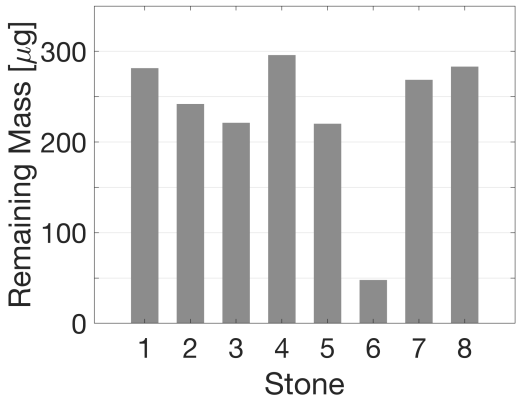


Figure 4.13: The remaining mass of stone fragments (>2 mm) after exposure to 300 SWs at 1 Hz. Stone 6 was fragmented best, while stone 4 experienced the least fragmentation.

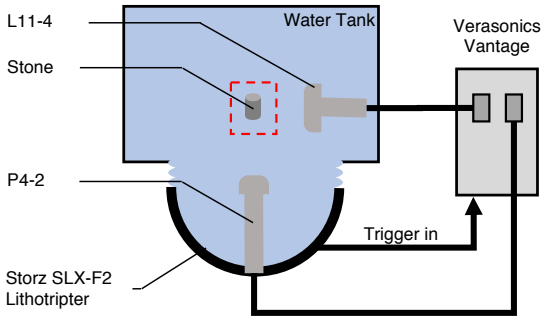


Figure 4.14: Experimental setup during the stone fragmentation experiments. The stone has been placed in a latex glove finger and aligned with the SW focus using x-ray. The L11-4 probe is placed at a 90° angle to the SW propagation direction. The dashed rectangle outlines the contour of the PAM images that were created around the stone.

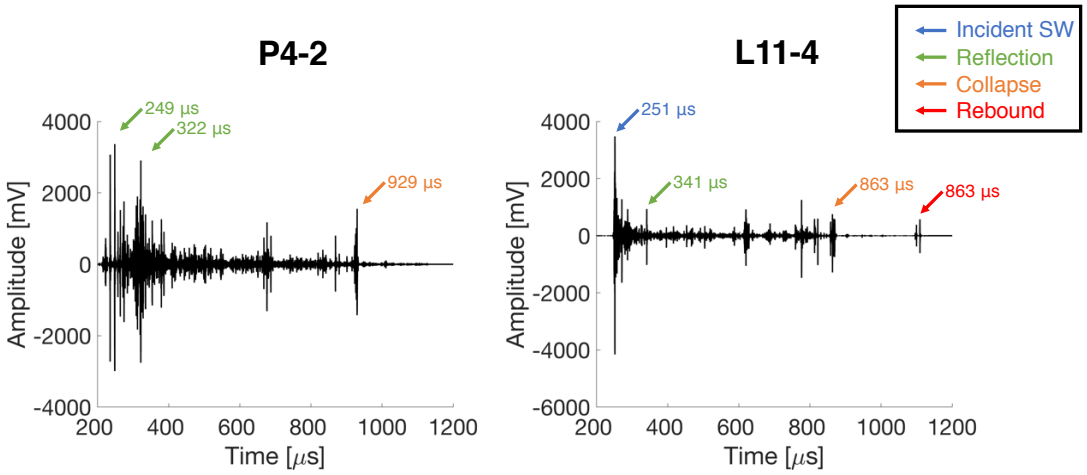


Figure 4.15: Representative signals collected on the P4-2 and the L11-4 for the SW during stone fragmentation. Some key features are highlighted.

experiments.

Figure 4.15 shows sample traces collected during the same SW on the P4-2 and the L11-4 during a stone fragmentation experiment. It can be seen that the signature is similar to the signals shown previously, when a kidney was used as a SW target. On the P4-2 trace, the structure includes emissions from the reflection of the proximal surface of the stone, reflection from the distal surface of the stone, reverberations, and the major collapse at 929 µs. Note that is likely that collapses occur on multiple locations on the surface of the stone, resulting in several emissions at different time points. The signal collected on the L11-4 shows the detection of the incident SW, a reflection from the water surface, and collapse and rebound.

Figure 4.16 shows the peaks detected on the stones after the experiments on the P4-2, where a noise theshold of $> 5 \times 10^{-14}$ and an area threshold of $<100\,\mathrm{mm}^2$ have been set to exclude reflections. The reflection from the stone is detected in all cases at 240 µs. From 240 µs to 280 µs, when the reflection of the SW is expected, few peaks have been detected on stones 1 and 6 (25 and 26, respectively) compared to 87 for stone 3. There does not appear to be a correlation between the detction of the reflected wave at this time and the stone fragmentation.

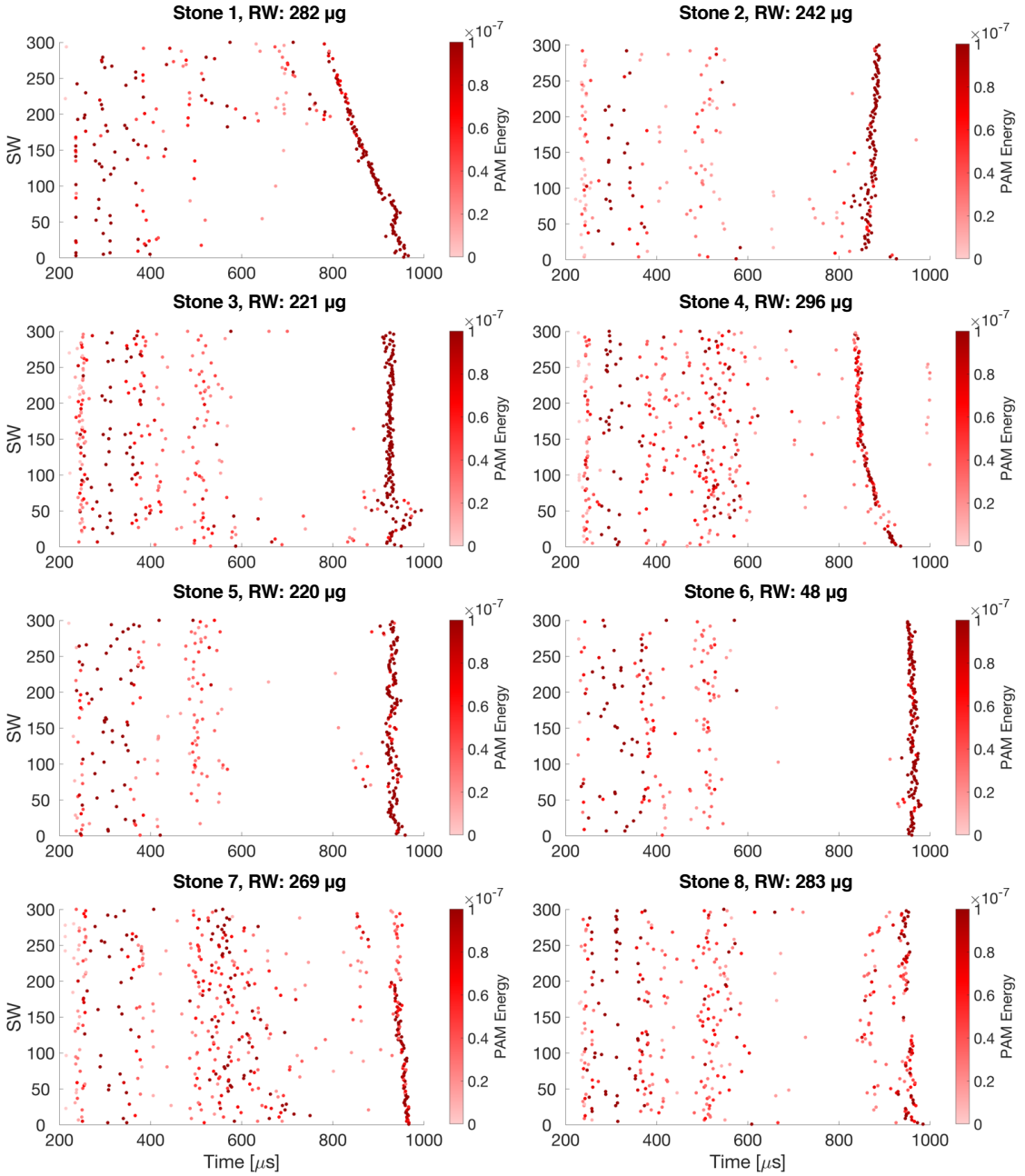


Figure 4.16: Peak detection on the P4-2 during a stone fragmentation experiment with exposure to 300 SWs at EL 6 at 1 Hz. All eight stones and their retained mass are shown.

The bulk of the peaks are detected between 380 µs to 600 µs. Hints of a double-humped distribution, one ranging from 380 µs to 450 µs and the other from 500 µs to 600 µs, can be seen again. The peaks during this segment may be due to the reflection from the water surface and reverberations in the stone. The experiment with the poorest stone fragmentation, stone 4, resulted in the greatest number of peaks in this time span.

Collapses have been detected on all stones after 800 µs. For stone 1, a consistent peak is detected at 965 µs at the first SW and it decreases in time, almost linearly, to 782 µs at the 300$^{\text{th}}$ SW. A similar pattern was observed with stone 4, where the peak time decreased from 925 µs to 836 µs. These peaks are not due to a reflection, as the object would have to move >25 cm towards the probe to produce a ∼180 µs time shift, which is unlikely. For stones 3 and 5, the final cluster of peaks appears consistently at all SWs at 930 µs and for stone 6 this time shifts to 970 µs, corresponding to characteristic times of 690 µs and 730 µs, respectively. Stone 8 produced peaks that are more broadly distributed and the peak detection times at approximately 960 µs, corresponding to a characteristic time of 720 µs.

Finally, PAM images generated with the L11-4 for selected SWs and stones. In figure 4.17 PAM images from the 12$^{\text{th}}$ of 300 SWs on stone 3 are shown. The incident wave is detected at 255 µs and results in a reflection from the surface of the stone as shown in figure 4.17(A). On the P4-2 the detection of the incident wave is followed by 100 µs, where multiple peaks are detected due to reverberations in the stone. At 772 µs a small cloud can be seen on the surface of the stone, at the focus of the lithotripter. The event shown in figure 4.17(C) shows several collapses on the stone. Emissions from the same event were also detected on the P4-2 with a time delay of 58 µs. Afterwards, the locations are in more isolated locations and it may be that several collapses and rebounds occurred. The event in figure 4.17(E) has a characteristic time of 866 µs.

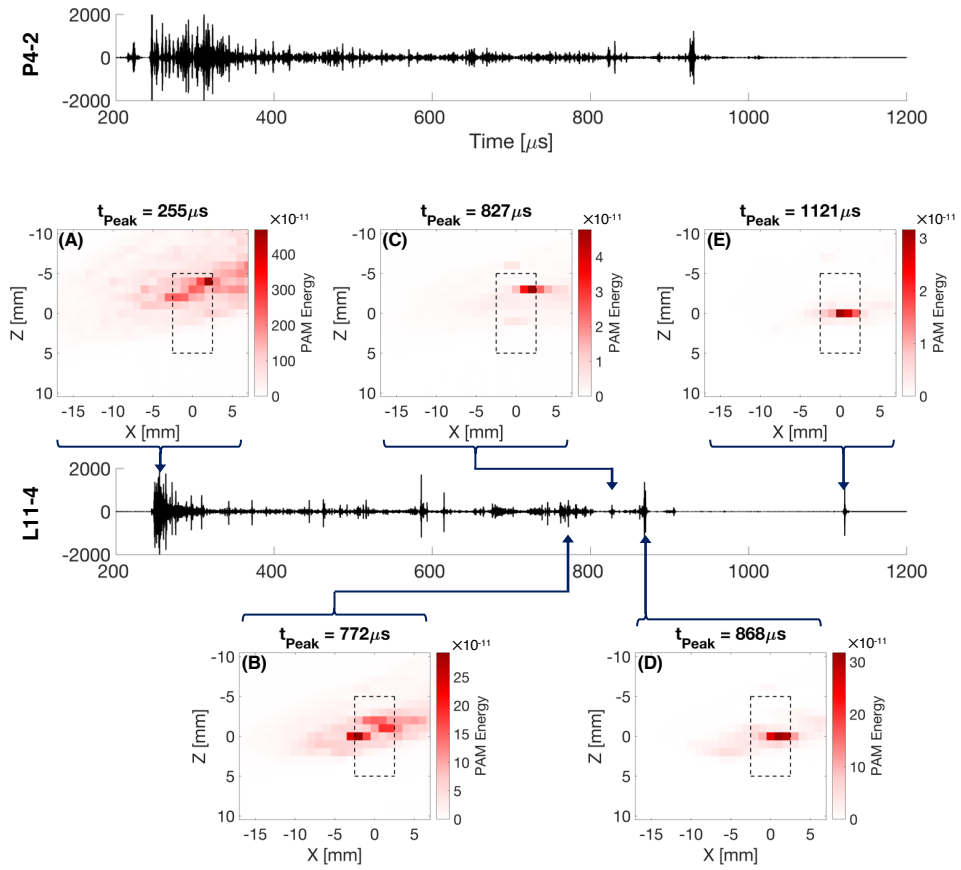


Figure 4.17: Representative PAM images generated at different peak times on the L11-4 for the 12th SW on stone 3. The RF lines collected on the central element of both probes are shown. The SW is coming from above and the dotted line represents the initial outline of the stone, but because the stone "jumps" at every SW, its orientation will vary from SW to SW. Note that the colourmap is changing by several orders of magnitude from frame to frame.

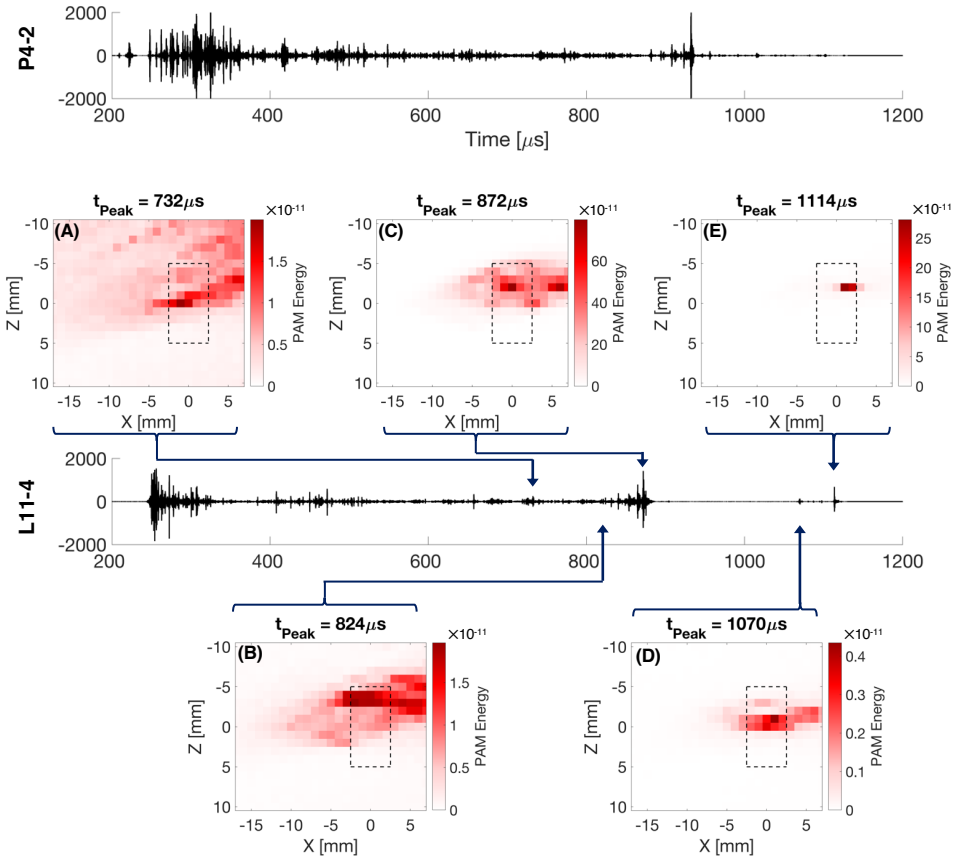


Figure 4.18: Representative PAM images generated at different peak times on the L11-4 for the 282nd SW on stone 3. The SW is coming from above and the dotted line represents the initial outline of the stone. Note that as the stone is impacted repeatedly by SWs its location will change.

Considering the 282nd SW during the same exposure (figures 4.18), it can be seen that a large area of activity is detected at a peak time of 872 µs, where a bubble cloud may have collapsed. Emissions are detected on the stone and several collapses around the around the target can be seen. Several more collapses at longer characteristic times can be seen in panels (D) and (E), where some events may be rebound collapses. The collapse shown in (E) corresponds to a collapse that was detected on the P4-2 at 932 µs.

In figure 4.19, PAM images from a different stone are shown for the 12th SW. In panel (A), a signal due to a reflection, likely from the water surface, can be seen. Panels (B) and (C) show large areas of activity on the surface of the stones. These emissions may be due to a collapsing cloud or reflections from a bubble cloud. Finally, panels

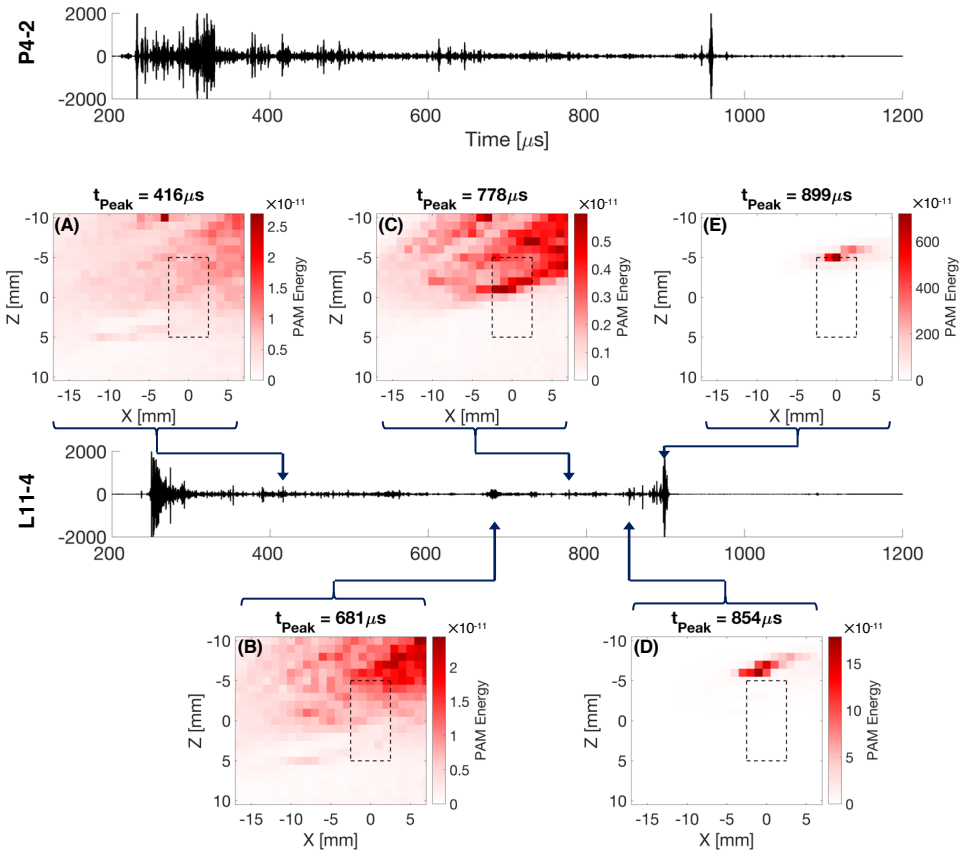


Figure 4.19: Representative PAM images generated at different peak times on the L11-4 for the 12th SW on stone 6. The RF lines collected on the central element of both probes are shown. The SW is coming from above and the dotted line represents the initial outline of the stone. Note that as the stone is impacted repeatedly by SWs its location will change.

(D) and (E) show activity located close to one another and it appears that the collapse-rebound cycle in for this SW was shorter than for the previous ones. The last event detected in (E) corresponds to a peak on the P4-2 that was detected with a time delay of 58 µs.

For the same stone, figure 4.20 shows the PAM images created during the 272nd SW. In general the pattern is similar to figure 4.19 except that some timings are shifted later in time. It can be seen that initially several locations of activity are pre-focally (panels A and B), before a cloud is detected (panel C). Afterwards, a similar signature to the 12th SW is detected, where the activity spatially overlaps on the surface of the stone.

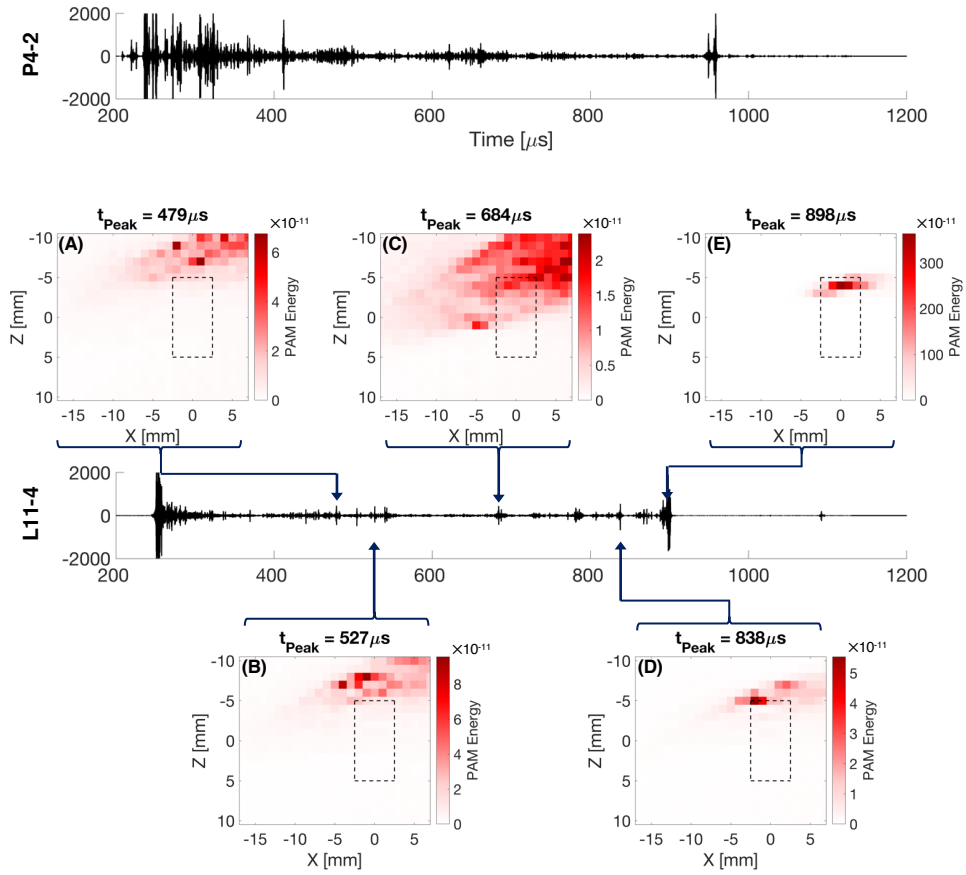


Figure 4.20: Representative PAM images generated at different peak times on the L11-4 for the 272nd SW on stone 6. The RF lines collected on the central element of both probes are shown. The SW is coming from above and the dotted line represents the initial outline of the stone. Note that as the stone is impacted repeatedly by SWs its location will change.

4.7 Discussion

This chapter demonstrated that using a B-mode probe and appropriate signal processing, it is possible to detecting cavitation during SWL. This heralds an advance in the state-of-the-art as current monitoring techniques based on x-ray and B-mode ultrasound have mostly remained unchanged for decades. The lack of adequate monitoring with current imaging likely means that patients are subject to more SWs than needed [12,104,105]. Because tissue damage increases with the SW dose [21–23,126] delivering excessive SWs likely leads to unwanted tissue damage. Cavitation is thought to be a primary driver of tissue damage and a contributor to stone fragmentation, and so, the spatio-temporal monitoring of cavitation in ex vivo kidneys and model stones by PAM provides a means to distinguish between harmful and beneficial cavitation.

All experiments were monitored using two arrays: an in-line P4-2 that could also be employed clinically and an out-of-line L11-4 that was used as a research tool. Using both probes, it was determined that the characteristic time of the major collapse increased between EL 5 to 9 from 486 µs to 700 µs. In vivo data from a pig kidney collected with a PCD using a Dornier HM3, an electrohydraulic lithotripter, have resulted in characteristic times of up to 440 µs [130]. However, the peak pressures of the lithotripter used here were higher than those created by a Dornier HM3 and the attenuation of the SW in vivo is higher than in the water tank, and thus the characteristic times are reasonable.

Applying SWs of a range of pressures to an ex vivo pig kidney has revealed a few considerations for the analysis of future experiments. It was shown that consistent peak detection times reveal reflections from within the tank and it may be that reflections result in PAM images where the source energy is spread over a large proportion of the map, on the L11-4 distal to the probe and on the P4-2 transversely

across the map. These observations suggest using an absorber on the water surface to minimise reflections. In vivo the body should absorb most of the wave although the bones and lungs will be an additional source of scattering. To minimise the number of events detected due to reflections, for the P4-2, a correlation between the size of the −6 dB region in PAM and the nature of the activity was determined, where cavitation was linked to events that covered less than 100 mm^2. Finally, it might have been the case that a slight misalignment of the L11-4 probe with the plane of the SW focus meant that some events were not captured due to the directivity of the elements in the array.

In vivo experiments have revealed that renal injury increases with the number of SWs [21, 126]. In this chapter, during an exposure to 3000 SWs, it was also determined that cavitation changes over the course of an experiment. Transitions were determined throughout all experiments, although their timing was varied for different kidneys. Within the first 1000 shocks, for example, late violent collapses are detected at all ELs suggesting that there might be some gas trapped in the kidney that cavitates or reflects the SW in the beginning of each experiment. However, only ex vivo kidneys should be subject to trapping large amounts of gas.

In addition to the number of SWs, the rate has also been shown to contribute to renal injury [22, 23]. The experiments in this chapter showed that in six kidneys exposed to rates of 1 Hz, 1.5 Hz, and 2 Hz, no difference in cavitation could be determined. The variability in the cavitation detection was mostly due to kidney-specific features rather than due to the SW rate. It may be the case that the quality and freshness of the ex vivo kidneys used in these experiments plays a role in some of the observed effects. The in vivo effects are further driven by the perfusion of kidneys that would cause blood to escape when cavitation damages vessels. The experiments in this chapter are thus limited by using ex vivo kidneys, where the effect of the rate on cavitation is limited.

Cavitation on the proximal surface of a model stone has previously been detected in vitro using a high speed camera [98]. Using a Dornier HM3, the characteristic time was in the order of 600 µs. The data, reported in this chapter, is consistent with the presence of bubble clusters on the surface and around the stone that resulted in major collapses at characteristic times of more than 650 µs. The characteristic time of stones that fragmented well was constant throughout the experiments. In some of the targets that did not fragment sufficiently, the characteristic time decreased during the course of the experiment. The shorter time could imply smaller bubble clusters, and thus, less fragmentation as a result of less violent cavitation. Previously, it has been determined that cavitation occurs on the proximal and distal surfaces of model stones [98]. Limitations in the resolution of PAM and the fact that the stone location could not be predicted after the the target was hit, prevent the accurate localisation of cavitation with respect to the stone in this chapter. To confirm the location of cavitation on model stone, high speed imaging could be used in the future.

Contrasting cavitation in tissue and cavitation on stones, it was determined that the cavitation in tissue had shorter characteristic times. As the SW reflects from the stone, the negative pressure in proximal to the stone increases, and thus, the cavitation is driven harder. Here, the difference appears to be approximately 100 µs. Furthermore, the more complex environment of a kidney resulted in more peaks that were detected throughout the experiments and required some consideration of reflected signals. It is expected that in vivo or in patients even more complex acoustic fields are encountered although the large absorption in vivo will also attenuate the SW. To create a methodology for the implementation of cavitation detection and localisation future experiments would need to address there complex fields and use perfused kidney models and natural stones. The challenge remains in differentiating between harmful and beneficial cavitation in the presence of complex fields.

4.8 Conclusions

In summary, cavitation produced by a clinical lithotripter was detected in ex vivo kidneys and in water around model stones using two ultrasound arrays and PAM. The PAM algorithm detected peaks in the signal first and then created maps from the signals in time windows that correspond to the peaks. Double-bang signatures were detected from which the characteristic time could be determined, which was found to increase from 486 µs to 700 µs at EL 5 to 9. Transitions in the characteristic time were furthermore detected during an exposure to 3000 SWs. Cavitation during stone fragmentation was monitored and longer characteristic times of up to 730 µs were recorded at EL 6. Challenges in developing a system to differentiate between the cavitation on stones and in tissue include the complex fields that would arise in vivo and in patients and the increased complexity of the presence of stones in the kidney. Furthermore, localisations are limited by a poor axial resolution of the in-line probe that appears to be worse than the resolution of B-mode. Nonetheless, it was shown that a B-mode probe and signal processing can be used to map cavitation during SWL allowing for a novel treatment option during treatment.

5 Conclusions

In this chapter, a discussion including a summary of findings and of the impact of the work is shown. Suggestions for future work and conclusions of the work presented in this thesis are also provided.

5.1 Discussion

The aim of this thesis was to investigate alternative monitoring options for SWL. The literature revealed a need to limit the SW dose that is delivered to each lithotripsy patient, and in particular to map and monitor cavitation that occurs throughout the procedure in the kidney parenchyma.

Chapter 1 reviewed the literature and demonstrated that SWL routinely results in tissue damage and that a correlation between the SW dose and injury exists. Furthermore, cavitation was identified as a driver of adverse effects and a contributor to stone comminution, motivating the development of novel monitoring tools in SWL. The rest of the chapter reviewed mapping of cavitation and stone tracking.

Chapter 2 addressed tissue injury by employing a large aperture, low frequency monitoring array that can be used to track stones in real-time. By tracking the stone, it is possible to gate the SW so that it is only triggered when the target is in

the focus, hence preventing SWs, which will only interact with the soft tissue. To image the stone with ultrasound, two variables should be considered: the frequency and the aperture of the imaging array. B-mode frequencies in the range of 3 MHz to 7 MHz provide greater resolution at the cost of increased attenuation and a small aperture of the probes limits the sensitivity to detect stones in the target region. Thus, the proposed array was constructed with 0.5 MHz transducers arranged on a circle of diameter 206 mm.

The tracking of a stone in a homogeneous water tank using a trilateration algorithm, resulted in an accuracy better than 2 mm in the axial direction and better than 4 mm in the lateral direction within ±15 mm from the focus of the lithotripter. These are sufficient to track a stone within the focal region of a lithotripter. Poor localisation occurred when the stone was more than 15 mm from the focus and an uncertainty metric was developed to identify when the localisation was not robust.

The focus of the work was then shifted from stone localisation to cavitation detection. PAM, a well established method to localise cavitation spatio-temporally by using conventional ultrasound probes in HIFU, was adapted to SWT and SWL. Since SWL treatment is routinely monitored using conventional diagnostic arrays, expanding PAM to SWL could provide a monitoring option to differentiate beneficial cavitation from harmful cavitation.

In chapter 3, PAM was modified to detect cavitation due to SWs by an SWT source in water with an ultrasound array. First, the acoustic field was measured using a PVDF needle hydrophone. The focal zone (8.0 mm by 1.8 mm at EL 20) was similar to the size reported by the manufacturer but the peak pressure (25.9 MPa at EL 20) was lower. The disparity in the pressure measurements is most likely due to using a needle hydrophone that is large compared to the size of the focus and will provide a measurement of the mean pressure over its sensitive diameter of <0.5 m m.

The modified version of PAM determined the location of cavitation in space and the characteristic time of bubbles that increased with the EL and the PRF to 288 µs at EL 20 and 8 Hz. The characteristic times were mostly in agreement with previous studies that used a comparable acoustic fields. It was also found that cavitation nuclei flowing through a tube in the SW focus would cavitate and that the characteristic time would increase with the EL. The dynamics were similar to degassed water flowing through a tube implying that the high pressures and low frequencies of the PiezoClast were above the cavitation threshold of both, impurities in the water and the submicron cavitation nuclei.

In chapter 4, PAM was used to detect and map cavitation in an ex vivo pig kidney and a model stone when targeted by a clinical lithotripter. Two conventional ultrasound probes were used to localise cavitation: an in-line P4-2 and an out-of-line L11-4. While the out-of-line probe was useful in mapping the cavitation with a better resolution, the in-line probe can be employed clinically. It was revealed that the characteristic time is affected by the EL and increases from EL 6 to 9 from 560 µs to 700 µs in tissue. The characteristic time can be determined using the clinically viable in-line probe and by correlating the characteristic time to renal injury, PAM could provide a method for real-time injury assessment throughout the treatment. Most current lithotripters are already equipped with the option of using an in-line probe, which would allow for cavitation mapping on most current systems.

The cavitation on the model stone was correlated to the fragmentation of the target subject to 300 SWs and appeared to have longer characteristic times than the cavitation in the kidney at an equivalent field. Longer characteristic times are consistent with an increased negative pressure proximal to the stone due to the reflected SW. Detecting that time difference, on a clinically viable probe using PAM, means that beneficial cavitation around the stone might be separable from the harmful cavitation in the soft tissue. Further, a monitoring option could thus allow for a feedback

system for stone fragmentation and renal injury detection.

The work in this thesis was limited to experiments in a water tanks, using ex vivo kidneys and model stones. The major unanswered question is with regards to performance in vivo or in patients. In chapter 4 using ex vivo kidneys already resulted in more complex acoustic fields and raised questions about differentiating cavitation from reflections. It can only be assumed that the complexity increases in a human body, where the soft tissue will abberate the field and the bones will reflect the signal. However, in vivo signals will also be attenuated more than in water, reducing the impact of reflections.

5.2 Future work

The major focus on any future work should lie in translating the tools developed in this thesis to a clinical setting to determine if stones can be tracked and cavitation can be mapped in patients durin SWL treatmeant.

For stone tracking an array that matches a clinical lithotripter needs to be made and a compiled code that runs in real-time should be developed for it. Further, the performance in tissue like media should be assessed. Studies should include regular stone motion due to breathing and random motion due to patient movement. Further, the work should determine if stones can be disintegrated using fewer SWs in a feasible treatment time.

By mapping and detecting cavitation, the impact of cavitation on the bioeffects of SWT can be determined. A clinical SWT study that assesses the efficacy of SWT could be linked to the level of cavitation during each treatment. It was shown that submicron cavitation nuclei cavitate when subject to a SW. Future work could show if SWs can propel these particles, for example, through the skin in transdermal drug

delivery applications. It was also found that there was no correlation between the characteristic time and the PRF when cavitation in a tube was detected. Given that the PRF had an effect when no tube was present, it would be interesting to investigate the effect of the flow rate on the cavitation at different SW rates.

With regards to cavitation detection a correlation between reduced tissue damage due to cavitation detection would need to be established. By using kidneys that are connected to a organ perfusion machine, two additional parameters can be introduced into the experiments. First, it is expected that cavitation will rupture the perfused blood vessels, and thus, more cavitation nuclei will be released into the kidney, which will trigger more cavitation. Second, in a perfused organ, the damage done due to the SWs can be assessed after the treatment.

Similarly, a clinical study can be used to monitor cavitation during a clinical SWL procedure and at different ELs and PRFs. The levels of detected cavitation could thus be correlated to stone fragmentation and adverse effects such as hematuria. Here it is important to determine if cavitation signatures with different characteristic times and different spatial locations are related to adverse effects. It is for example possible that larger bubbles, resulting in longer characteristic times, result in more tissue damage.

Real-time monitoring during lithotripsy is currently mostly achieved through x-ray imaging. Thus, another challenge would be the implementation of the work shown in this thesis onto current systems. To implement the work in chapter 2 and track stones during lithotripsy, an additional tracking system would need to be installed that would gate the SWs to be fired only when the stone is in the focal area. But the implementation of the work presented to detect cavitation would be more challenging. Although a difference between the characteristic time of cavitation in tissue and on a stone was reported (chapter 4), questions remain about whether the map should be overlayed with the existing B-mode system or whether the aim

should be a simple message identifying excess cavitation. Either way, more work is necessary to translate the work into clinical practice.

Finally, in the long-run, it would be necessary to draw together existing monitoring modalities and the ones presented in this work into one comprehensive monitoring strategy. Currently, most SWL procedures are monitored using x-ray and/or B-mode ultrasound. Ideally, novel monitoring options will eliminate the need for x-ray systems to remove the radiation risk and cavitation detection needs to be incorporated on existing B-mode systems.

5.3 Conclusions

SWL routinely results in renal injury such as hematuria and hematomas. The treatment is currently monitored using x-ray and/or B-mode ultrasound. These monitoring modalities can either not be operated continuously throughout the treatment (x-ray) and are not effective in limiting the SW dose that is a key contributor to renal injury. In this thesis, further updates to the state-of-the-art monitoring methods were considered, in particular, tracking the stone throughout the treatment using ultrasound and mapping the cavitation due to each SW. With regards to tracking, we have shown that a low-element count array mounted around the aperture of the SW source operating at 0.5 MHz can be used to track stones in real time. With regards to cavitation detection, it was shown that conventional B-mode probes and signal processing algorithms can be used to map the cavitation due to a SW and determine the characteristic time of bubbles.

However, a few challenges still have to be overcome before the monitoring advancements shown in this thesis can be implemented clinically. The environments used to test the algorithms in this work are simple and there is reason to believe that com-

plex tissue layers will affect the functionality of the algorithms. For example, using an ex vivo kidney and ultrasound probes at realistic diagnostic distances already affected the ability to see and localise cavitation compared to experiments in a clean water tank. Nonetheless, the combination of both findings, a large aperture array to track the target and PAM to monitor cavitation, provides an opportunity for the future development of monitoring methods to limit the SW dose that is delivered to each patient, and thus, reduce renal injury as a routine outcome of the treatment.

Bibliography

[1] C. Chaussy, W. Brendel, and E. Schmiedt, "Extracorporeally induced destruction of kidney stones by shock waves," Lancet **316**(8207), 1265–1268 (1980).

[2] J. C. Williams Jr., B. R. Matlaga, S. C. Kim, M. E. Jackson, A. J. Sommer, J. A. McAteer, J. E. Lingeman, and A. P. Evan, "Calcium oxalate calculi found attached to the renal papilla: Preliminary evidence for early mechanisms in stone formation," J Endourol **20**(11), 885–890 (2006).

[3] M. S. Pearle, E. A. Calhoun, and G. C. Curhan, "Urologic diseases in America project: urolithiasis," The Journal of Urology **173**(3), 848–857 (2005).

[4] K. K. Stamatelou, M. E. Francis, C. A. Jones, L. M. Nyberg, and G. C. Curhan, "Time trends in reported prevalence of kidney stones in the United States: 1976–1994," Kidney International **63**(5), 1817–1823 (2003).

[5] B. W. Turney, J. M. Reynard, J. G. Noble, and S. R. Keoghane, "Trends in urological stone disease," British Journal of Urology **109**(7), 1082–1087 (2012).

[6] C. Chaussy, E. Schmiedt, D. Jocham, W. Brendel, B. Forssmann, and V. Walther, "First clinical experience with extracorporeally induced destruction of kidney stones by shock waves," The Journal of Urology **127**(3), 417–420 (1982).

[7] C. Chaussy and E. Schmiedt, "Shock wave treatment for stones in the upper urinary tract," The Urologic Clinics of North America **10**(4), 743–750 (1983).

[8] S. A. V. Holmes and H. N. Whitfield, "The current status of lithotripsy," British Journal of Urology **68**(4), 337–344 (1991).

[9] B. Finlayson and D. Ackermann, "Overview of surgical treatment of urolithiasis with special reference to lithotripsy," The Journal of Urology **141**(3), 778–779 (1989).

[10] J. Skenazy, B. Ercole, C. Lee, S. Best, E. Fallon, and M. Monga, "Nephrolithiasis: "scope," shock or scalpel?," The Journal of Endourology **19**(1), 45–49 (2005).

[11] T. G. Leighton and R. O. Cleveland, "Lithotripsy," in *Proc of the IMechE, Part H, J Eng Med* (2010), Vol. 224, pp. 317–342.

[12] P. M. Knapp, T. B. Kulb, J. E. Lingeman, D. M. Newman, J. H. Mertz, P. G. Mosbaugh, and R. E. Steele, "Extracorporeal shock wave lithotripsy-induced perirenal hematomas," The Journal of Urology **139**(4), 700 (1988).

[13] J. V. Kaude, C. M. Williams, M. R. Millner, K. N. Scott, and B. Finlayson, "Renal morphology and function immediately after extracorporeal shock-wave lithotripsy," The American Journal of Roentgenology **145**(2), 305–313 (1985).

[14] J. A. McAteer and A. P. Evan, "The acute and long-term adverse effects of shock wave lithotripsy," in *Seminars in Nephrology* (2008), Vol. 28, pp. 200–213.

[15] A. K. Tuteja, J. P. Pulliam, T. H. Lehman, and L. W. Elzinga, "Anuric renal failure from massive bilateral renal hematoma following extracorporeal shock wave lithotripsy," Urology **50**(4), 606–608 (1997).

[16] B. Lipski, J. Miller, G. Rigaud, G. Stack, and C. Marsh, "Acute renal failure from a subcapsular hematoma in a solitary kidney: an unusual complication of extracorporeal shock wave lithotripsy," The Journal of Urology **157**(6), 2245 (1997).

[17] G. Janetschek, F. Frauscher, R. Knapp, G. Hofle, R. Peschel, and G. Bartsch, "New onset hypertension after extracorporeal shock wave lithotripsy: age related incidence and prediction by intrarenal resistive index," The Journal of Urology **158**(2), 346–351 (1997).

[18] N. Mandel, I. Mandel, K. Fryjoff, T. Rejniak, and G. Mandel, "Conversion of calcium oxalate to calcium phosphate with recurrent stone episodes," The Journal of Urology **169**(6), 2026–2029 (2003).

[19] R. Newman, R. Hackett, D. Senior, K. Brock, J. Feldman, J. Sosnowski, and B. Finlayson, "Pathologic effects of ESWL on canine renal tissue," Urology **29**(2), 194–200 (1987).

[20] R. Thomas, J. Roberts, B. Sloane, and B. Kaack, "Effect of extracorporeal shock wave lithotripsy on renal function," The Journal of Endourology **2**(2), 141–144 (1988).

[21] L. R. Willis, A. P. Evan, B. a. Connors, Y. Shao, P. M. Blomgren, J. H. Pratt, N. S. Fineberg, and J. E. Lingeman, "Shockwave lithotripsy: dose-related effects on renal structure, hemodynamics, and tubular function.," Journal of endourology / Endourological Society **19**(1), 90–101 (2005).

[22] M. Delius, M. Jordan, H. Eizenhoefer, E. Marlinghaus, G. Heine, H.-G. Liebich, and W. Brendel, "Biological effects of shock waves: kidney haemorrhage by shock waves in dogs—administration rate dependence," Ultrasound in Medicine & Biology **14**(8), 689–694 (1988).

[23] A. P. Evan, J. A. McAteer, B. A. Connors, P. M. Blomgren, and J. E. Lingeman, "Renal injury during shock wave lithotripsy is significantly reduced by slowing the rate of shock wave delivery," British Journal of Urology **100**(3), 624–628 (2007).

[24] B. A. Connors, A. P. Evan, L. R. Willis, P. M. Blomgren, J. E. Lingeman, and N. S. Fineberg, "The effect of discharge voltage on renal injury and impairment caused by lithotripsy in the pig.," Journal of the American Society of Nephrology **11**(2), 310–8 (2000).

[25] R. O. Cleveland, R. Anglade, and R. K. Babayan, "Effect of stone motion on in vitro comminution efficiency of Storz Modulith SLX," The Journal of Endourology **18**(7), 629–633 (2004).

[26] L. R. Willis, A. P. Evan, and J. E. Lingeman, "The impact of high-dose lithotripsy on renal function," Contemporary Urology **11**(12), 45–50 (1999).

[27] J. A. Ogden, A. Tóth-Kischkat, and R. Schultheiss, "Principles of Shock Wave Therapy," Clinical Orthopaedics and Related Research **387**, 8–17 (2001).

[28] J. A. Ogden, R. Alvarez, R. Levitt, G. L. Cross, and M. Marlow, "Shock wave therapy for chronic proximal plantar fasciitis," Clinical Orthopaedics and Related Research **387**, 47–59 (2001).

[29] L. S. Weil, T. S. Roukis, and A. H. Borrelli, "Extracorporeal shock wave therapy for the treatment of chronic plantar fasciitis: indications, protocol, intermediate results, and a comparison of results to fasciotomy," The Journal of Foot & Ankle Surgery **41**(3), 166–172 (2002).

[30] J. D. Rompe, C. Schoellner, and B. Nafe, "Evaluation of low-energy extracorporeal shockwave application for treatment of chronic plantar fasciitis," The Journal of Bone & Joint Surgery **84**(3), 335–341 (2002).

[31] M. Hanada, M. Takahashi, and Y. Matsuyama, "The effect of extracorporeal shock wave therapy for the treatment of plantar fasciitis in regard to middle-aged patients' activity level and pain localization," Shock Waves (2017).

[32] J. D. Rompe, R. Bürger, C. Hopf, and P. Eysel, "Shoulder function after extracorporal shock wave therapy for calcific tendinitis," The Journal of Shoulder & Elbow Surgery **7**(5), 505–509 (1998).

[33] M. Loew, W. Daecke, D. Kusnierczak, M. Rahmanzadeh, and V. Ewerbeck, "Shock-wave therapy is effective for chronic calcifying tendinitis of the shoulder," The Journal of Bone & Joint Surgery **81**(5), 863–867 (1999).

[34] J. D. Rompe, J. P. Furia, and N. Maffulli, "Eccentric loading compared with shock wave treatment for chronic insertional Achilles tendinopathy," The Journal of Bone & Joint Surgery **90**(1), 52–61 (2008).

[35] J. D. Rompe, J. P. Furia, and N. Maffulli, "Eccentric Loading Versus Eccentric Loading Plus Shock-Wave Treatment for Midportion Achilles Tendinopathy A Randomized Controlled Trial," The American Journal of Sports Medicine **37**(3), 463–470 (2009).

[36] J. P. Furia, "High-energy extracorporeal shock wave therapy as a treatment for insertional Achilles tendinopathy," The American Journal of Sports Medicine **34**(5), 733–740 (2006).

[37] R. Zimmermann, A. Cumpanas, L. Hoeltl, G. Janetschek, A. Stenzl, and F. Miclea, "Extracorporeal shock-wave therapy for treating chronic pelvic pain syndrome: a feasibility study and the first clinical results," British Journal of Urology **102**(8), 976–980 (2008).

[38] R. Zimmermann, A. Cumpanas, F. Miclea, and G. Janetschek, "Extracorporeal shock wave therapy for the treatment of chronic pelvic pain syndrome in males: a randomised, double-blind, placebo-controlled study," European Urology **56**(3), 418–424 (2009).

[39] M. Mathers, S. Degener, S. Roth, and T. Klotz, "Is there evidence for ESWT therpy in men with chronic nonbacterial prostititis/chronic pelvic syndrome? Preliminary results of a controlled study," The Journal of Urology **185**(4), 1341 (2011).

[40] X. Y. Zeng, C. Liang, and Z. Q. Ye, "Extracorporeal shock wave treatment for non-inflammatory chronic pelvic pain syndrome: a prospective, randomized and sham-controlled study," Chinese Medical Journal **125**(1), 114–118 (2012).

[41] B. Vahdatpour, F. Alizadeh, A. Moayednia, M. Emadi, M. H. Khorami, and S. Haghdani, "Efficacy of extracorporeal shock wave therapy for the treatment of chronic pelvic pain syndrome: a randomized, controlled trial," International Scholarly Research Notices Urology **2013**, 972601 (2013).

[42] A. Moayednia, S. Haghdani, S. Khosrawi, E. Yousefi, and B. Vahdatpour, "Long-term effect of extracorporeal shock wave therapy on the treatment of chronic pelvic pain syndrome due to non bacterial prostatitis," Journal of Research in Medical Sciences **19**(4), 293–296 (2014).

[43] R. Buchbinder, R. Ptasznik, J. Gordon, J. Buchanan, V. Prabaharan, and A. Forbes, "Ultrasound-guided extracorporeal shock wave therapy for plantar fasciitis: a randomized controlled trial," JAMA **288**, 1364–1372 (2002).

[44] M. Haake, I. R. König, T. Decker, C. Riedel, M. Buch, H.-H. Müller, M. Vogel, V. Auersperg, O. Maier-Boerries, and A. Betthäuser, "Extracorporeal shock wave therapy in the treatment of lateral epicondylitis," The Journal of Bone & Joint Surgery **84**(11), 1982–1991 (2002).

[45] J. Zwerver, F. Hartgens, E. Verhagen, H. Van Der Worp, I. Van Den Akker-Scheek, and R. L. Diercks, "No effect of extracorporeal shockwave therapy on patellar tendinopathy in jumping athletes during the competitive season: A randomized clinical trial," American Journal of Sports Medicine **39**(6), 1191–1199 (2011).

[46] A. Kolk, K. G. Auw Yang, R. Tamminga, and H. Van Der Hoeven, "Radial extracorporeal shock-wave therapy in patients with chronic rotator cuff tendinitis," Bone and Joint Journal **95 B**(11), 1521–1526 (2013).

[47] K. Engebretsen, M. Grotle, E. Bautz-Holter, L. Sandvik, N. G. Juel, O. M. Ekeberg, and J. I. Brox, "Radial extracorporeal shockwave treatment compared with supervised exercises in patients with subacromial pain syndrome: single blind randomised study," BMJ **339**(August), b3360–b3360 (2009).

[48] J. D. Rompe, A. Cacchio, L. Weil, J. P. Furia, J. Haist, V. Reiners, C. Schmitz, and N. Maffulli, "Plantar fascia-specific stretching versus radial shock-wave therapy as initial treatment of plantar fasciopathy," Journal of Bone and Joint Surgery **92**(15), 2514–2522 (2010).

[49] C. Schmitz, N. B. Császár, S. Milz, M. Schieker, N. Maffulli, J. D. Rompe, and J. P. Furia, "Efficacy and safety of extracorporeal shock wave therapy for orthopedic conditions: A systematic review on studies listed in the PEDro database," British Medical Bulletin **116**(1), 115–138 (2015).

[50] R. O. Cleveland and J. A. McAteer, "The physics of shock wave lithotripsy," in *Smith's Textbook of Endourology*, edited by Arthur D. Smith, G. Preminger, G. Badlani, and L. R. Kavoussi, Vol. 1 & 2, 3rd ed. (Wiley-Blackwell, Hoboken, NJ, 2012), pp. 527–558.

[51] S. Mariotto, E. Cavalieri, E. Amelio, A. R. Ciampa, A. C. De Prati, E. Marlinghaus, S. Russo, and H. Suzuki, "Extracorporeal shock waves: From lithotripsy to anti-inflammatory action by NO production," Nitric Oxide - Biology and Chemistry **12**(2), 89–96 (2005).

[52] C.-J. Wang, H.-Y. Huang, and C.-H. Pai, "Shock wave-enhanced neovascularization at the tendon-bone junction: An experiment in dogs," The Journal of Foot and Ankle Surgery **41**(1), 16–22 (2002).

[53] C. J. Wang, F. S. Wang, K. D. Yang, L. H. Weng, C. C. Hsu, C. S. Huang, and L. C. Yang, "Shock wave therapy induces neovascularization at the tendon-bone junction. A study in rabbits," Journal of Orthopaedic Research **21**(6), 984–989 (2003).

[54] K. Ito, Y. Fukumoto, and H. Shimokawa, "Extracorporeal Shock Wave Therapy as a New and Non-invasive Angiogenic Strategy," The Tohoku Journal of Experimental Medicine **219**(1), 1–9 (2009).

[55] A. J. Coleman and J. E. Saunders, "A survey of the acoustic output of commercial extracorporeal shock wave lithotripters," Ultrasound in Medicine & Biology **15**(3), 213–227 (1989).

[56] D. T. Blackstock, M. F. Hamilton, and A. D. Pierce, "Progressive waves in lossless and lossy fluids," Nonlinear acoustics 65–150 (1998).

[57] T. A. Flam, M. Bourlion, N. Thiounn, F. Saporta, R. Chiche, P. Dancer, M. Zerbib, and B. Debré, "Electroconductive lithotripsy: principles, experimental data, and first clinical results of the Sonolith 4000," The Journal of Endourology **8**(4), 249 (1994).

[58] R. O. Cleveland, P. V. Chitnis, B. Gerbus, and J. McAteer, "An in vitro comparison of open-cage and encapsulated electrodes in shock wave lithotripsy (SWL)," European Urology Supplements **3**(2), 235 (2004).

[59] D. Cathignol, J. L. Mestas, P. Dancer, M. Bourlion, F. Gomez, and P. Lenz, "Improvement of the reproducibility in electrohydraulic generators by using conducting liquid (medical US lithotripsy)," in *IEEE 1990 Ultrasonics Symposium Proceedings (Cat. No.90CH2938-9)* (1990), pp. 1641–4 vol.3.

[60] J. Pleiner, R. Crevenna, H. Langenberger, M. Keilani, M. Nuhr, F. Kainberger, M. Wolzt, G. Wiesinger, and M. Quittan, "Extracorporeal Shockwave treatment is effective in calcific tendonitis of the shoulder. A randomized controlled trial," Wiener Klinische Wochenschrift **116**(15-16), 536–541 (2004).

[61] D. S. Malay, M. M. Pressman, A. Assili, J. T. Kline, S. York, B. Buren, E. R. Heyman, P. Borowsky, and C. LeMay, "Extracorporeal Shockwave Therapy Versus Placebo for the Treatment of Chronic Proximal Plantar Fasciitis: Results of a Randomized, Placebo-Controlled, Double-Blinded, Multicenter Intervention Trial," Journal of Foot and Ankle Surgery **45**(4), 196–210 (2006).

[62] J. A. Ogden, R. G. Alvarez, R. L. Levitt, J. E. Johnson, and M. E. Marlow, "Electrohydraulic high-energy shock-wave treatment for chronic plantar fasciitis," Journal of Bone and Joint Surgery - Series A **86**(10), 2216–2228 (2004).

[63] Y. A. Radwan, A. M. R. Mansour, and W. S. Badawy, "Resistant plantar fasciopathy: Shock wave versus endoscopic plantar fascial release," in *International Orthopaedics* (2012), Vol. 36, pp. 2147–2156.

[64] W. Folberth, G. Köhler, A. Rohwedder, and E. Matura, "Pressure distribution and energy flow in the focal region of two different electromagnetic shock wave sources," The Journal of Stone Disease **4**(1), 1–7 (1992).

[65] J. J. Rassweiler, G. G. Tailly, and C. Chaussy, "Progress in lithotriptor technology," European Association Urology Update Series **3**(1), 17–36 (2005).

[66] J. D. Rompe, J. Decking, C. Schoellner, and B. Nafe, "Shock Wave Application for Chronic Plantar Fasciitis in Running Athletes: A Prospective, Randomized, Placebo-Controlled Trial," The American Journal of Sports Medicine **31**(2), 268–275 (2003).

[67] J. D. Rompe, J. Decking, C. Schoellner, and C. Theis, "Repetitive Low-Energy Shock Wave Treatment for Chronic Lateral Epicondylitis in Tennis Players," The American Journal of Sports Medicine **32**(3), 734–743 (2004).

[68] M. Delius, A. Mueller, A. Vogel, and W. Brendel, *Extracorporeal shock waves: properties and principles of generation* (Year Book Medical Publisher, Chicago, 1989), pp. 9–16.

[69] H. W. Liang, T. G. Wang, W. S. Chen, and S. M. Hou, "Thinner plantar fascia predicts decreased pain after extracorporeal shock wave therapy," Clinical Orthopaedics and Related Research (460), 219–225 (2007).

[70] S. Rasmussen, M. Christensen, I. Mathiesen, and O. Simonson, "Shockwave therapy for chronic Achilles tendinopathy: A double-blind, randomized clinical trial of efficacy," Acta Orthopaedica **79**(2), 249–256 (2008).

[71] R. O. Cleveland, P. V. Chitnis, and S. R. McClure, "Acoustic field of a ballistic shock wave therapy device," Ultrasound in Medicine & Biology **33**(8), 1327–1335 (2007).

[72] A. Cacchio, J. D. Rompe, J. P. Furia, P. Susi, V. Santilli, and F. De Paulis, "Shockwave therapy for the treatment of chronic proximal hamstring tendinopathy in professional athletes," American Journal of Sports Medicine **39**(1), 146–153 (2011).

[73] C. Perez, H. Chen, T. J. Matula, M. Karzova, and V. A. Khokhlova, "Acoustic field characterization of the Duolith: measurements and modeling of a clinical shock wave therapy device," The Journal of the Acoustical Society of America **134**(2), 1663–1674 (2013).

[74] A. F. Bierkens, R. M. Maes, A. J. M. Hendrikx, A. F. Erdos, J. D. M. De Vries, and F. M. J. Debruyne, "The use of local anesthesia in second generation extracorporeal shock wave lithotripsy: Eutectic mixture of local anesthetics," Journal of Urology **146**(2), 287–289 (1991).

[75] K. R. Anderson, D. W. Keetch, D. M. Albala, P. S. Chandhoke, B. L. McClennan, and R. V. Clayman, "Optimal therapy for the distal ureteral stone: extracorporeal shock wave lithotripsy versus ureteroscopy.," The Journal of urology **152**(1), 62–65 (1994).

[76] J. Rassweiler, A. Westhauser, P. Bub, and F. Eisenberger, "Second-generation lithotripters: a comparative study," Journal of Endourology **2**(2), 193–204 (1988).

[77] J. Rassweiler, T. O. Henkel, K. U. Köhrmann, D. Potempa, K. P. Jünemann, and P. Alken, "Lithotripter technology: present and future," Journal of endourology **6**(1), 1–13 (1992).

[78] J. Rassweiler, R. Gumpinger, R. Mayer, H. Kohl, A. Schmidt, and F. Eisenberger, "Extracorporeal piezoelectric lithotripsy using the Wolf-lithotriptor versus low energy lithotripsy with the modified Dornier HM-3: a cooperative study," World Journal of Urology **5**(4), 218–224 (1987).

[79] Y. A. Pishchalnikov, J. S. Neucks, R. J. Von Der Haar, I. V. Pishchalnikova, J. C. Williams, and J. A. McAteer, "Air pockets trapped during routine coupling in dry head lithotripsy can significantly decrease the delivery of shock wave energy," The Journal of Urology **176**(6), 2706–2710 (2006).

[80] A. Jain, T. K. Shah, and F. X. Keeley, "Effect of air bubbles in the coupling medium on efficacy of extracorporeal shock wave lithotripsy," European urology **51**(6), 1680–1687 (2007).

[81] A. Buizza, T. Dell'Aquila, P. Giribona, and C. Spagno, "The performance of different pressure pulse generators for extracorporeal lithotripsy: A comparison based on commercial lithotripters for kidney stones," Ultrasound in Medicine & Biology **21**(2), 259–272 (1995).

[82] J. M. Teichman, a. J. Portis, P. P. Cecconi, W. L. Bub, R. C. Endicott, B. Denes, M. S. Pearle, and R. V. Clayman, "In vitro comparison of shock wave lithotripsy machines.," The Journal of urology **164**(October), 1259–1264 (2000).

[83] M. D. Sorensen, M. R. Bailey, A. R. Shah, R. S. Hsi, M. Paun, and J. D. Harper, "Quantitative assessment of shockwave lithotripsy accuracy and the effect of respiratory motion," The Journal of Endourology **26**(8), 1070–1074 (2012).

[84] P. Lubock, "The physics and mechanics of lithotripters," Digestive Diseases and Sciences **34**(7), 999–1005 (1989).

[85] W. Lu, B. W. Cunitz, O. A. Sapozhnikov, P. J. Kaczkowski, J. C. Kucewicz, N. R. Owen, M. R. Bailey, and L. A. Crum, "Investigation of the effect of signal amplitude on twinkling artifact," The Journal of the Acoustical Society of America **129**(4), 2376 (2011).

[86] M. D. Sorensen, J. D. Harper, R. S. Hsi, A. R. Shah, M. K. Dighe, S. J. Carter, M. Moshiri, M. Paun, W. Lu, and M. R. Bailey, "B-mode ultrasound versus color Doppler twinkling artifact in detecting kidney stones," The Journal of Endourology **27**(2), 149–153 (2013).

[87] A. D. Maxwell, B. W. Cunitz, W. Kreider, O. A. Sapozhnikov, R. S. Hsi, J. D. Harper, M. R. Bailey, and M. D. Sorensen, "Fragmentation of Urinary Calculi In Vitro by Burst Wave Lithotripsy," Journal of Urology **193**(1), 338–344 (2015).

[88] A. Maxwell, B. Cunitz, W. Kreider, M. R. Bailey, O. Sapozhnikov, F. Lee, M. Sorensen, and J. Harper, "Pd42-02 A Preclinical Image-guided Therapy System For Burst Wave Lithotripsy," The Journal of Urology **193**(4), e886 (2015).

[89] R. Agarwal and V. R. Singh, "A comparative study of fracture strength, ultrasonic properties and chemical constituents of kidney stones," Ultrasonics **29**(1), 89–90 (1991).

[90] N. P. Cohen and H. N. Whitfield, "Mechanical testing of urinary calculi," The World Journal of Urology **11**(1), 13–18 (1993).

[91] P. E. I. Zhong and G. M. Preminger, "Mechanisms of differing stone fragility in extracorporeal shockwave lithotripsy," Journal of Endourology **8**(4), 263–268 (1994).

[92] D. Heimbach, R. Munver, P. Zhong, J. Jacobs, A. Hesse, S. C. Müller, and G. M. Preminger, "Acoustic and mechanical properties of artificial stones in comparison to natural kidney stones," Journal of Urology **163**(2), 537–544 (2000).

[93] W. Eisenmenger, "The mechanisms of stone fragmentation in ESWL," Ultrasound in Medicine & Biology **27**(5), 683–693 (2001).

[94] W. Eisenmenger, X. X. Du, C. Tang, S. Zhao, Y. Wang, F. Rong, D. Dai, M. Guan, and A. Qi, "The first clinical results of "wide-focus and low-pressure" ESWL," Ultrasound in Medicine & Biology **28**(6), 769–774 (2002).

[95] T. G. Leighton, *The Acoustic Bubble* (Academic Press, London, UK, 1997).

[96] A. J. Coleman, J. E. Saunders, L. A. Crum, and M. Dyson, "Acoustic cavitation generated by an extracorporeal shockwave lithotripter," Ultrasound in Medicine & Biology **13**(2), 69–76 (1987).

[97] L. A. Crum, "Cavitation microjets as a contributory mechanism for renal calculi disintegration in ESWL," The Journal of Urology **140**(6), 1587–1590 (1988).

[98] Y. A. Pishchalnikov, O. A. Sapozhnikov, M. R. Bailey, J. C. Williams, R. O. Cleveland, T. Colonius, L. A. Crum, A. P. Evan, and J. A. McAteer, "Cavitation bubble cluster activity in the breakage of kidney stones by lithotripter shockwaves," The Journal of Endourology **17**(7), 435–446 (2003).

[99] R. O. Cleveland and O. A. Sapozhnikov, "Modeling elastic wave propagation in kidney stones with application to shock wave lithotripsy," The Journal of the Acoustical Society of America **118**(4), 2667–2676 (2005).

[100] E. T. Sylven, S. Agarwal, C. L. Briant, and R. O. Cleveland, "High strain rate testing of kidney stones," The Journal of Materials Science Medicine **15**(5), 613–617 (2004).

[101] O. A. Sapozhnikov, A. D. Maxwell, B. MacConaghy, and M. R. Bailey, "A mechanistic analysis of stone fracture in lithotripsy," The Journal of the Acoustical Society of America **121**(2), 1190–1202 (2007).

[102] S. M. Gracewski, G. Dahake, Z. Ding, S. J. Burns, and E. C. Everbach, "Internal stress wave measurements in solids subjected to lithotripter pulses," The Journal of the Acoustical Society of America **94**(2), 652–661 (1993).

[103] X. Xi and P. Zhong, "Dynamic photoelastic study of the transient stress field in solids during shock wave lithotripsy," The Journal of the Acoustical Society of America **109**(3), 1226–1239 (2001).

[104] B. R. Baumgartner, K. W. Dickey, S. S. Ambrose, K. N. Walton, R. C. Nelson, and M. E. Bernardino, "Kidney changes after extracorporeal shock wave lithotripsy: appearance on MR imaging," Radiology **163**(2), 531–534 (1987).

[105] J. I. Rubin, P. H. Arger, H. M. Pollack, M. P. Banner, B. G. Coleman, M. C. Mintz, and K. N. Van Arsdalen, "Kidney changes after extracorporeal shock wave lithotripsy: CT evaluation," Radiology **162**(1), 21–24 (1987).

[106] J. E. Lingeman and J. R. Newmark, "Adverse bioeffects of shock-wave lithotripsy," in *Kidney Stones: Medical and Surgical Management*, edited by F. L. Coe, M. J. Favus, C. Y. C. Pak, J. H. Parks, and G. M. Preminger (Lippincott-Raven, Philadelphia, PA, 1996), pp. 605–614.

[107] B. R. Matlaga and J. E. Lingeman, "Surgical Management of Upper Urinary Tract Calculi," in *Campbell-Walsh Urology*, 10th ed. (Saunders Elsevier, Philadelphia, PA, 2011), Chap. 1367 – 14.

[108] A. P. Evan and J. A. McAteer, "Q-effects of shock wave lithotripsy," in *Kidney Stones: Medical and Surgical Management*, edited by F. L. Coe, M. J. Favus, C. Y. C. Pak, J. H. Parks, and G. M. Preminger (Lippincott-Raven, Philadelphia, PA, 1996), pp. 549–570.

[109] L. R. Willis, A. P. Evan, B. A. Connors, R. K. Handa, P. M. Blomgren, and J. E. Lingeman, "Prevention of lithotripsy-induced renal injury by pretreating kidneys with low-energy shock waves," The Journal of the American Society of Nephrology **17**(3), 663–673 (2006).

[110] C. Chaussy and E. Schmiedt, "Extracorporeal shock wave lithotripsy (ESWL) for kidney stones. An alternative to surgery?," Urologic Radiology **6**(1), 80–87 (1984).

[111] V. Krishnamurthi and S. B. Streem, "Long-term radiographic and functional outcome of extracorporeal shock wave lithotripsy induced perirenal hematomas," The Journal of Urology **154**(5), 1673–1675 (1995).

[112] R. Knapp, F. Frauscher, G. Helweg, W. Judmaier, H. Strasser, G. Bartsch, and D. Zur Nedden, "Blood pressure changes after extracorporeal shock wave nephrolithotripsy: prediction by intrarenal resistive index," European Radiology **6**(5), 665–669 (1996).

[113] B. S. I. Montgomery, R. S. Cole, E. L. H. Palfrey, and K. E. D. Shuttleworth, "Does extracorporeal shockwave lithotripsy cause hypertension?," British Journal of Urology **64**(6), 567–571 (1989).

[114] R. Knapp, F. Frauscher, G. Helweg, D. Zur Nedden, H. Strasser, G. Janetschek, and G. Bartsch, "Age-related changes in resistive index following extracorporeal shock wave lithotripsy," The Journal of Urology **154**(3), 955–958 (1995).

[115] J. H. Parks, E. M. Worcester, F. L. Coe, A. P. Evan, and J. E. Lingeman, "Clinical implications of abundant calcium phosphatein routinely analyzed kidney stones," Kidney International **66**(2), 777–785 (2004).

[116] P. Zhong and Y. Zhou, "Suppression of large intraluminal bubble expansion in shock wave lithotripsy without compromising stone comminution: Methodology and in vitro experiments," The Journal of the Acoustical Society of America **110**(6), 3283–3291 (2001).

[117] J. C. Williams, J. F. Woodward, M. A. Stonehill, A. P. Evan, and J. A. McAteer, "Cell damage by lithotripter shock waves at high pressure to preclude cavitation," Ultrasound in Medicine & Biology **25**(9), 1445–1449 (1999).

[118] H. Chen, W. Kreider, A. A. Brayman, M. R. Bailey, and T. J. Matula, "Blood vessel deformations on microsecond time scales by ultrasonic cavitation," Physical Review Letters **106**(3), 34301 (2011).

[119] T. G. Leighton, F. Fedele, A. J. Coleman, C. McCarthy, S. Ryves, A. M. Hurrell, A. De Stefano, P. R. White, J. C. Williams, and A. P. Evan, "Clinical studies of real-time monitoring of lithotripter performance using passive acoustic sensors," in *AIP Conf Proc of Ann Int Urolithiasis Research Symposium*, Indianapolis, IN (2008), Vol. 1049, p. 256.

[120] P. Zhong, I. Cioanta, S. Zhu, F. H. Cocks, and G. M. Preminger, "Effects of tissue constraint on shock wave-induced bubble expansion in vivo," The Journal of the Acoustical Society of America **104**(5), 3126–3129 (1998).

[121] P. Zhong, Y. Zhou, and S. Zhu, "Dynamics of bubble oscillation in constrained media and mechanisms of vessel rupture in SWL," Ultrasound in Medicine & Biology **27**(1), 119–134 (2001).

[122] A. J. Coleman, M. J. Choi, and J. E. Saunders, "Detection of acoustic emission from cavitation in tissue during clinical extracorporeal lithotripsy," Ultrasound in Medicine & Biology **22**(8), 1079–1087 (1996).

[123] O. Sapozhnikov, M. R. Bailey, L. A. Crum, N. Miller, R. O. Cleveland, Y. Pishchalnikov, I. V. Pishchalnikova, J. A. McAteer, B. A. Connors, and P. M. Blomgren, "Ultrasound-guided localized detection of cavitation during, lithotripsy in pig kidney in vivo," in *Proc of IEEE Ultrasonics Symposium*, Atlanta, GA (2001), Vol. 2, pp. 1347–1350.

[124] M. Lokhandwalla and B. Sturtevant, "Mechanical haemolysis in shock wave lithotripsy (SWL): I. Analysis of cell deformation due to SWL flow-fields," Physics in Medicine and Biology **46**(2), 413 (2001).

[125] M. Lokhandwalla, J. A. McAteer, J. C. Williams, and B. Sturtevant, "Mechanical haemolysis in shock wave lithotripsy (SWL): II. In vitro cell lysis due to shear," Physics in Medicine and Biology **46**(4), 1245 (2001).

[126] M. Delius, G. Enders, Z. Xuan, H.-G. Liebich, and W. Brendel, "Biological effects of shock waves: kidney damage by shock waves in dogs—dose dependence," Ultrasound in Medicine & Biology **14**(2), 117–122 (1988).

[127] C. C. Church, "A theoretical study of cavitation generated by an extracorporeal shock wave lithotripter," The Journal of the Acoustical Society of America **86**(1), 215–227 (1989).

[128] R. O. Cleveland, O. A. Sapozhnikov, M. R. Bailey, and L. A. Crum, "A dual passive cavitation detector for localized detection of lithotripsy-induced cavitation in vitro," The Journal of the Acoustical Society of America **107**(3), 1745–1758 (2000).

[129] A. J. Coleman, M. J. Choi, J. E. Saunders, and T. G. Leighton, "Acoustic emission and sonoluminescence due to cavitation at the beam focus of an electrohydraulic shock wave lithotripter," Ultrasound in Medicine and Biology **18**(3), 267–281 (1992).

[130] M. R. Bailey, Y. A. Pishchalnikov, O. A. Sapozhnikov, R. O. Cleveland, J. A. McAteer, N. A. Miller, I. V. Pishchalnikova, B. A. Connors, L. A. Crum, and A. P. Evan, "Cavitation detection during shock-wave lithotripsy," Ultrasound in Medicine & Biology **31**(9), 1245–1256 (2005).

[131] M. Gyöngy and C.-C. Coussios, "Passive spatial mapping of inertial cavitation during HIFU exposure," IEEE Transactions on Biomedical Engineering **57**(1), 48–56 (2010).

[132] G. C. Carter, "Time Delay Estimation for Passive Sonar Signal Processing," IEEE Transactions on Acoustics, Speech, and Signal Processing **29**(3), 463–470 (1981).

[133] S. J. Norton and I. J. Won, "Time exposure acoustics," IEEE Transactions on Geoscience and Remote Sensing **38**(3), 1337–1343 (2000).

[134] C. R. Jensen, R. W. Ritchie, M. Gyöngy, J. R. T. Collin, T. Leslie, and C.-C. Coussios, "Spatiotemporal Monitoring of High-Intensity Focused Ultrasound Therapy with Passive Acoustic Mapping," Radiology **262**(1), 252–261 (2012).

[135] C. R. Jensen, R. O. Cleveland, and C. C. Coussios, "Real-time temperature estimation and monitoring of HIFU ablation through a combined modeling and passive acoustic mapping approach," Physics in Medicine and Biology **58**(17), 5833–5850 (2013).

[136] J. Choi, R. C. Carlisle, C. Coviello, L. Seymour, and C. C. Coussios, "Non-invasive and real-time passive acoustic mapping of ultrasound-mediated drug delivery," Physics in Medicine and Biology **59**(17), 4861–4877 (2014).

[137] J. J. Kwan, R. Myers, C. M. Coviello, S. M. Graham, A. R. Shah, E. Stride, R. C. Carlisle, and C. C. Coussios, "Ultrasound-Propelled Nanocups for Drug Delivery," Small **11**(39), 5305–5314 (2015).

[138] M. Gyöngy and C.-C. Coussios, "Passive cavitation mapping for localization and tracking of bubble dynamics," The Journal of the Acoustical Society of America **128**(4), EL175–EL180 (2010).

[139] B. D. Van Veen and K. M. Buckley, "Beamforming: A Versatile Approach to Spatial Filtering," IEEE ASSP Magazine **5**(2), 4–24 (1988).

[140] J. Lighthill, *Waves in fluids* (Cambridge university press, 2001).

[141] C. Coviello, R. Kozick, J. Choi, M. Gyöngy, C. Jensen, P. P. Smith, and C.-C. Coussios, "Passive acoustic mapping utilizing optimal beamforming in ultrasound therapy monitoring.," The Journal of the Acoustical Society of America **137**(5), 2573 (2015).

[142] J. Capon, "High-resolution frequency-wavenumber spectrum analysis," Proceedings of the IEEE **57**(8), 1408–1418 (1969).

[143] P. Stoica, Z. Wang, and J. Li, "Robust Capon beamforming," IEEE Signal Processing Letters **10**(6), 172–175 (2003).

[144] J. Li, P. Stoica, and Z. Wang, "On robust Capon beamforming and diagonal loading," IEEE Transactions on Signal Processing **51**(7), 1702–1715 (2003).

[145] D. T. Blackstock, *Fundamentals of physical acoustics* (John Wiley \& Sons, New York City, NY, 2000).

[146] A. G. Brisson, C. Nowacki, W. R. Shene, T. H. Burdick, and E. Dela-Cruz, "Aiming system for kidney stone disintegrator," (1988).

[147] M. Kuwahara, N. Ioritani, K. Kambe, S. Orikasa, and K. Takayama, "Anti-miss-shot control device for selective stone disintegration in extracorporeal shock wave lithotripsy," Shock Waves **1**(2), 145–148 (1991).

[148] C. Devevey, F. Denis, and G. Gimenez, "Real time tracking of gallstones on ultrasonic images for extracorporeal lithotripsy," in *Proc of IEEE Ultrasonics Symposium*, Tucson, AZ (1992), pp. 1073–1076.

[149] M. Orkisz, T. Farchtchian, D. Saighi, M. Bourlion, N. Thiounn, G. Gimenez, B. Debre, and T. A. Flam, "Image based renal stone tracking to improve efficacy in extracorporeal lithotripsy," The Journal of Urology **160**(4), 1237–1240 (1998).

[150] M. Orkisz, M. Bourlion, G. Gimenez, and T. A. Flam, "Real-time target tracking applied to improve fragmentation of renal stones in extra-corporeal lithotripsy," Machine Vision and Applications **11**(3), 138–144 (1999).

[151] C. C. Chang, S. M. Liang, Y. R. Pu, C. H. Chen, I. Chen, T. S. Chen, C.-L. Kuo, F. M. Yu, and Z. F. Chu, "In vitro study of ultrasound based real-time tracking of renal stones for shock wave lithotripsy: part 1," The Journal of Urology **166**(1), 28–32 (2001).

[152] C. C. Chang, I. Manousakas, Y. R. Pu, S. M. Liang, C. H. Chen, T. S. Chen, F. M. Yu, W.-H. Yang, Y.-C. Tong, and C.-L. Kuo, "In vitro study of ultrasound based real-time tracking for renal stones in shock wave lithotripsy: part II—a simulated animal experiment," The Journal of Urology **167**(6), 2594–2597 (2002).

[153] C. Bohris, T. Bayer, and C. Lechner, "Hit/miss monitoring of ESWL by spectral Doppler ultrasound," Ultrasound in Medicine & Biology **29**(5), 705–712 (2003).

[154] I. Manousakas, Y.-R. Pu, C. C. Chang, and S. M. Liang, "Ultrasound image analysis for renal stone tracking during extracorporeal shock wave lithotripsy," in *Proc of IEEE Engineering in Medicine and Biology Society Ann Int Conf*, New York City, NY (2006), pp. 2746–2749.

[155] N. R. Owen, M. R. Bailey, L. A. Crum, O. A. Sapozhnikov, and L. A. Trusov, "The use of resonant scattering to identify stone fracture in shock wave lithotripsy," The Journal of the Acoustical Society of America **121**(1), EL41–EL47 (2007).

[156] C. Chaussy, E. Schmiedt, D. Jocham, J. Schüller, H. Brandl, and B. Liedl, "Extracorporeal shock-wave lithotripsy (ESWL) for treatment of urolithiasis," Urology **23**(5), 59–66 (1984).

[157] A. Rahmouni, R. Bargoin, A. Herment, N. Bargoin, and N. Vasile, "Color Doppler twinkling artifact in hyperechoic regions," Radiology **199**(1), 269–271 (1996).

[158] W. Lu, O. A. Sapozhnikov, M. R. Bailey, P. J. Kaczkowski, and L. A. Crum, "Evidence for Trapped Surface Bubbles as the Cause for the Twinkling Artifact in Ultrasound Imaging," Ultrasound in Medicine and Biology **39**(6), 1026–1038 (2013).

[159] J. C. Simon, O. A. Sapozhnikov, W. Kreider, M. Breshock, J. C. Williams Jr, and M. R. Bailey, "The role of trapped bubbles in kidney stone detection with the color Doppler ultrasound twinkling artifact," Physics in Medicine & Biology **63**(2), 25011 (2018).

[160] C. Prada, F. Wu, and M. Fink, "The iterative time reversal mirror: A solution to self-focusing in the pulse echo mode," The Journal of the Acoustical Society of America **90**(2), 1119–1129 (1991).

[161] C. Prada, J. Thomas, and M. Fink, "The iterative time reversal process: Analysis of the convergence," The Journal of the Acoustical Society of America **97**(1), 62–71 (1995).

[162] F. Wu, J.-L. Thomas, and M. Fink, "Time reversal of ultrasonic fields. Il. Experimental results," IEEE Transactions on Ultrasonics, Ferroelectrics, and Frequency Control **39**(5), 567–578 (1992).

[163] J.-L. Thomas, F. Wu, and M. Fink, "Time reversal focusing applied to lithotripsy," Ultrasonic Imaging **18**(2), 106–121 (1996).

[164] C. Prada, S. Manneville, D. Spoliansky, and M. Fink, "Decomposition of the time reversal operator: Detection and selective focusing on two scatterers," The Journal of the Acoustical Society of America **99**(4), 2067–2076 (1996).

[165] K. Shoar, B. W. Turney, and R. O. Cleveland, "Tracking kidney stones in a homogeneous medium using a trilateration approach," The Journal of the Acoustical Society of America **142**(6), 3715–3721 (2017).

[166] M. A. Averkiou and R. O. Cleveland, "Modeling of an electrohydraulic lithotripter with the KZK equation," The Journal of the Acoustical Society of America **106**(1) (1999).

[167] J. A. McAteer, J. C. Williams Jr, R. O. Cleveland, J. Van Cauwelaert, M. R. Bailey, D. A. Lifshitz, and A. P. Evan, "Ultracal-30 gypsum artificial stones for research on the mechanisms of stone breakage in shock wave lithotripsy," Urological Research **33**(6), 429–434 (2005).

[168] J. C. Lagarias, J. A. Reeds, M. H. Wright, and P. E. Wright, "Convergence Properties of the Nelder–Mead Simplex Method in Low Dimensions," SIAM Journal on Optimization **9**(1), 112–147 (1998).

[169] P. V. Chitnis and R. O. Cleveland, "Acoustic and cavitation fields of shock wave therapy devices," AIP Conference Proceedings **829**, 440–444 (2006).

[170] F. Ueberle and A. J. Rad, "Ballistic Pain Therapy Devices: Measurement of Pressure Pulse Parameters," Biomedical Engineering / Biomedizinische Technik **57**(SI-1 Track-H), 700–703 (2012).

[171] Y. Liu, X. Chen, A. Guo, S. Liu, and G. Hu, "Quantitative Assessments of Mechanical Responses upon Radial Extracorporeal Shock Wave Therapy," Advanced Science 1700797 (2017).

[172] C. H. Farny, R. G. Holt, and R. A. Roy, "Temporal and Spatial Detection of HIFU-Induced Inertial and Hot-Vapor Cavitation with a Diagnostic Ultrasound System," Ultrasound in Medicine and Biology **35**(4), 603–615 (2009).

[173] E. Neppiras, "Acoustic cavitation," Physics Reports **61**(3), 159–251 (1980).

[174] P. Zhong, I. Cioanta, F. H. Cocks, and G. M. Preminger, "Inertial cavitation and associated acoustic emission produced during electrohydraulic shock wave lithotripsy.," The Journal of the Acoustical Society of America **101**(5), 2940–50 (1997).

[175] J. J. Kwan, S. Graham, R. Myers, R. Carlisle, E. Stride, and C. C. Coussios, "Ultrasound-induced inertial cavitation from gas-stabilizing nanoparticles," Physical Review E **92**(2) (2015).

[176] S. Bhatnagar, J. J. Kwan, A. R. Shah, C. C. Coussios, and R. C. Carlisle, "Exploitation of sub-micron cavitation nuclei to enhance ultrasound-mediated transdermal transport and penetration of vaccines," Journal of Controlled Release **238**, 22–30 (2016).

[177] R. Myers, C. Coviello, P. Erbs, J. Foloppe, C. Rowe, J. Kwan, C. Crake, S. Finn, E. Jackson, J. M. Balloul, C. Story, C. Coussios, and R. Carlisle, "Polymeric cups for cavitation-mediated delivery of oncolytic vaccinia virus," Molecular Therapy **24**(9), 1627–1633 (2016).

[178] *IEC 61846*, Ultrasonics, Pressure pulse lithotripters - Characteristics of fields (1998).

[179] J. Chandrapal, A. Tang, A. Navetta, B. Trojan, A. Haynes, W. de Riese, S. Filleur, and T. Nelius, "Single-Center Experience With the Dual-Focus Storz Modulith SLX-F2 Lithotripter: A Retrospective Study," World Journal of Nephrology and Urology **3**(1), 7–17 (2014).